OXIDE NANOWIRE ARRAYS FOR ENERGY SCIENCES

A Dissertation
Presented to
The Academic Faculty

by

Sheng Xu

In Partial Fulfillment
of the Requirements for the Degree
Doctor of Philosophy in the
School of Materials Science and Engineering

Georgia Institute of Technology
December, 2010

OXIDE NANOWIRE ARRAYS FOR ENERGY SCIENCES

Approved by:

Dr. Zhong Lin Wang, Advisor
School of Materials Science and Engineering
Georgia Institute of Technology

Dr. Russell Dupuis
School of Electrical and Computer Engineering
Georgia Institute of Technology

Dr. Robert L. Snyder
School of Materials Science and Engineering
Georgia Institute of Technology

Dr. C. F. Jeff Wu
School of Industrial and Systems Engineering
Georgia Institute of Technology

Dr. Christopher Summers
School of Materials Science and Engineering
Georgia Institute of Technology

Dr. Mostafa El-Sayed
School of Chemistry and Biochemistry
Georgia Institute of Technology

Date Approved: October 29, 2010

As an infinitesimal step in the scientific advancement of the entire world

ACKNOWLEDGEMENTS

First I would like to thank my advisor, Dr. Zhong Lin Wang, for his scientific vision in pioneer nanoscience research, his encouragement and guidance during my PhD study, and his constant support for my personal life. Professionally, Dr. Wang launches my scientific career, to which I am determined to dedicate the rest of my life. And personally, he has always been a strong supporter when I need help in my personal life. I would also like to give thanks to members of my dissertation committee, Dr. Snyder, Dr. Summers, Dr. Dupuis, Dr. Wu, and Dr. El-Sayed for the time, patience and valuable advice that they generously offer. Also thank the professors who have instructed the courses I took, and have tirelessly answered my numerous questions.

I would like to say thank you to my friends, who helped me to settle down when I first came to this country. I would also like to thank my colleagues and friends, who trained me on the equipments and taught me a great deal, and who collaborated with me and provided insightful discussions. The work presented in this thesis would not have been achieved without their help and inspiration.

Special thanks to my family, who made what I am experiencing possible in the first place. Also I have to say sorry to my family, to whom I am really indebted. Thanks to my grandmother, who raised me up, for the constant love and care she gave me. Being away from my home country for almost five years, I always feel guilty that I have been unable to take care of her, who is now in her eighties and living on her own. I also feel the pain when my only uncle went through surgery and passed away, and I did not find a chance to attend his funeral. Words cannot express my regret that I could not be with him

during his last days. Finally, I would like to say thank you to my deceased father, for motivating me to work hard since I was a child. Though my family members have never left my hometown and have never had a chance to see the world outside, nor have them had littlest clue of what I have been working on in the US, their love and expectation is my constant source of inspiration.

TABLE OF CONTENTS

LIST OF FIGURES

LIST OF SYMBOLS AND ABBREVIATIONS

Symbol-1	Symbol-1 Means
LED	Light emitting diode
LD	Laser diode
PZT	$PbZr_{0.52}Ti_{0.48}O_3$
MOCVD	Metal organic chemical vapor deposition
MBE	Molecular beam epitaxy
IPA	Isopropyl alcohol
HMTA	Hexamethylenetetramine
pH	Potential of hydrogen
SEM	Scanning electron microscopy
PVD	Physical vapor deposition
EBL	Electron beam lithography
PMMA	Polymethyl methacrylate
XRD	X-ray diffraction
TEM	Transmission electron microscopy
HRTEM	High resolution transmission electron microscopy
RIE	Reactive ion etching
FWHM	Full width at half maximum
NBE	Near band edge
UV	Ultraviolet
STO	$SrTiO_3$

SUMMARY

Oxide nanowire arrays are playing an important role in energy sciences nowadays, including energy harvesting, energy storage, and power management. By utilizing a wet chemical growth method, we demonstrated the capabilities of synthesizing density controlled vertical ZnO nanowire arrays on a general substrate, optimizing the aspect ratio of the vertical ZnO nanowire arrays guided by a statistical method, epitaxially growing patterned vertical ZnO nanowire arrays on inorganic substrates, epitaxially growing patterned horizontal ZnO nanowire arrays on non-polar ZnO substrates, and the lift-off of the horizontal ZnO nanowire arrays onto general flexible substrates. In addition, single crystalline $PbZr_xTi_{1-x}O_3$ (PZT) nanowire arrays were epitaxially grown on conductive and nonconductive substrates by hydrothermal decomposition. Beyond that, based on the as-synthesized ZnO nanowire arrays, we demonstrated multilayered three dimensionally integrated direct current and alternating current nanogenerators. By integrating a ZnO nanowire based nanogenerator with a ZnO nanowire based nanosensor, we demonstrated solely ZnO nanowire based self-powered nanosystems. Also, utilizing a commercial full-wave bridge rectifier, we rectified the alternating output charges of the nanogenerator based on PZT nanowire arrays, and the rectified charges were stored into capacitors, which were later discharged to light up a laser diode (LD). In addition, blue/near-ultraviolet (UV) light emitting diodes (LED) composed of ordered ZnO nanowire arrays on p-GaN wafers were presented.

CHAPTER 1

INTRODUCTION

There are three most important and popular one-dimensional nanostructures that are being actively studied nowadays in nanoscience and nanotechnology: carbon nanotubes,(*1-2*) silicon nanowires,(*3*) and ZnO nanowire/nanobelts.(*4-5*) ZnO nanowires stand out from the family of one-dimensional nanomaterials, because of its superior performance and far reaching applications in biomedical science, energy science, electronics and optoelectronics.(*6-8*) ZnO is a piezoelectric material. It has a direct wide band gap of 3.37 eV, and a large exciton binding energy of 60 meV. It has many applications in electronic, optoelectronic, and electromechanical devices.

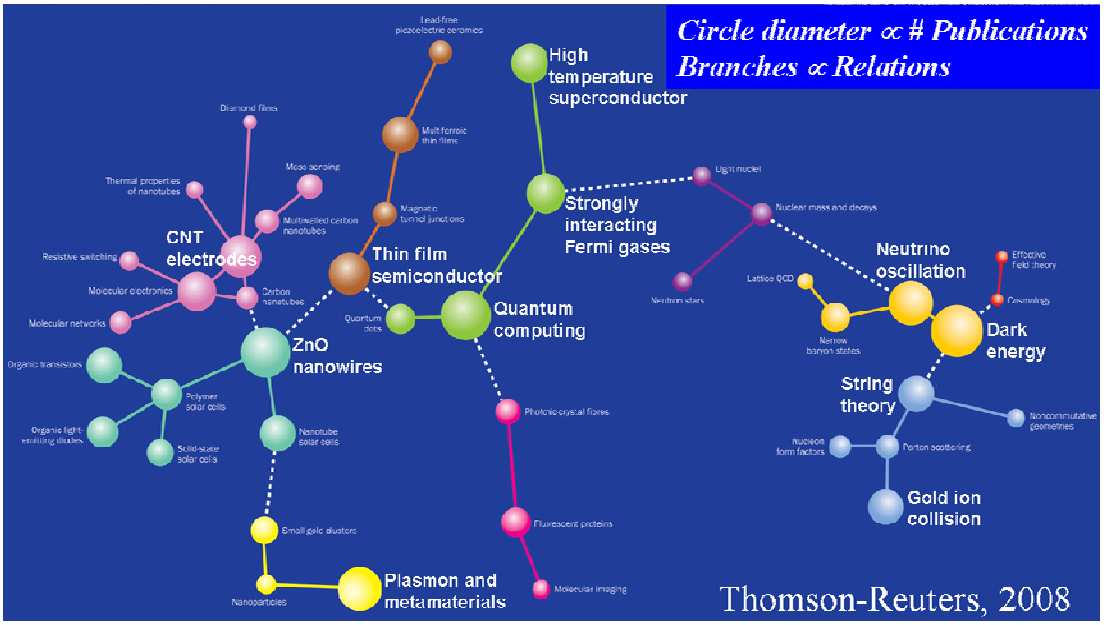

Figure 1. Map of physics.(*10*)

In reality, over the last decade, there has been an exponential increase in the number of publications on ZnO nanowires according to an editorial themed issue published in the Journal of Materials Chemistry (*J. Mater. Chem.,* 2009, 19, 826-827.).(*9*) In addition, as illustrated in the "Map of Physics" (Figure 1) by *Physics World*, each

circle represents a sub-discipline of physics, and the size of the circle is proportional to the number of publications in that area, and the branches represent its popularity. On this map, we can find quantum computing, dark energy, string theory, high temperature superconductor, carbon nanotube electrodes, and ZnO nanowires, etc. A clear message is that ZnO nanowire research is currently one of the most important and popular research subjects in the entire field of physics (*Physics World,* 2008, October, 21, 36-37.).(*10*)

CHAPTER 2

RATIONAL GROWTH OF OXIDE NANOWIRE ARRAYS BY WET CHEMICAL METHODS

ZnO is a semiconductive and piezoelectric material with a direct wide bandgap of 3.37 eV and a large exciton binding energy of 60 meV at room temperature.(*11-12*) It has been demonstrated to have enormous applications in building up electronic, optoelectronic, electrochemical, and electromechanical nanodevices,(*6-7, 13-16*) such as ultraviolet (UV) lasers,(*17-18*) light-emitting diodes,(*19-21*) field emission devices,(*22-24*) high performance nanosensors,(*25-27*) solar cells,(*28-31*) piezoelectric nanogenerators,(*32-36*) and nano-piezotronics.(*8, 37-38*)

One dimensional ZnO nanostructures have been synthesized by a wide range of approaches, such as wet chemical methods,(*39-41*) PVD,(*4-5, 42*) metal-organic chemical vapor deposition (MOCVD),(*43-45*) molecular beam epitaxy (MBE),(*46*) pulsed laser deposition,(*47*) sputtering,(*48*) flux,(*49*) eletrospinning,(*50-51*) and even top down approaches.(*52*) Among those techniques, PVD and flux usually require high temperature, and easily incorporate catalysts or impurities into the ZnO nanostructures, and therefore are less likely to be able to integrate with flexible organic substrate for future foldable and portable electronic applications. MOCVD and MBE can give high quality ZnO nanowire arrays, but are usually limited by the sample uniformity, low product yield, and choices of substrate. Also, the experimental cost is usually very high, and they are thus less widely adopted. Pulsed laser deposition, sputtering and top down approaches have less controllability and repeatability compared with other techniques.

Comparatively speaking, the wet chemical methods are attractive, having several advantages, such as low cost, less hazardous, and thus capable of easy scaling up;(*53-54*)

the possibility of achieving satisfying crystallinity at a relatively low temperature (<100 ℃) without further calcination, and thus compatible with flexible organic substrates; no need for the use of metal catalysts, and thus can be integrated with the present silicon technologies;(*55*) besides, there are a variety of parameters that we can play with to fully control the morphologies and properties of the products.(*56-57*) The wet chemical methods have been demonstrated as a very powerful technique for growing one dimensional ZnO nanostructures.

2.1 Density controlled growth of vertical ZnO nanowire arrays on a general substrate

The seeded grown ZnO nanowires were usually very dense and its density could not be easily controlled.(*41, 59*) Using a novel chemical approach, density-controlled, vertically aligned ZnO nanowire arrays were synthesized on both rigid and flexible substrates.(*58*) We have chosen Si (100) and flexible Kapton polymer as the substrates. For simplicity of description, we use Si substrate to describe the experimental procedure and to illustrate the effects of various experimental parameters on the growth.

A piece of Si (100) wafer substrate was cleaned by a standard cleaning progress. First, the wafer was ultrasonicated consecutively in acetone, ethanol, isopropyl alcohol (IPA) and de-ionized water each for 10 minutes, then blew dry by dry nitrogen gas and then baked on hotplate at 200 °C for 5 minutes to get rid of any adsorbed moisture. Then, a 50 nm thick layer of Au was deposited on top of the Si wafer by magnetron plasma sputtering, which is expected to act as an “intermediate-layer” to assist the growth. Between the Si wafer and Au layer, 20 nm of Ti was deposited as an adhesion layer to buffer the large lattice mismatch between Si(100) surface with native oxide on and Au(111) surface and to improve the interface bonding. Then the substrate was annealed at 300 °C for 1 hour.

The next step is to prepare the nutrient solution. The nutrient solution was composed of a 1 to 1 ratio of zinc nitrate and hexamethylenetetramine (HMTA) (Figure 2). Both of the chemicals were reagent grade from Fluka.

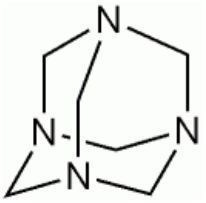

Figure 2. Molecular structure of HMTA.

$$(CH_2)_6N_4 + 6\ H_2O \leftrightarrow 4\ NH_3 + 6\ HCHO \quad (1)$$

$$NH_3 + H_2O \leftrightarrow NH_3 \cdot H_2O \quad (2)$$

$$NH_3 \cdot H_2O \leftrightarrow NH_4^+ + OH^- \quad (3)$$

$$Zn^{2+} + 2\ OH^- \leftrightarrow Zn(OH)_2 \quad (4)$$

$$Zn(OH)_2 \xrightarrow{\Delta} ZnO + H_2O \quad (5)$$

The reactions taking place in aqueous systems are usually considered to be in a reversible equilibrium, and the driving force is to minimize the free energy of the entire reaction system, which is the nature of wet chemical method. The chemistry of the growth is well documented.(*60-61*) Zinc nitrate salt provides Zn^{2+} ions required for building up ZnO nanowires. Water molecules in the solution provide O^{2-} ions. Even though the exact function of HMTA during the ZnO nanowire growth is still unclear, it is believed to act as a weak base. Shown in Figure 2 is the molecular structure of HMTA. It gradually decomposes in water into small molecules, ammonia and formaldehyde, to release the strain energy that was built in the structure, as shown in reaction equation (1). The ammonia creates a basic environment, which helps to form zinc hydroxide, reaction equations (2-4). Then at an elevated temperature, Zinc hydroxide undergoes dehydration and produce ZnO. We can play with the various reaction parameters to control the morphology, dimensionality, and crystallinity of the nanowires.

The slow decomposition of HMTA in the water solution gradually producing OH^- is critical in the synthesis process because, if the HMTA hydrolyzes very fast and produces a lot of OH^- in a short period of time, the Zn^{2+} ions in solution would precipitate out very quickly due to the high potential of hydrogen (pH) environment, which would have little contribution to the ZnO nanowire oriented growth, and eventually results in fast consumption of the nutrient and prohibits further growth of ZnO nanowires.

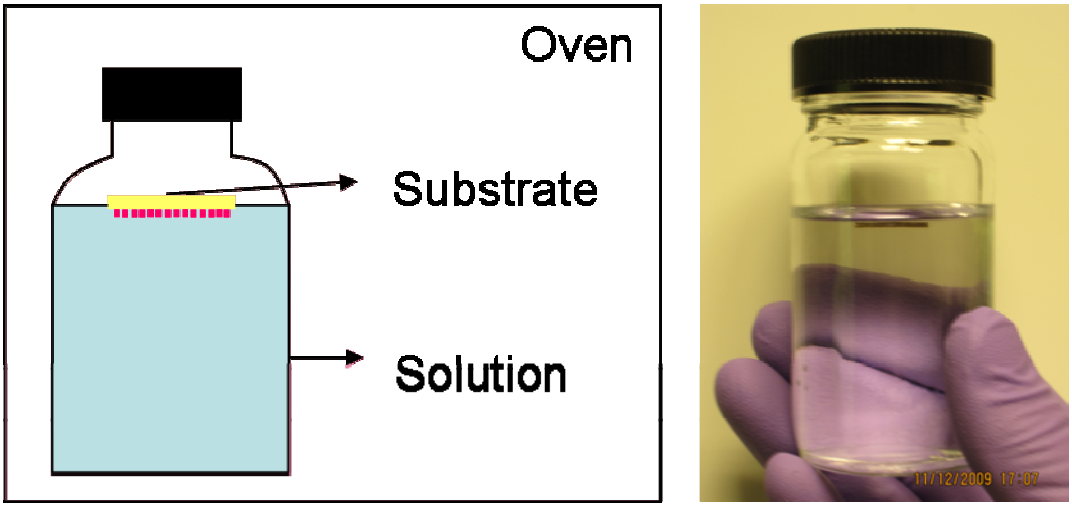

Figure 3. The graph on the left is the schematic experimental setup; the camera image on the right is the actual reaction container, where we can clearly see a substrate floating on the surface of the growth solution.

Growth of ZnO nanowires was conducted in mechanical convection oven (Yamato DKN400). Shown on the left in Figure 3 is the schematic experimental setup. One thing worth noting is that we float the substrate facing down on the surface of the reaction solution by virtue of surface tension, which prevents the homogeneously formed ZnO nanostructures inside the solution body falling onto the substrate and inhibiting the regular growth of ZnO nanowires. When heated in an oven, ZnO nanowires heterogeneously nucleate and grow on the substrate. Shown on the right in Figure 3 is a real camera image of it. It is apparent that a substrate floating on the solution surface. The annealing process helps the as-deposited Au layer to form a uniform crystalline thin layer

on the surface of Si substrate, which is critical in the oriented growth of aligned ZnO nanowires.

The growth process of ZnO nanowires can be controlled through the five chemical reactions listed above. All of the five reactions are actually in equilibrium and can be controlled by adjusting the reaction parameters, such as precursor concentration, growth temperature and growth time, in order to push the reaction equilibrium forward or backward. In general, precursor concentration determines the nanowire density. Growth time and temperature control the ZnO nanowire morphology and aspect ratio. In the following parts, the growth mechanism of ZnO nanowire arrays is elucidated with detailed analysis.

2.1.1 Concentration

The density of ZnO nanowires on the substrate could be controlled by the initial concentration of the zinc salt and HMTA. To explore the relationship between the precursor concentration and the density of the ZnO nanowire arrays, a series of experiments were performed by varying the precursor concentration but keep the ratio constant between the zinc salt and HMTA. Experimental results show that the density of the nanowire arrays is closely related to the precursor concentration. Detailed analysis of the measured data is shown in Figure 4 (red line). From 0.1 mM to 5 mM, the ZnO nanowires density, defined as number of nanowires per 100 μm^2, increases dramatically, possibly for the following reasons. Zinc chemical potential inside the solution body increases with zinc concentration. To balance the increased zinc chemical potential in solution, more nucleation sites on the substrate surface will be generated. So, the density of ZnO nanowires increases.

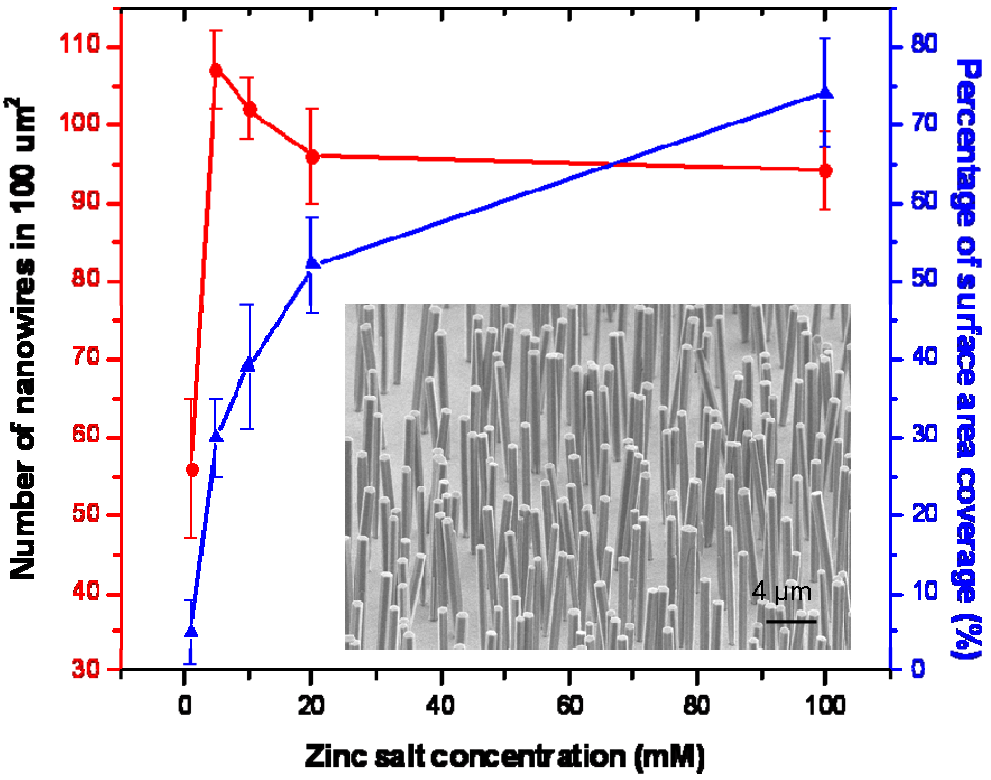

Figure 4. Density varied with concentration: Plot of ZnO nanowire density in a 100 μm^2 area (red line) and plot of area percentage covered by ZnO nanowires (blue line). Each data point was obtained from 4 different areas. Inset is a typical scanning electron microscopy (SEM) image of ZnO nanowires grown at 5 mM.

When further increasing the zinc concentration, the density of ZnO nanowires remains approximately steady with a little tendency of decrease. The steady/saturated density may be understood from the nucleation and growth process. The nanowire density is decided by the number of nuclei formed at the very beginning of the growth, which continued to grow and form nanorods (shorter nanowires). The arrival of more ions on the substrate may not initiate new nuclei at a later stage because of two possible reasons. One, with consideration the critical size required for a nucleus to grow into a crystal, no new nanorods would form if the sizes of the nuclei are smaller than the critical size. Second, due to the existence of the first group of nanorods, the newly arrived ions on the substrate have higher probability to reach the existing nanowires rather than to the newly formed nuclei, thus, the size of the nuclei may not exceeds the critical size and

they will eventually dissolve into the solution body. In such cases, a continuous increase in solution concentration may not increase the density of the nanowires when its density is larger than the saturation density. This also explains why the grown nanowires in our experiments have fairly uniform height. Even though the density of the ZnO nanowire remains steady at high precursor concentration level, the surface coverage percentage increases slightly due to the lateral growth of the nanowires (Figure 4, blue line).

2.1.2 Growth time

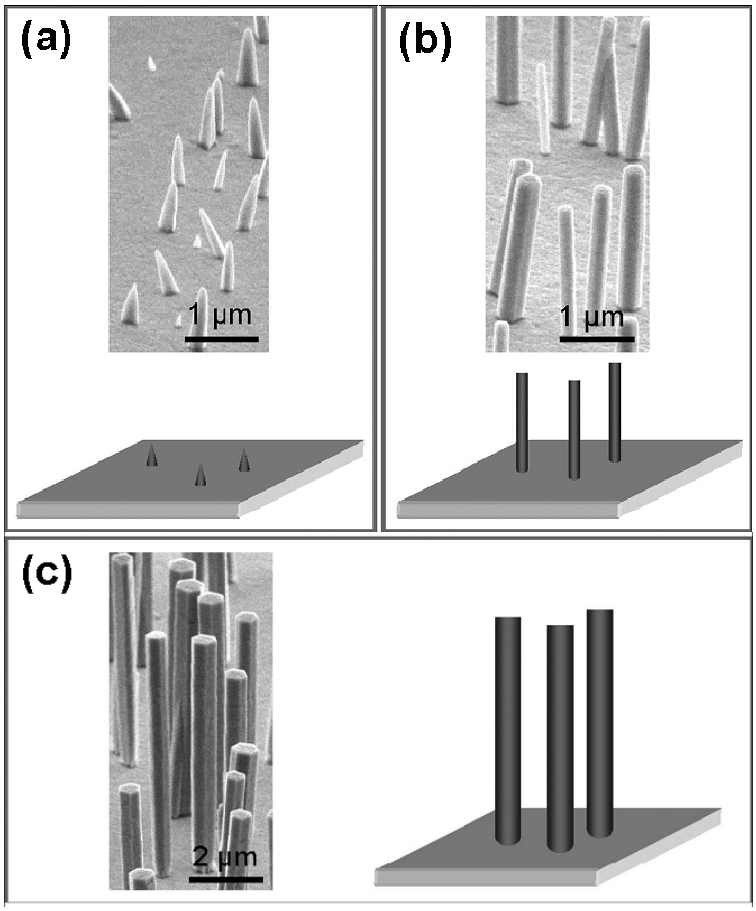

Figure 5. Time dependent of ZnO nanowire morphology evolution: (a) 0.5 hour; (b) 6 hours; (c) 48 hours.

Wurtzite ZnO has polar surfaces, such as (0001) and $(000\bar{1})$, and non-polar surfaces such as $\{01\bar{1}0\}$ and $\{2\bar{1}\bar{1}0\}$. At different growth stages, including at the beginning, in the middle and at the end, the polar surfaces axial growth is found to have a

different relative growth rate to non-polar surfaces' lateral growth. At the beginning growth period (from the very start to around half an hour), lateral growth seems to be more significant than axial growth (Figure 5(a)). When the growth time exceeds half of an hour, the width of ZnO nanowires is almost independent of time, indicating little lateral growth [Figure 5(b)]. This indicates that, at the beginning growth stage, lateral growth is more significant than axial growth. In the middle growth stage, which means to grow from half an hour to around 6 hours, axial growth is dominant. At the final growth stage, which means to grow from 6 hours to 48 hours in our experiments, lateral growth and axial growth seem to be equally significant, as can be seen from Figure 5(b) and 5(c). In this period, ZnO nanowires length is almost doubled. At the same time, ZnO nanowires width is also doubled. The aspect ratio remains nearly constant.

Our previous study indicates that the Zn-terminated (0001) surface is much more catalytically active than the O-terminated ($000\bar{1}$) surface for the growth of nanowires. For the aligned array, we believe that all of the nanowires have their positive c-axis pointing upwards, which means that the (0001) surface is at the growth front. This characteristic results in the alignment of polarity and piezoelectric effect of all the nanowires.

2.1.3 Temperature

Temperature is an important factor in keeping high aspect ratio of the hexagonal prism shape of ZnO nanowires. In our experiments, 70 ℃ is found to be the optimum temperature to get high aspect ratio and well defined hexagonal prism shape of the ZnO nanowires [Figure 6(b)]. If going to a lower temperature, for example 60 ℃ [Figure 6(c)], the aspect ratio becomes smaller compared to that at 70 ℃. Aspect ratio of the ZnO nanowires is determined by the relative growth rate of the polar surfaces and non-polar surfaces. Therefore, it means that the relative growth rate of polar surface to non-polar surface at low temperatures is smaller than that at high temperatures. By increasing the

temperature for example to 95 °C, pyramid shaped ZnO nanorods were grown [Figure 6(a)]. The temperature dependent growth behavior may also be understood from the basic theory of crystal nucleation and growth. When the temperature is low, the mobility and the diffusion length of the ions on the substrate are rather limited, which prohibit the ions to diffuse around, and therefore large size nuclei were formed. Thus, the nanowire density is low. At high temperature, the mobility and diffusion length of the ions are large enough to reach the sites of the firstly grown nanowires, thus, no new nuclei would be formed because the precursor ions have higher affinity to the already formed seeds than bare substrate, resulting in a lower density of nanowires on the substrate. At an optimum temperature, such as 70 ℃, the mobility of the ions is moderate and their diffusion length is within a small range in the vicinity of the substrate, thus the accumulation of ions at local regions results in high density of nanowires. But their size is small because of the conservation of total ions that are able to migrate to near the substrate.

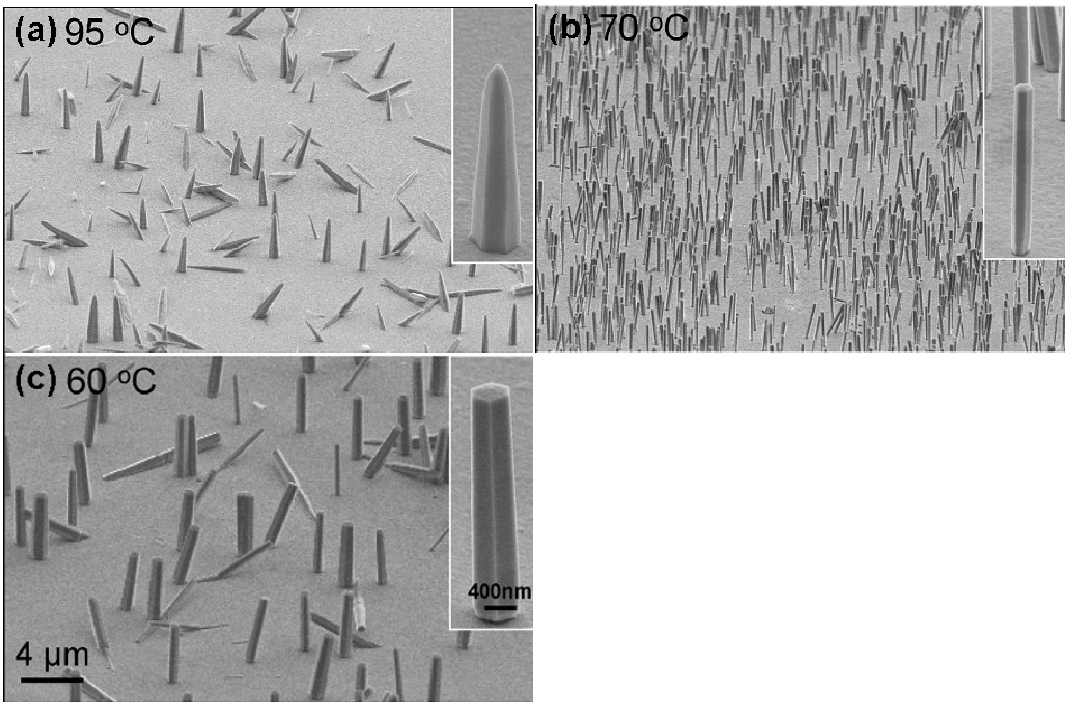

Figure 6. ZnO nanowires grown at different temperatures: 60° tilt degree view of ZnO nanowires synthesized at (a) 95 ℃, (b) 70 ℃, and (c) 60 ℃. The three images are recorded at the same magnification and the three inset images are at the same magnification as well.

As discussed previously, HMTA functions as a slowly decomposing weak base, which maintains the weak basic environment in the solution and successively provides Zn^{2+} ions with OH^- ions. From reaction (1), we find that 7 moles of reactant produce 10 moles of product. So, if increasing the reaction temperature, reaction (1) would move forward by virtue of entropy increase, which means that HMTA decomposes more quickly at high temperature than at low temperature. That is to say, at the very beginning, HMTA has already decomposed to a relatively large degree and has produced enough OH^-, resulting in a sufficient and thorough growth of ZnO at the beginning. Therefore, the base of our ZnO nanorods is thicker than at lower temperature. Furthermore, both the axial and lateral growth rates are much increased at higher temperature. As time goes by, the supply of Zn^{2+} is limited in the reaction container and gradually becomes exhausted, which leads to the formation of incomplete shape of the nanowires (pyramids or tapped nanorods).

As discussed above, the concentration controls the nucleation density, growth time controls the aspect ratio, and temperature controls the morphology as well as aspect ratio. By adjusting those three parameters, we can optimize the aspect ratio ZnO nanowires, to be discussed in section 2.2.

2.1.4 Substrate

In the experiments, effect of different substrates on the controlled growth of aligned ZnO nanowire arrays was investigated. The results show that the substrate substances have little influence on the growth of ZnO nanowire arrays as long as the substrates were treated with a standard fabricating procedure as described previously. Growth results on different substrates are shown in Figure 7. ZnO nanowire arrays could grow not only on single crystal Si wafers (Figure 7(a)), but also on amorphous flexible polymer substrates [Figure 7(b)]. The basic requirement for the aligned growth is that the substrate is locally smooth. This technique was a low-cost, time-efficient, and scalable

method for fabricating ZnO nanowire arrays on a general substrate for various applications.

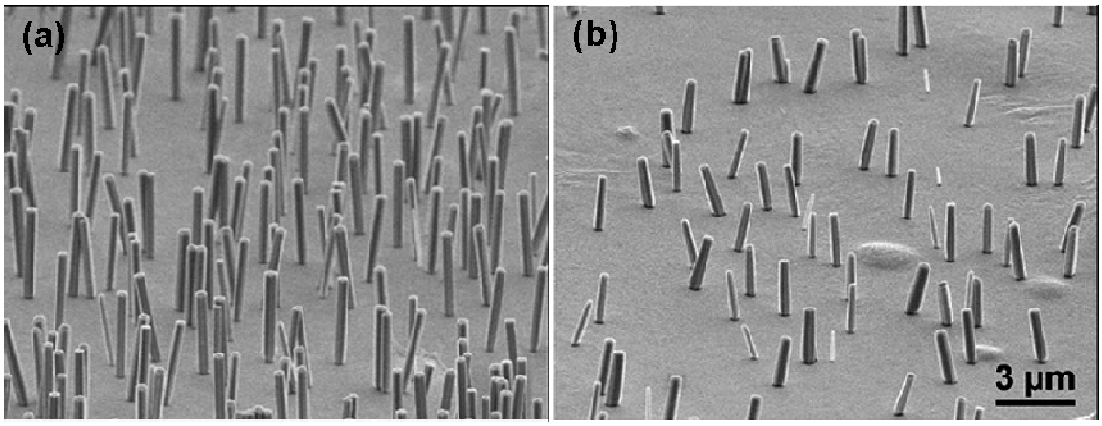

Figure 7. ZnO nanowires grown on (a) stiff Si wafer and (b) flexible Kapton polymer substrate, which are at the same magnification.

2.2 Optimizing the growth quality of ZnO nanowire arrays using a statistical design of experiments

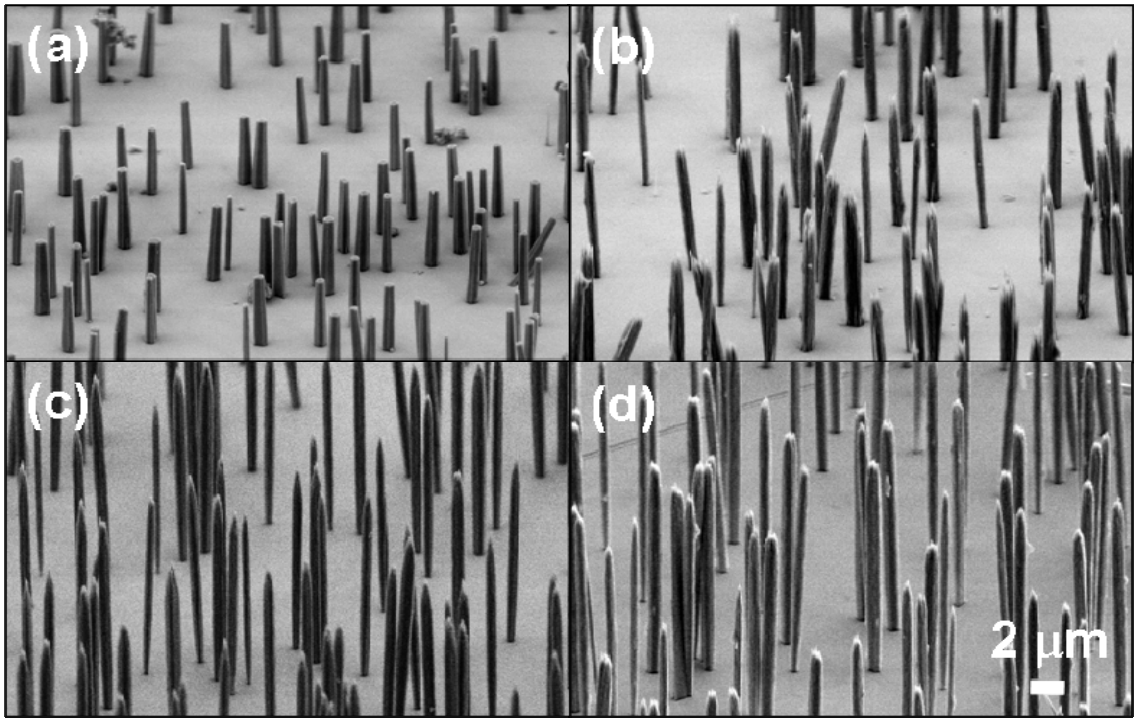

Figure 8. SEM images of ZnO nanowires of aspect ratio of (a) 7.7, (b) 12.4, (c) 14.5 and (d) 22.3, respectively.

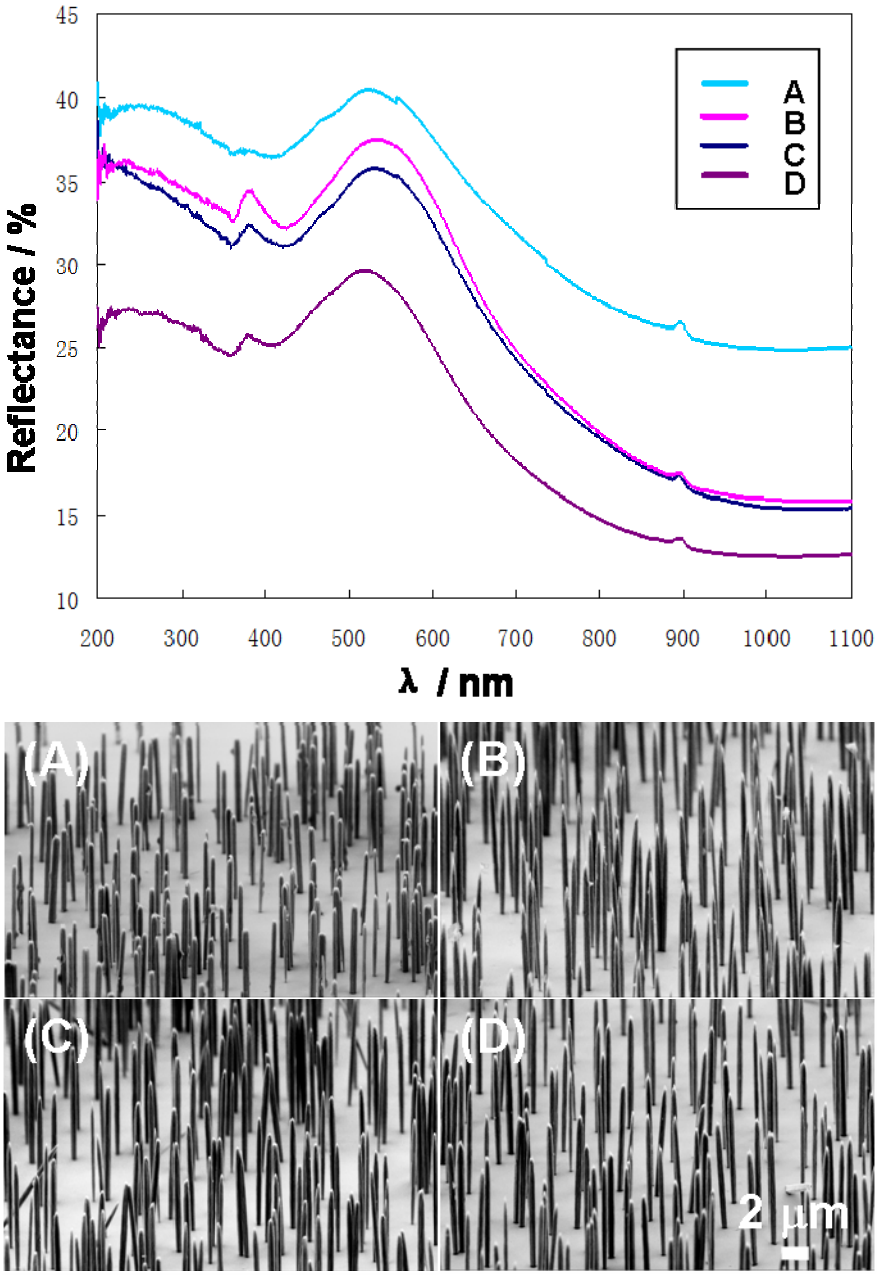

Figure 9. Reflectance spectra of the ZnO nanowire arrays of different aspect ratio. Curve A, B, C and D correspond to aspect ratio of 15.1, 20.1, 20.9 and 22.3, respectively and their representative SEM images.

In general, ZnO nanowires are typically manufactured by two methods, namely, PVD and hydrothermal decomposition. In contrast to the PVD, synthesized *via* the wet chemical method, the ZnO nanowires are of low aspect ratio typically of 10 to 15,(*59, 62*) which greatly limits their applications in which flexible and high surface to volume ratio

ZnO nanowires are needed. There has been a few reports that the aspect ratio of the ZnO nanowires could be increased by adding some external capping agents, such as ethylenediamine(*63*) and polyethylenimine;(*64*) however, at the same time, these capping agents might also introduce some undesirable impurities into the ZnO nanowires, which would greatly undermine their applications for which untainted ZnO nanowires are required. In most existing literature, there is a lack of a general theoretical guidance in experimental approach. The usual cook and look methods are time consuming and often time ineffective. We developed a novel way of optimizing the aspect ratio of hydrothermally grown ZnO nanowire arrays by utilizing a systematic statistical design and analysis method.(*57*) As guided by statistical methods, we performed a sequence of experiments toward growing aspect ratio enhanced ZnO nanowire arrays.

Classic statistical analysis did not suit this application due to the uncontrollable variation in the process and complex interactions among various factors. In this work, we used pick-the-winner rule(*65*) and one-pair-at-a-time main effect analysis(*66*) to identify optimal reaction settings. By controlling the hydrothermal reaction parameters (reaction temperature, time, precursor concentration, and capping agent), we improved the aspect ratio of ZnO nanowires from around 10 to nearly 23 (Figure 8). The statistical design and analysis methods were very effective in reducing the number of experiments performed and in identifying the optimal experimental parameters, and also enabled us to change more than one parameters at a time and analyze the relationship between the different reaction parameters.

Antireflection coating layers play a significant role in enhancing the efficiency of photovoltaic devices by increasing the light coupled into the active region of the devices.(*67-70*) The intricate distribution of the ZnO nanowires and their textured surface could trap photons, leading to a broadband suppression in reflection. Lee et al. reported that highly textured ZnO nanorod arrays synthesized via low temperature solution growth played a significant role in the performance of photovoltaic devices as an antireflective

coating.(*70*) By changing the growth conditions, they modified the shape of the ZnO nanorod tips, leading to continuously varied refractive index profiles in a single layer. Accordingly we expect that, as we increase the aspect ratio of the ZnO nanowires combined with the nanoscale surface roughness of the nanowire arrays, there would be better chances for the incident photons interacting with the nanowires' surfaces and therefore the absorption cross section would be considerably larger. Thus there would be more photons coupled into the ZnO nanowire and eventually increase the efficiency of the photovoltaic devices.

We measured the anti-reflection spectrums of different aspect ratios of the ZnO nanowire arrays at an incident angle of 60°. As illustrated in Figure 9, curves A, B, C and D correspond to ZnO nanowires of aspect ratio of 15.1, 20.1, 20.9 and 22.3, respectively. These four nanowire arrays have approximately the same nanowire density, as shown in their SEM images. Obviously, we can see that the ZnO nanowire arrays with an aspect ratio of 22.3 have an almost 30% stronger capability to suppress the reflection than those with an aspect ratio of 15.1 in both the ultraviolet and visible range. That is simply because long nanowires would have much higher chance to interact and couple the light photons with the nanowires' surface than the short ones. This showed great potential applications as antireflective coating layers in photovoltaic devices. The little bumps at around 900 nm on the curve come from the detector change during the data collection of the equipment.

2.3 Patterned growth of vertically aligned ZnO nanowire arrays on inorganic substrates at low temperature without catalyst

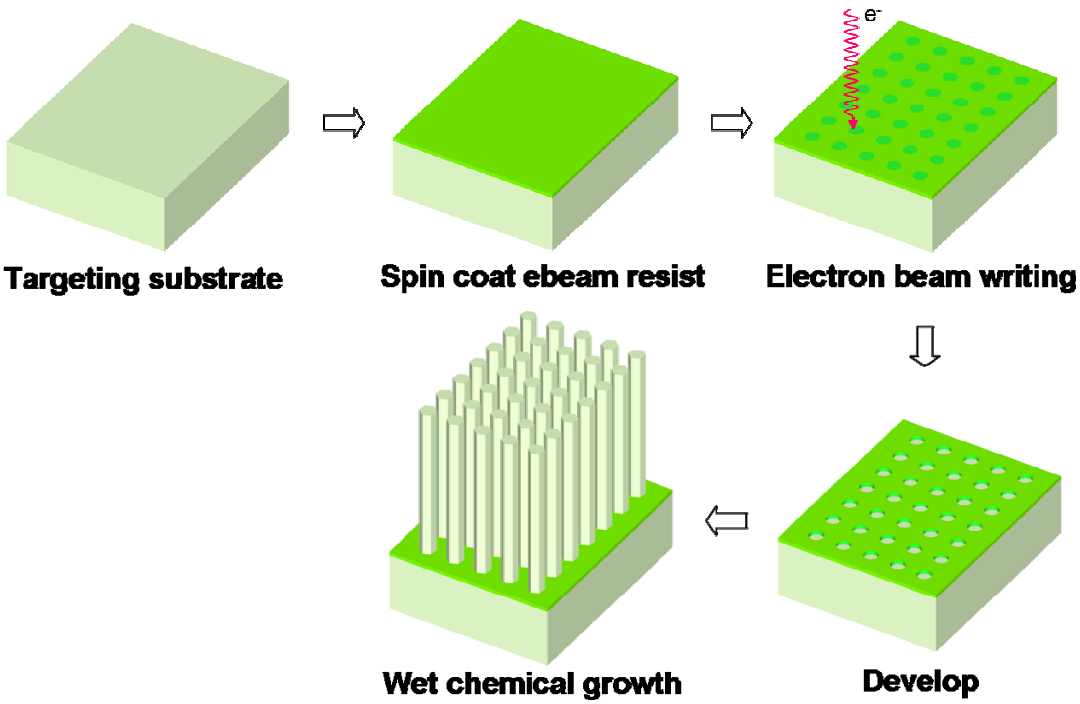

Figure 10. Flow chart growing patterned vertical ZnO nanowire arrays on inorganic substrates. The substrate could be seeded general substrates or epitaxial substrates, e.g. GaN. We spin coat a thin layer of photoresist first, then use electron beam to write patterns on the photoresist, and then put exposed photoresist into a developer. The photoresist where has been exposed by the electron beam is washed away, exposing the targeting substrate underneath in the patterned areas only. Then when we put it into the growth solution, and ZnO nanowires grow out of the photoresist openings only.

Vertically aligned ZnO nanowires have a variety of astonishing applications in electronics, optoelectronic and electromechanical nanodevices. Growth of aligned ZnO nanowires has been achieved on GaN via physical vapor deposition (PVD) at high temperature of 500-800 ℃, with the use of gold as a catalyst,(*71*) in which the catalyst initiated and guided the growth, and the epitaxial orientation relationship between the ZnO nanowires and the GaN substrate led to the aligned growth. This strategy may have the risk of introducing catalyst residual atoms into the ZnO nanowires, which is incompatible with silicon technology. Patterned growth of aligned ZnO nanowires has also been accomplished by PVD using nanosphere-masking lithography on sapphire,(*72*) which was conducted at high growth temperature, and therefore was not compatible with many other materials. MOCVD growth(*73*) and template-assisted growth(*74*) have also

been employed for the fabrication of vertically aligned ZnO nanowires. Yi et al. have demonstrated a technique of growing periodically arranged ZnO nanorod arrays on a silicon substrate coated with ZnO seeds by electron beam lithography (EBL).(*75*) But their nanorods were thick in diameter and had a rather small aspect ratio,(*76-77*) which greatly limited their applications.

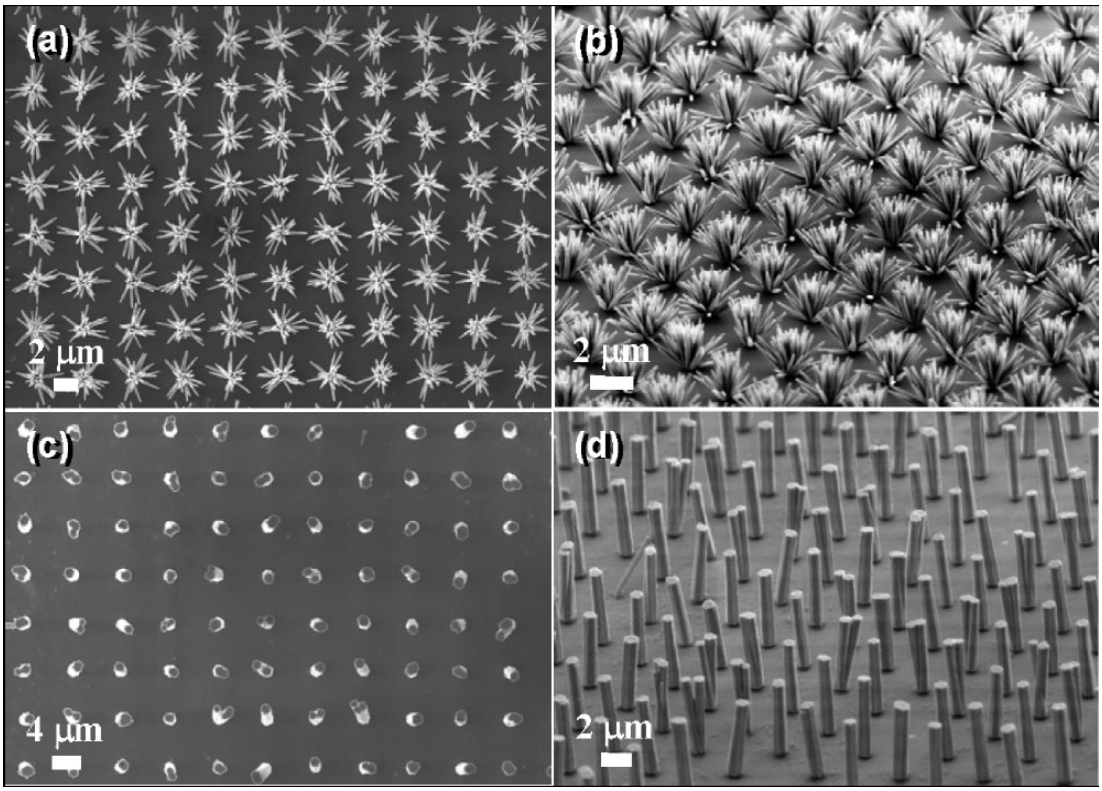

Figure 11. (a) Top view and (b) 60° tilt view of the ZnO nanowire arrays on a Si wafer grown at 70 ℃. (c) Top view and (d) 60° tilt view of the ZnO nanowire arrays on a Si wafer grown at 95 ℃.

To grow high-quality ZnO nanowire arrays for applications including sensor arrays, piezoelectric antenna arrays, LEDs, waveguides and high voltage nanogenerators, we need an approach that can meet the following three requirements. First, the growth has to be at low temperature so that it can be integrated with general substrates. Second, the nanowires have to be grown following a designed pattern, with a high degree of control in size, orientation, dimensionality, uniformity, and possibly shape. Finally, the catalyst should be eliminated for integration with silicon based technology.

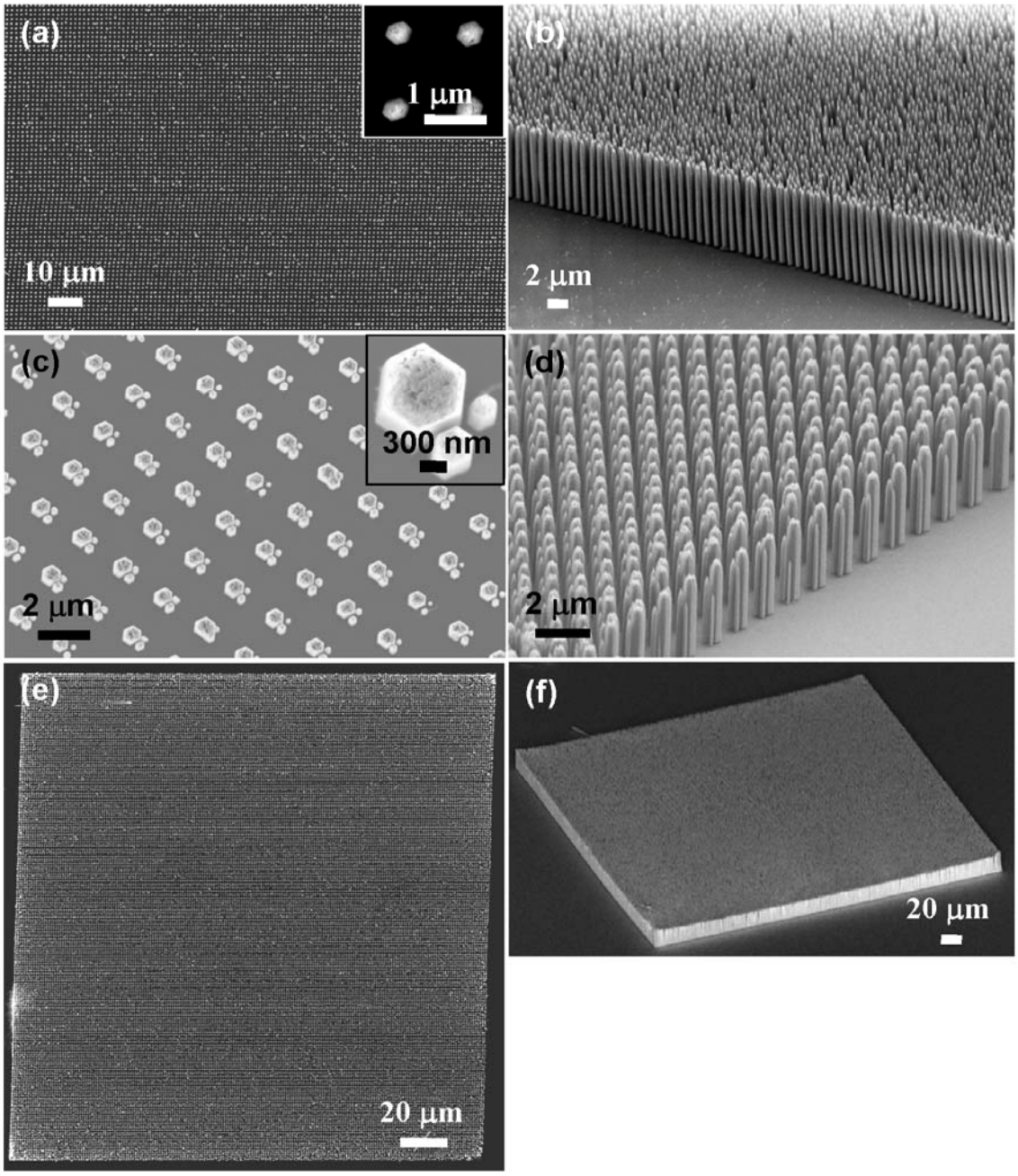

Figure 12. (a) Top view and (b) 60° tilt view of the ZnO nanowire arrays on a GaN substrate. (c) Top view and (d) 60° tilt view of the nanowires growing out of 400, 200, and 100 nm sized holes. Insets are enlarged top view image. Insets are enlarged top view of the nanowires. (e) Top view and (f) 60° tilt view of a 200 μm × 200 μm patterned nanowire arrays.

We demonstrated an approach that met all of these requirements.(*55*) Our method combined EBL and a hydrothermal method to achieve patterned and aligned growth of ZnO nanowires at <100 °C on general inorganic substrates, such as Si and GaN, without

using a catalyst (Figure 10). The non-epitaxial growth of ZnO nanowire arrays on Si wafers (or any other inorganic substrates) was assisted by a thin film of polycrystalline ZnO seeds. EBL was employed to generate a patterned mask, which was made of polymethyl methacrylate (PMMA), over the ZnO seed film. The hydrothermal growth mechanism has been elaborated above. Even though the substrate was annealed at 300 ℃ for 20 minutes, the ZnO seed film on the substrate was still composed of many tiny crystals with random in-plane orientations, ranging from several nanometers to tens of nanometers in size. The sizes of the EBL patterned openings in this study were all greater than 100 nm, in which a number of ZnO grains were exposed. Consequently, in most cases, multiple nanowires would grow out of one single spot, as illustrated in Figure 11(a) and (b). Under appropriate conditions, ZnO nanowires in close proximity are inclined to have coalescence effects.(*80*) In our experiments, by increasing the growth temperature from 70℃ to a relatively high growth temperature (95 ℃), those multiple nanowires from one single opening merged together, resulting in a thicker nanowire as shown in Figure 11 (c) and (d).

The epitaxial growth of aligned ZnO nanowire arrays on Si doped n-type GaN on a sapphire substrate(*81*) was performed in an analogous way as on a Si wafer. The lattice mismatch between Wurtzite GaN (0001) plane and Wurtzite ZnO (0001) plane is 1.8%, which led to a perfectly aligned growth of ZnO nanowire array, as shown in Figure 12 (a) and (b). Because the as-grown nanowires have a small diameter and a large aspect ratio, the sample needs a supercritical drying when the hydrothermal growth is complete.(*82*) Or else, when the liquid droplets on the nanowire arrays get evaporated and shrink in size, the surface tension of the droplet would sweep all the vertical nanowires down onto the substrate.

An interesting phenomenon was noticed when we compared the EBL pattern before hydrothermal growth with that after hydrothermal growth. Out of 100 nm sized holes the grown nanowires were 300 nm in diameters. The width of the nanowires was

three times the diameter of the holes. We proposed a two-step growing process for the ZnO nanowires. In the first step, the nanowire grew out of the photoresist hole with the same lateral dimension as confined by the hole. Then in the following step, there was no lateral confinement for it, and the nanowire could grow both vertically and laterally, but apparently faster in vertical direction than in lateral direction.

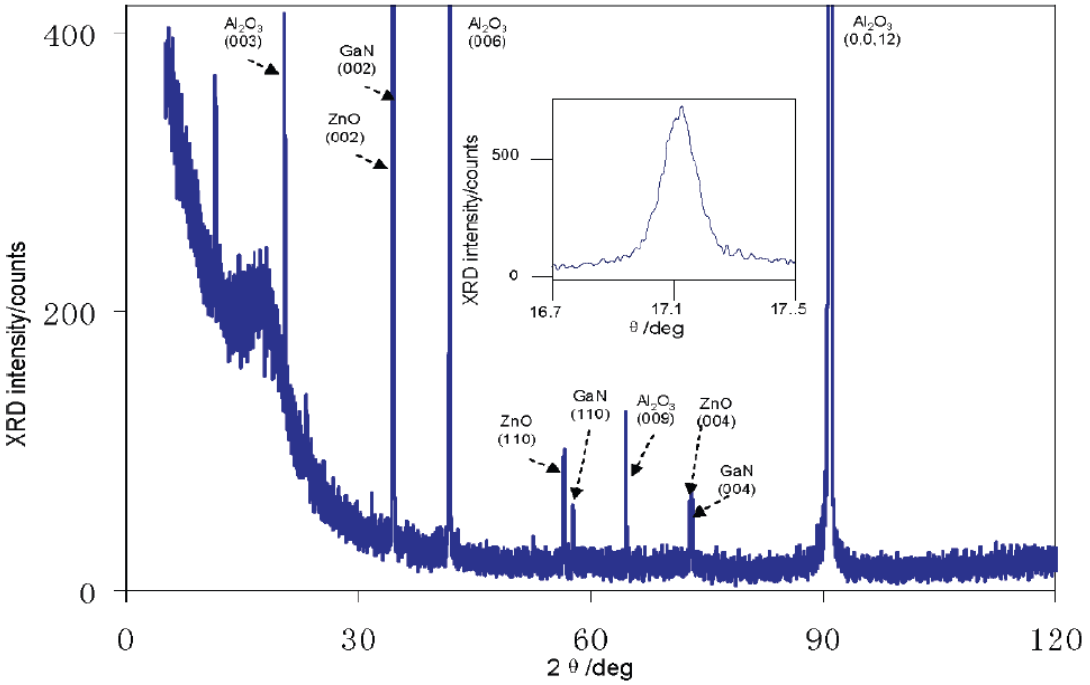

Figure 13. XRD pattern of the as-grown ZnO nanowire arrays on GaN (001). Inset is the ZnO (002) peak rocking curve.

Even though the nanowires would expand laterally when they grew out of the confining holes, we could still tune the width of the nanowires in a very responsive and reliable fashion. As shown in Figure 12 (c) and (d), when we made an array of circles with 400 nm, 200 nm and 100 nm in diameter, respectively, the developed nanowires showed proportional sizes to the holes accordingly. In addition, the pitch between the roles and columns of the pattern could also be straight forwardly varied for different application purposes. Even though the EBL method is said to be time consuming, the patterned growth could be easily scaled up with JEOL JBX-9300FS EBL system. As

shown in Figure 12 (e) and (f), a 200 μm by 200 μm sized ZnO nanowire arrays, with 100 nm in hole diameter and 1 μm in pitch could be finished within less than 2 minutes.

The crystal structure and vertical alignment of the as-grown ZnO nanowire arrays were examined by X-ray diffraction (XRD) pattern and rocking curve measurements. The θ-2θ scanning results of the sample are shown in Figure 13, where the main peaks have been labeled. In the inset of Figure 13 is the θ-rocking curve for the peak at 34.393° of the ZnO (002) plane. It exhibits a full width at half maximum (FWHM) value of 0.15°, which indicates almost perfect vertical alignment of the ZnO nanowires on the GaN substrate.

2.4 Patterned growth of horizontal ZnO nanowire arrays

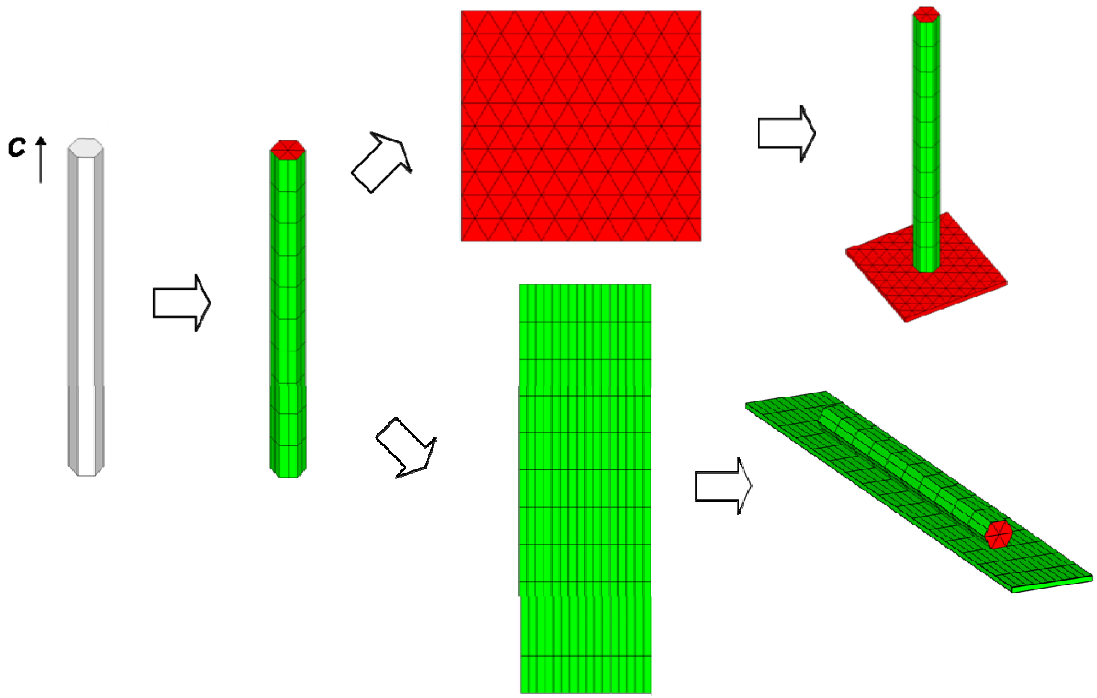

Figure 14. Illustration of epitaxial growth strategy for vertical and horizontal ZnO nanowire arrays, respectively.

As a counterpart of the vertically aligned ZnO nanowire arrays, horizontal ZnO nanowire arrays have as many important applications as the vertical arrays. But there is only limited research and progress in this area. Horizontally aligned ZnO nanowire arrays

have also been grown by a few approaches, such as growing ZnO nanowires out of pre-patterned side walls of a thin ZnO seed layer, or metal catalysts on planar alumina substrate by hydrothermal decomposition,(*85*) PVD,(*86-88*) or MOCVD.(*89*) But the horizontal nanowires were rather sparse and random in horizontal orientation,(*86, 89*) or of a poor horizontal alignment.(*85, 87-88*) Horizontal alignment of the ZnO nanowires after growth were also achieved by dispersing the nanowires into solvents then applying high frequency alternative electrical field.(*90*)

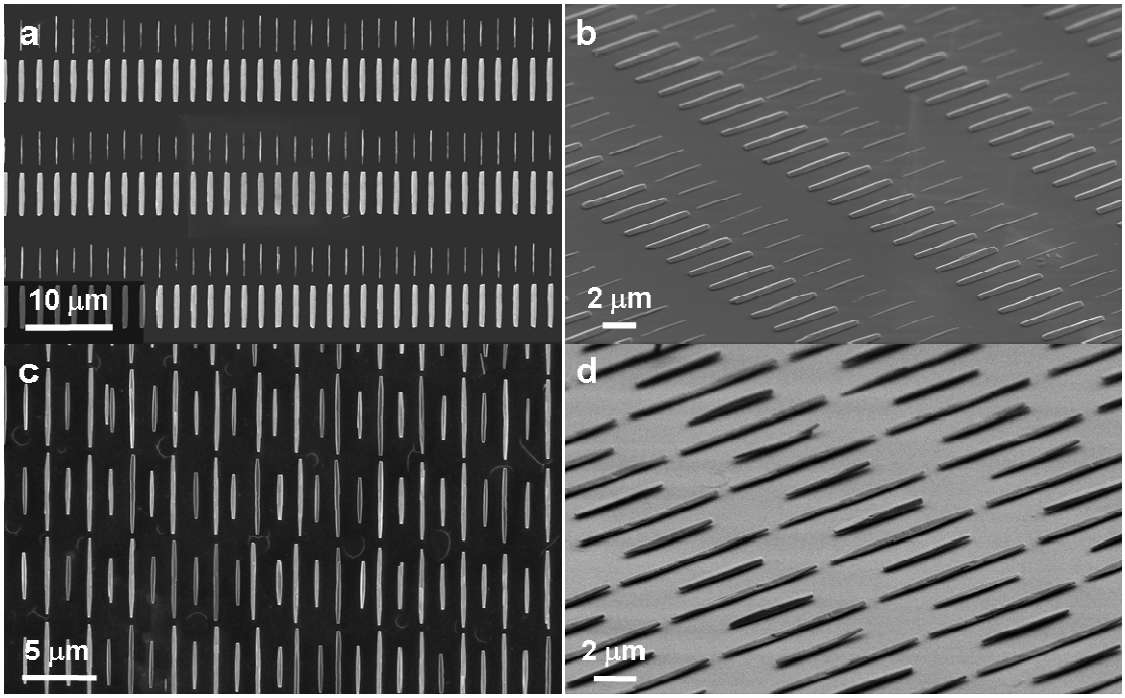

Figure 15. SEM images of horizontal ZnO nanowires of different widths and lengths. (a) Top view and (b) 30° tilted view of the thick nanowires, ~550 nm wide out of 200 nm photoresist openings, and thin nanowires, ~100 nm wide out of 50 nm wide photoresist openings. (c) Top view and (d) 30° tilted view of the long nanowires, ~7.5 μm in length out of 4 μm long photoresist openings, and short nanowires, ~4.5 μm in length out of 1 μm photoresist openings.

For wurtzite structured ZnO nanowires, they have intrinsic high energy ±(0001) polar surfaces terminated with Zn^{2+} plane and O^{2-} plane, respectively. These surfaces have high energy and have active sites, which the newly arrived precursor molecules are more likely to adsorb to, resulting in fast growth along <0001>. If we look from a crystal structure point of view, it has a six-fold symmetry at its top and bottom surfaces, and a

two-fold symmetry at its side surfaces, as illustrated in Figure 14 in different colors. So, if we have a six fold symmetry substrate, then the nanowire would grow vertically on the substrate. That's called epitaxial growth. Similarly, if we have a substrate that has a two-fold symmetry, then the nanowire would grow horizontally on the substrate.(*83-84*)

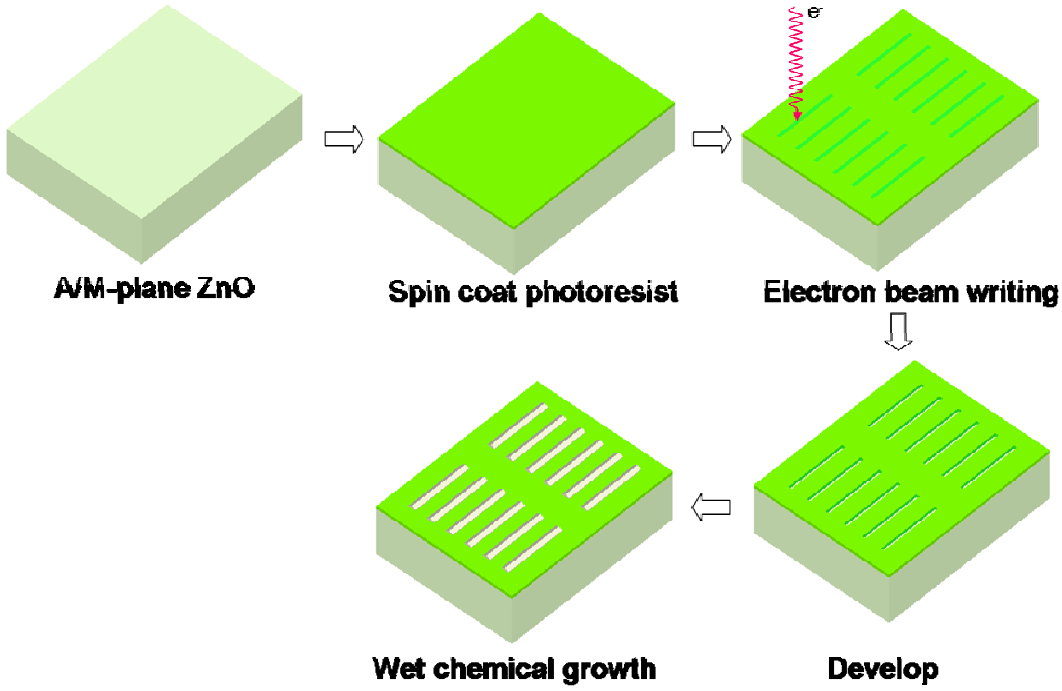

Figure 16. Flow chart growing patterned horizontal ZnO nanowire arrays on A/M plane single ZnO substrates. We spin coat a thin layer of photoresist first, then use electron beam to write patterns on the photoresist, and then put exposed photoresist into a developer. The photoresist where has been exposed by the electron beam is washed away, exposing the ZnO substrate underneath in the patterned areas only. Then when we put it into the growth solution, and horizontal ZnO nanowires grow out of the photoresist openings only.

To grow the horizontal ZnO nanowires, the single crystal ZnO ($2\bar{1}\bar{1}0$) substrate with photoresist was prepared and post treated by a standard process.(*55*) The patterns were defined by arrays of physical lines and rectangles with different lengths and widths, and also different orientations relative to the <0001> direction of the substrate. The line dose was ranged from 2.35 nC/cm to 2.55 nC/cm for the physical lines, and from 260 $\mu C/cm^2$ to 360 $\mu C/cm^2$ for the rectangles, as shown in Figure 16. Hydrothermal growth was conducted by a similar approach as described above.(*55*) The whole system was

heated up to different temperatures (80 ℃ or 85 ℃) for 2.5 hrs. After growth, it was let cool down to ambient temperature, and then was immersed in IPA to remove the absorbed water.

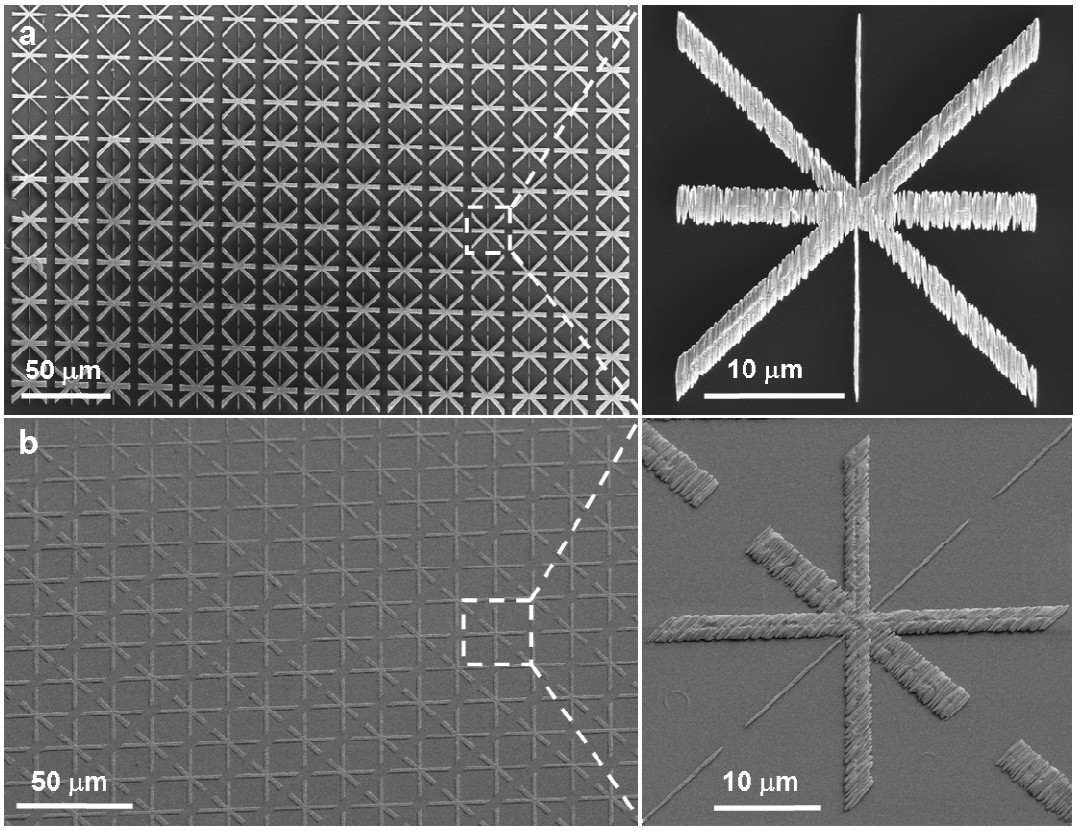

Figure 17. Illustration of the relationship between the ZnO nanowires growth direction and the photoresist openings orientation on the substrate. (a) Top overhead view and (b) 30° tilted view of the horizontal ZnO nanowire arrays growing out of an array of cross marks.

The growth morphology of the nanowires depends on the quality and structure of the substrate. Although <0001> stripe areas can be defined by EBL, a small miscut of the substrate along <0001> results in terrace along this direction. In such a case, the step edges with the (0001) facets can be the "mini" substrates for the growth. A direct growth of multiple nanowires out of the step edges formed one-directionally piled parallel nanowires. This was a multi-nuclei growth process.(*83*)

For wurtzite structured ZnO nanowires, along the *c* axis, they have intrinsic high energy polar surfaces such as ±(0001). Owing to the high energy of the polar surfaces,

the incoming molecules tend to favorably be adsorbed on the polar surfaces and get energy benefits from satisfying the dangling bonds, resulting in a fast growth along ±<0001> and the formation of low energy, non-polar $\{01\bar{1}0\}$ or $\{2\bar{1}\bar{1}0\}$ surfaces. This is how a nanowire structure is formed. In the PVD, the width of the nanowire is, in a lot of cases, dictated by the size of the catalyst particle and normally doesn't change with growth time, simply because the incoming molecular species are preferably adsorbed on the catalyst particle and the growth occurs at the interface between the particle and the solid nanowire.(*91*)

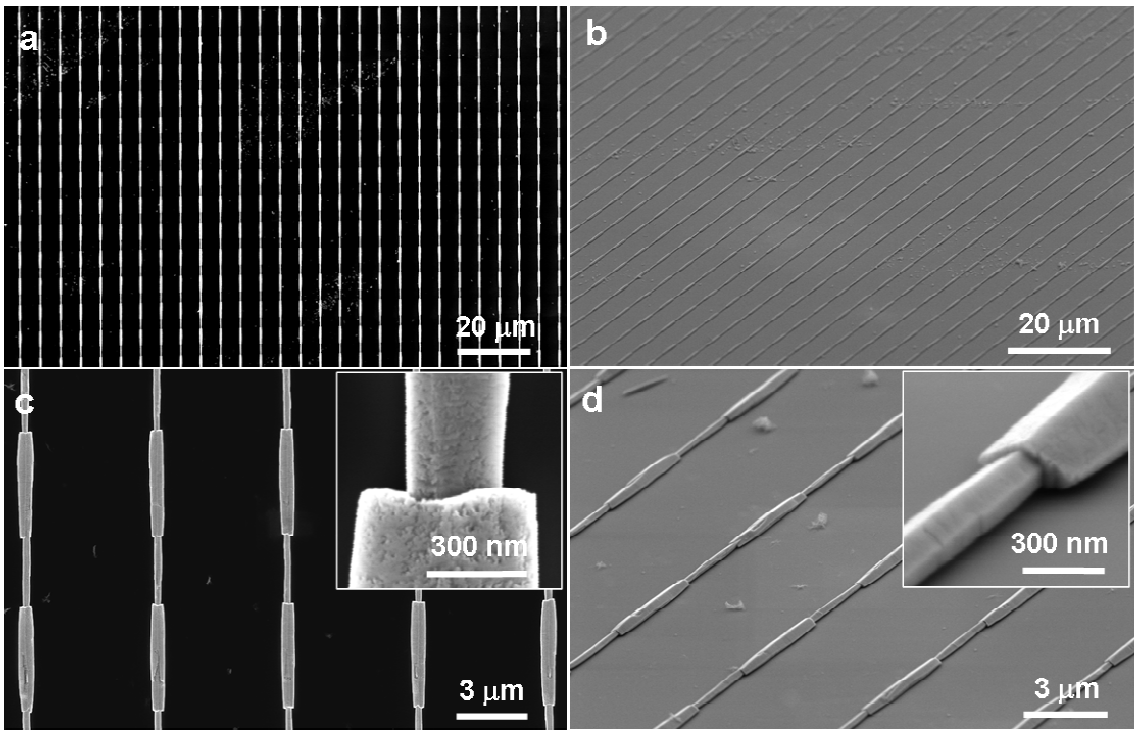

Figure 18. Horizontal ZnO nanowire arrays based two-segment monolithic superstructure. (a) Top and (b) 30 ° tilt over view of the superstructure. Enlarged (c) top and (d) 30 ° tilt view of the thin and thick nanowires connected together by lateral overgrowth. Inset images are enlarged view of the connection junctions.

But in the wet chemical method, as is always the case, size expansion is observed in both the vertical and horizontal directions when the nanowires are grown on photoresist pre-patterned substrates.(*55, 83, 92*) To put it in a different way, the dimensions of the ZnO nanowires grown by wet chemical methods are not only decided

by the physical confinement from the photoresist but also in fact established by the growth parameters/rates, such as the precursor concentration, the growth temperature and growth time. Generally speaking, low precursor concentration, high growth temperature and moderate growth time favor thin and high aspect ratio nanowires; low precursor concentration, low growth temperature and too long or too short growth time is inclined to produce thick and low aspect ratio nanowires.(*58*)

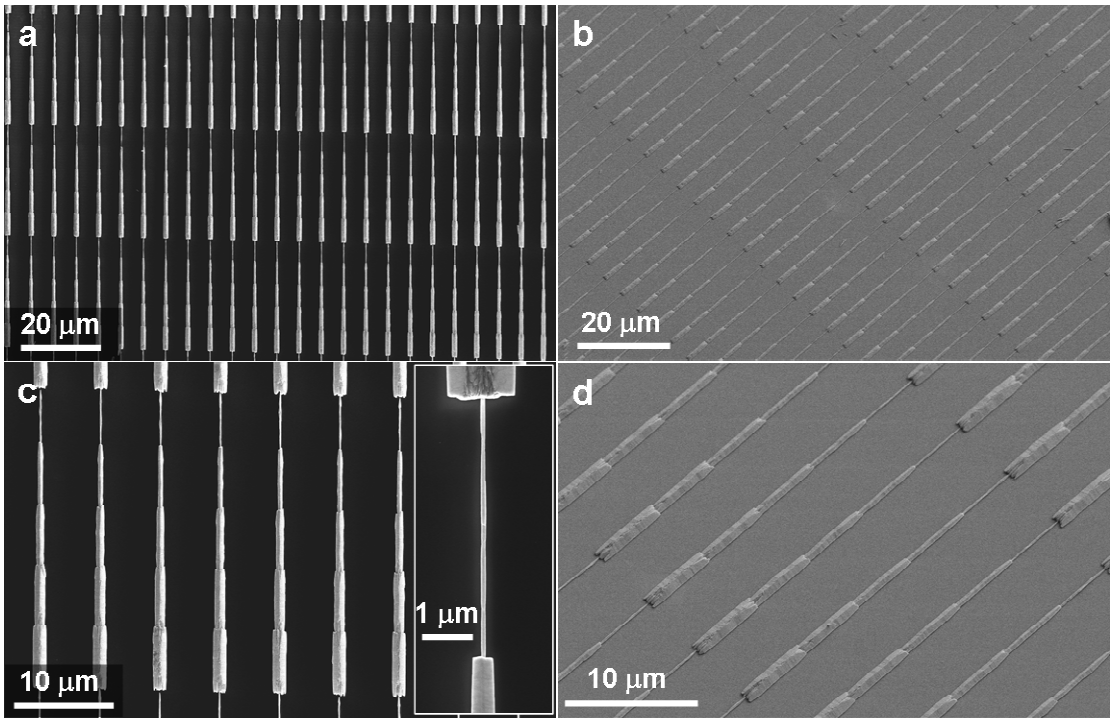

Figure 19. Horizontal ZnO nanowire arrays based five-segment monolithic superstructure. (a) Top and (b) 30 ° tilt view of the superstructure. Enlarged (c) top and (d) 30 ° tilt view of the five-segment superstructure. Inset image is enlarged view of a thin nanowire at the connection junction.

When out of the photoresist openings, the nanowires experience no physical confinement and could grow along both polar and non-polar axes, with different growth rate though due to the different adsorption rates and the slow diffusion of the precursor molecules at low temperatures. In our experiments, we found that out of 400 nm wide and 5 μm long photoresist openings, the as-grown nanowires were 1 μm wide and 13.2 μm long. The overgrowths in width and length were about 600 nm and 8.2 μm,

respectively. Nevertheless, as shown in Figure 15(a)-(d), we could still control the width and length of the nanowires effectively and efficiently by defining different sizes of the photoresist openings.(*55, 83*) We can clearly see that the size of the nanowires increases with enlarging the size of the photoresist openings, but they are apparently not in a linear relationship.

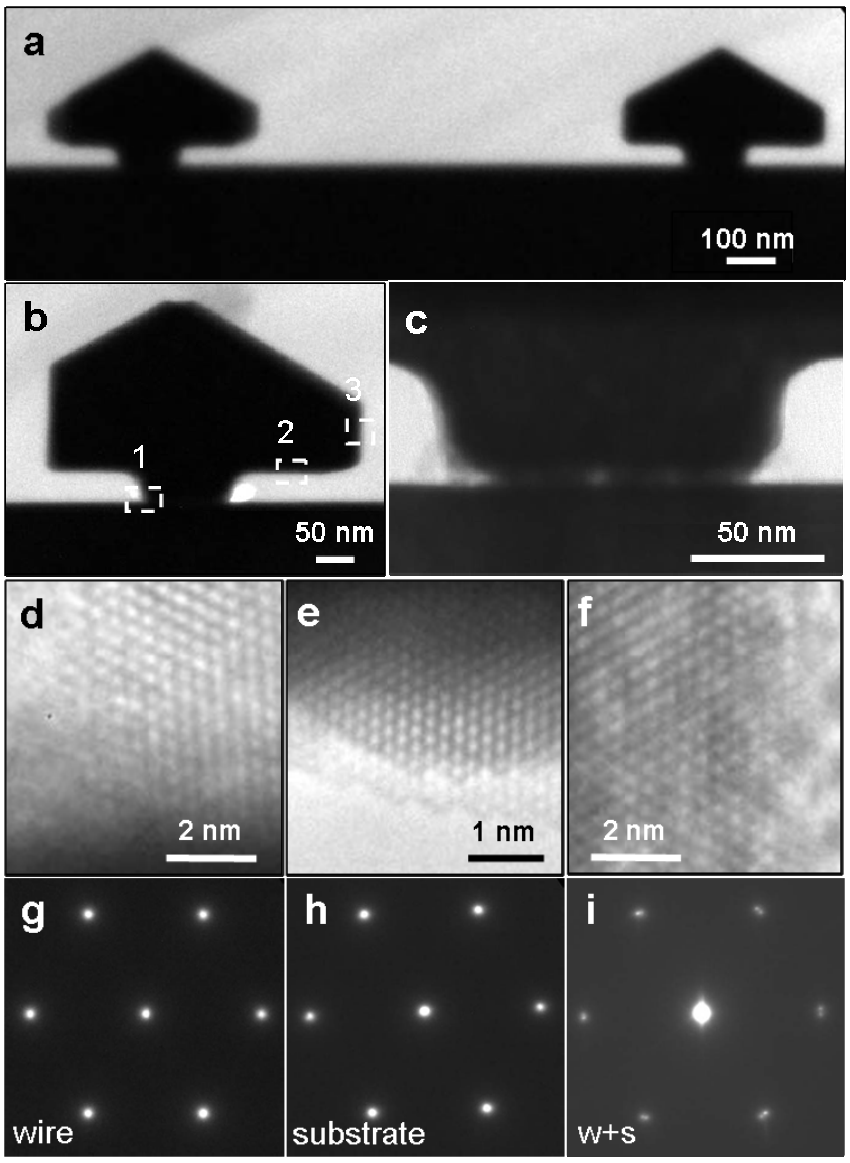

Figure 20. TEM cross section view of the horizontal ZnO nanowires with the substrate. (a) Overview of two adjacent nanowires. Enlarged view of (b) a nanowire and (c) the root area of the nanowire. HRTEM images of the areas (d) 1, (e) 2, and (f) 3 in (b), as indicated by the white dashed boxes. Selected area electron diffraction patterns of (g) the sole nanowire, (h) the sole substrate, and (i) the two together.

The substrate, A-plane ($2\bar{1}\bar{1}0$) single crystalline ZnO wafer, has the *c* axis lying inside the top surface plane, so we have to be careful about the orientation of the photoresist openings, parallel or perpendicular to the *c* axis. A cross-arm shaped opening pattern was first created by EBL on the substrate (Figure 17). Because the nanowires always grow along the *c* axis, for these photoresist openings parallel to the *c* axis, one opening gives rise to one nanowire; for these not parallel to the *c* axis, each and every single point along the openings could be considered as a seed, and gives rise to one nanowire, with approximately the same growth rates along both the *c* and –*c* directions, indicating that the growth rates along Zn-terminated [0001] and O-terminated [$000\bar{1}$] were about the same. In other words, the catalytic activities of the two polar surfaces were about the same for hydrothermal growth.(*83*) These nanowires pile up side by side together, forming a ZnO nanowire slab at high precursor concentration. The precursor concentration plays an important role here.(*58*) What we normally used is 5 mM, but when it goes to a relatively low level (1 mM), these side by side nanowires will not merge with each other. Instead of making strips, we can also make dotted patterns on the photoresist and each individual dot could be grown into a nanowire along the *c* axis.

We make use of the lateral overgrowth to make novel two-segment nanowire superstructures, as shown in Figure 18. To make the superstructures, we defined an array of photoresist openings with different widths separated from each other, e.g. a row of 50 nm wide photoresist openings, another row of 200 nm wide photoresist openings, and so on so forth. When the nanowires grow out of the photoresist openings, they tend to expand, and eventually merge or coalesce with each other (inset images show the junction regions), forming these continuous two-segment superstructures.

By the same methodology, we can make multi-segment nanowire superstructures, as shown in Figure 19, with the thinnest part only about 90 nm (inset image of Figure 19c) growing out of a 40 nm wide photoresist opening. Each and every individual segment has an epitaxial relationship with the single crystalline substrate, so the as-grown

continuous superstructures are considered to be monolithic single crystals. Of course, the separation between the photoresist openings should be moderate to match the amount of lateral overgrowth the nanowires could produce. The growth is very sensitive to the reaction temperature.(*58*) When the temperature is lower from 85℃ to 80℃, it changes from a well faceted thick nanowire to a pile of thin nanowires. Using this methodology, we could fabricate an array of ultra long ZnO nanowires with a length on the order of millimeters, and the width on the order of hundreds of nanometers, with an aspect ratio on the order of ten thousand. Compared with making an array of continuous ultra long photoresist openings, this also saves a lot of lithography exposure time. When fabricating these ultra long nanowires, as discussed above, we also need to be careful about the orientation of the photoresist openings.

The patterned horizontally aligned ZnO nanowire arrays could be straight forwardly scaled up for any practical applications. A 200 μm by 300 μm pattern could be generated by EBL in about five minutes.

2.5 Lift-off of the horizontal superstructures onto flexible substrates

Figure 20 depicts the cross section of the horizontal nanowires by transmission electron microscopy (TEM). Photoresist on the substrate has been removed by annealing at 500 ℃ for 30 min, which also helps improve the crystallinity of the nanowires from the rough surface morphology of the nanowires before annealing. Just as we expected, the cross section of the nanowire appears like a “mushroom” with the root about 100 nm wide, as defined by the size of the photoresist opening. The nanowire expands laterally forming two wings after growing out of the photoresist opening. The separation between the wings and substrate surface is about 50 nm (Figure 20(b)), which is the thickness of the photoresist. High resolution transmission electron microscopy (HRTEM) images around the nanowire clearly indicate that on the $(2\bar{1}\bar{1}0)$ surface of the substrate, the as-grown nanowire is enclosed by well defined $(01\bar{1}0)$ facets with a surface

roughness of less than 2 nm (Figure 20(f)). The selected area electron beam diffraction patterns from the sole nanowire (Figure 20(g)) confirm its growth orientation along the *c* axis, from the sole substrate (Figure 20(h)) confirm the orientation of the substrate, and from the two together, as shown in Figure 20(i), clearly indicate their epitaxial orientation relationship.

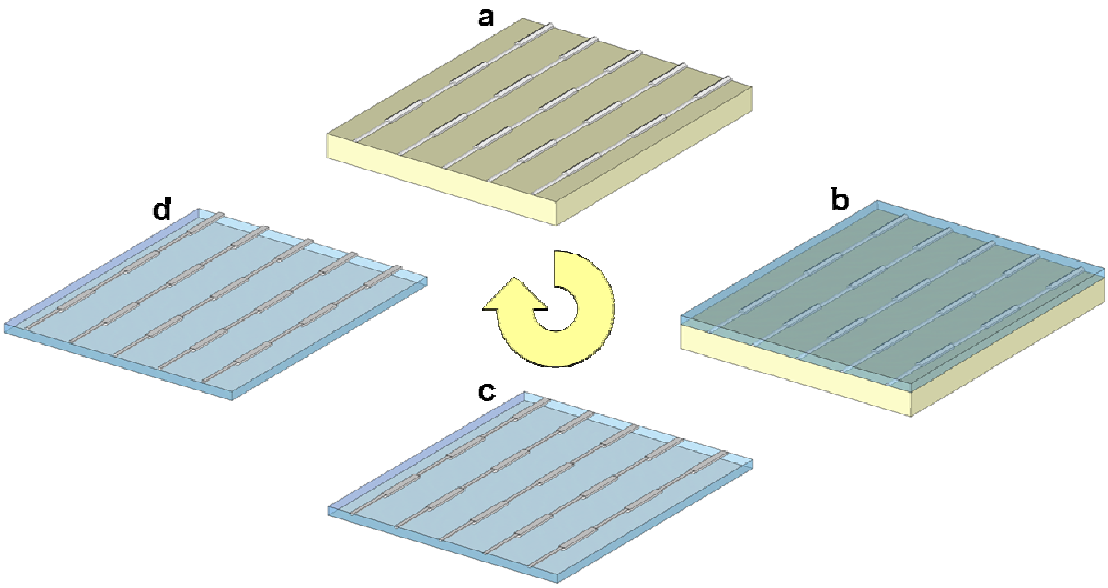

Figure 21. Schematic flow chart of transferring the horizontal nanowires from the ZnO substrate to flexible polymer substrate. We start from (a) a single crystal ZnO substrate with as-grown patterned horizontal ZnO nanowires, then (b) use a PMMA prepolymer glue to bond the existing PMMA photoresist, and then (c) lift the PMMA thin film off, and (d) finally do plasma etching on the PMMA to partially expose the horizontal nanowires.

The single crystalline ZnO substrate is not only mechanically rigid and brittle which prevents physical deformation from exerting on the nanowires, but also electrically conductive which obstructs us from fabricating electronic devices with the nanowires on it. We demonstrate an effective way of lifting off these horizontal nanowires and transferring them onto a mechanically flexible and electrically insulating polymer substrate.(*84*) By encapsulating the nanowire arrays with a polymer thin film, the horizontal nanowire arrays were lifted off and transferred onto flexible substrates (Figure 21).

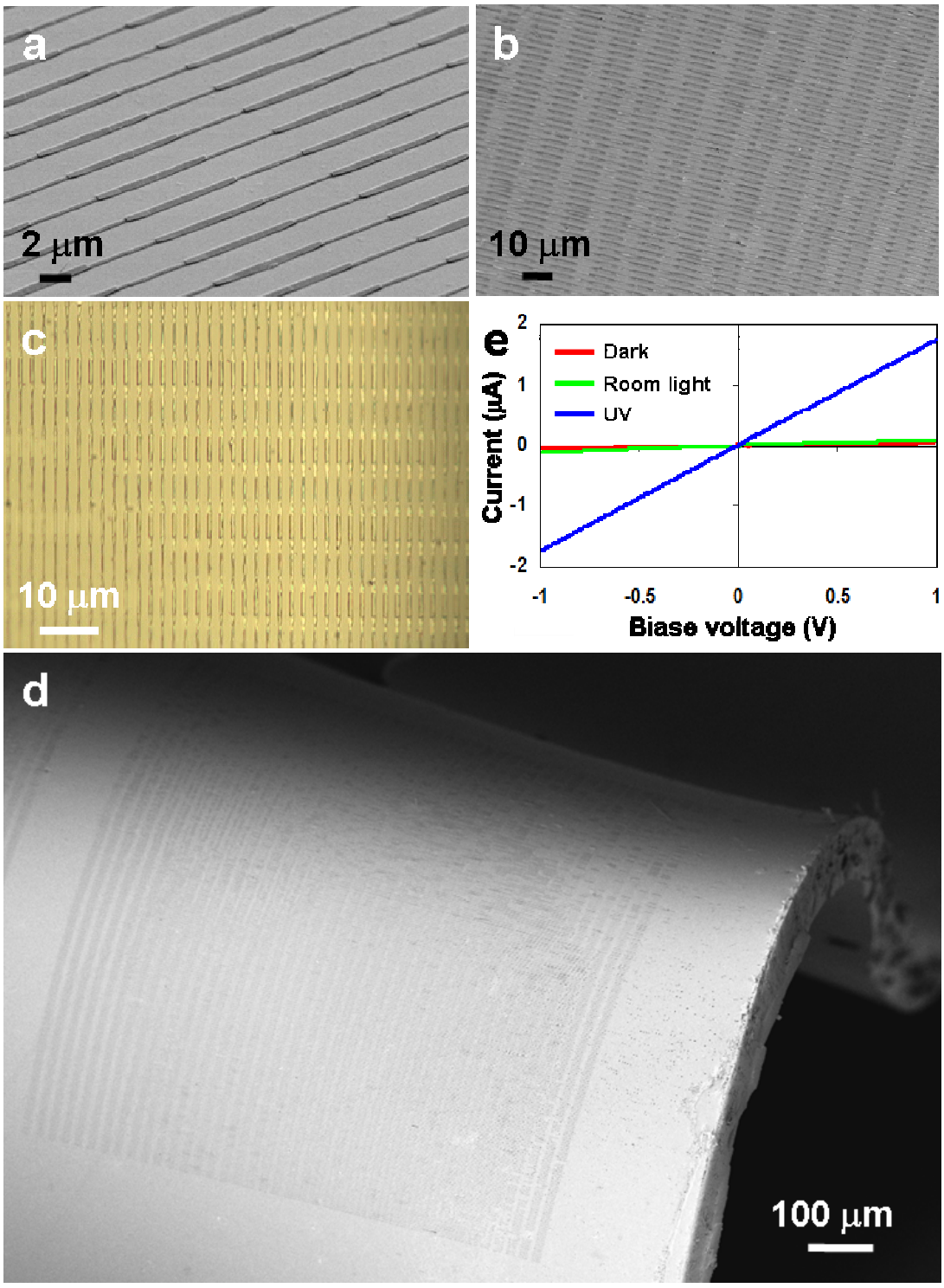

Figure 22. SEM images of the two-segment nanowire arrays (a) on ZnO substrate and (b) after transferring on flexible substrate. (c) Bright field optical image of the nanowire arrays on the flexible substrate. (d) Low magnification SEM image of the two-segment nanowire arrays on a flexible substrate. (e) I-V curves of the as-transferred nanowire arrays in dark environment (red), under room light (green), and under UV illumination (blue).

For the experimental process, a thin layer of PMMA prepolymer was used on the as-grown superstructures, which was prepared by heating methyl methacrylate monomer with 0.1% benzoyl peroxide at 95 ℃ for 15 min and then cooled down to room temperature. It is not necessary to remove the PMMA photoresist on the substrate simply because the prepolymer would form interfacial chemical bonds with the existing PMMA photoresist and give rise to a strong binding force between them. The viscosity of the prepolymer should be adequate so that it could form strong enough interface bonds, yet has sufficient fluidity to enclose all nanowires without leaving any possible bubbles behind. After that, the sample was kept at 50 ℃ for 10 h and 100℃ for 1 h to make the prepolymer fully polymerized which was about 100 μm in thickness. Then the ZnO nanowires were buried in the PMMA. After that the PMMA thin film was peeled away from the single crystalline substrate, and the horizontal nanowires were transferred onto the flexible PMMA thin film as shown in Figure 22b and 22c. Oxygen plasma was applied to etch a thin top surface layer of the PMMA thin film and to partially expose the buried nanowire arrays. This could be easily scaled up to a large area, as shown in Figure 22d.

Electrical transport properties of the as transferred nanowire arrays were characterized by making connection leads at two ends of the arrays using In metal that forms Ohmic contact. As shown in Figure 22e, the conductance of the arrays can be readily tuned by room light and UV light. Schottky contact is anticipated to have greater performance in this regard than Ohmic contact(*25-27*) and further study is still undergoing.

Such a structure could have many important applications in flexible electronics and portable nanodevices.(*93*) This approach shows great promise for many applications based on horizontal ZnO nanowires, including chemical and biological nanosensors, LEDs, optical gratings, integrated circuit interconnects, and high output power alternating

current nanogenerators. To the best of our knowledge, so far horizontal nanowire arrays based LEDs have never been demonstrated, whatever the materials are. Borrowing the similar idea from the horizontal epitaxial growth of ZnO on A-plane and M-plane ZnO substrate, we can also grow horizontal ZnO nanowire arrays on non-polar GaN substrate, by virtue of the similar structural and electronic properties of ZnO and GaN. The horizontal LED based on the non-polar GaN substrate is said to have less quantum confined Stark effects when the biased voltage goes up.(*94*)

CHAPTER 3

ORDERED NANOWIRE ARRAY BLUE/NEAR-UV LIGHT EMITTING DIODES

ZnO-based LEDs have been considered as a potential candidate for the next generation of blue/near-UV light sources,(*95*) due to the direct wide bandgap energy of 3.37 eV, a large exciton binding energy of 60 meV at room temperature, and several other manufacturing advantages of ZnO,(*96*) including the availability of large area substrates at a relatively low cost, amenability to wet chemical etching, great tolerance to high energy radiation, and long-term stability. They have great potential for a variety of technological applications, such as solid state lighting, optical interconnect, and high density information storage, etc. While the pursuit of stable and reproducible p-ZnO is still undergoing,(*97*) heterojunctions of n-ZnO and p-GaN are employed as an alternative approach in this regard by considering the similar crystallographic and electronic properties of ZnO and GaN.(*98-100*) Compared with the n-ZnO thin film/p-GaN thin film LEDs,(*20, 96, 101-106*) which may suffer from the total internal reflection, n-ZnO nanowire/p-GaN thin film heterostructures are utilized in order to increase the extraction efficiency of the LEDs by virtue of the waveguiding properties of the nanowires.(*107-109*) But in all of these cases, the n-ZnO nanowires are randomly distributed on the substrate, which largely limits their applications in high performance optoelectronic devices.

We demonstrated the capability of controlling the spatial distribution of the blue/near-UV LEDs composed of position controlled arrays of n-ZnO nanowires on a p-GaN thin film substrate.(*21*) The device was fabricated by a conjunction of low temperature wet chemical methods and EBL.(*55*) Under forward bias of the p-n junction,

each single nanowire is a light emitter. By Gaussian deconvolution of the emission spectrum,(*110-111*) the origins of the blue/near-UV emission are assigned particularly to three distinct electron-hole recombination processes. And in addition, by virtue of the nanowire/thin film heterostructures, these LEDs give an external quantum efficiency of 2.5 %. This approach has great potential applications in high resolution display, optical interconnect, and high density data storage.

3.1 Fabrication and characterization of the heterostructural LED

The design of the LED is shown in Figure 23(a). Ordered ZnO nanowire arrays were grown on p-GaN (Figure 23(b)-(d)).(*55, 58, 112*) The morphology of the ZnO nanowire arrays was characterized by LEO 1550 SEM. The capability of controlling the positions of the nanowires on the substrate allows us to fabricate nanoscale light emitters in a controllable pattern.(*101*) Ohmic contacts to the bottom p-GaN and top n-ZnO nanowires were made by depositing a 30-nm by 30-nm layers of Ni/Au by electron beam evaporation on the p-GaN followed by rapid thermal annealing in air at 500 ℃ for 5 min. Ohmic behavior was confirmed by their individual I-V curves, and the rectifying I-V curve comes only from the p-n diode herein. A 50-nm conformal layer of SiO_2 was deposited onto the nanowire arrays by plasma enhanced chemical vapor deposition. After that, a relatively thick layer of PMMA was carefully spun coated onto the substrate to wrap around the nanowires. During this process, the SiO_2 layer protected the nanowires from falling down onto the substrate due to the surface tension of the PMMA. Then oxygen plasma was applied to etch away the top part of the PMMA followed by reactive ion etching (RIE) to remove the top SiO_2, exposing the tips of the nanowires. Since the oxygen plasma and RIE were only applied to the tip part of the nanowires, the damage/deterioration they might have induced to the electrical and optical properties of the nanowires could be neglected. Then, a 100-nm layer of ITO was sputtered as the top common electrode of nanowires.

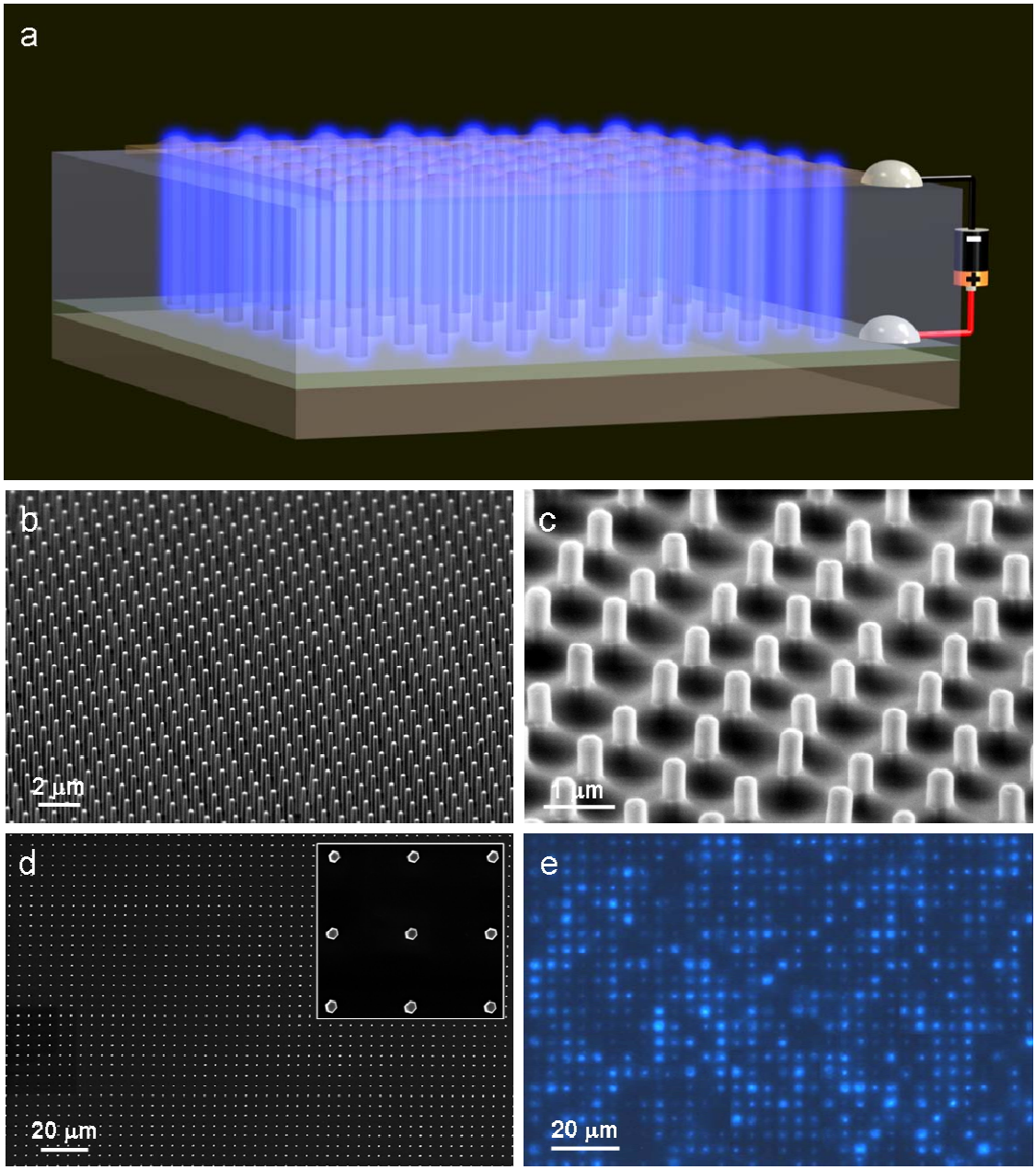

Figure 23. (a) Design overview of the LED. (b) 60° tilt SEM view of the as-grown patterned vertical ZnO nanowires with a width about 300 nm and (c) after they are wrapped with PMMA and the tips are exposed. (d) Top SEM image of the ZnO nanowire arrays. The pitch and layout of the nanowire arrays are readily controlled by the EBL. (e) The optical image of a turned on LED (artificial bluish color).

3.2 Electroluminescence characterization of the as-fabricated LED and peak deconvolution

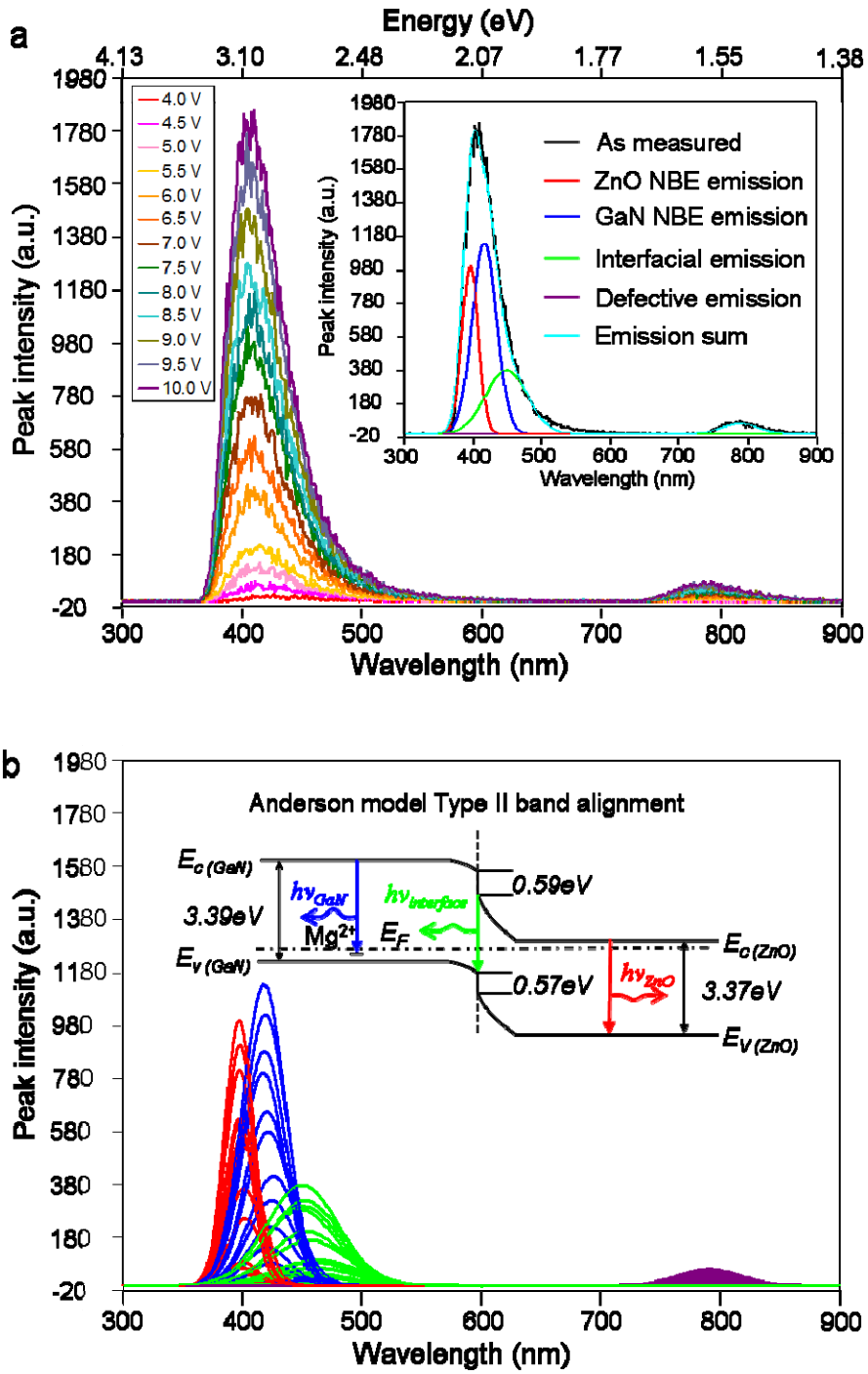

Figure 24. (a) EL spectrum as a function of the forward biased voltage. Inset shows by Gaussian deconvolution analysis the blue/near-UV emission could be decomposed into three distinct bands that correspond to three different optoelectronic processes. (b) All of the four emission bands evolve (band width, height, and intensity) as a function of the biased voltage. Inset schematics show the band diagram of the n-ZnO/p-GaN heterojunction under no or small biased voltage, where the three emission bands comprising the blue/near UV light are specifically indicated in different colors.

The forward biased voltage was applied by Semiconductor Characterization System Keithley 4200. The optical image of the blue/near-UV light was recorded under Nikon Eclipse Ti inverted fluorescence microscope with 9 s exposure time and a gain value of 1. Figure 23(e) is the optical image of a lighted up LED at a biased voltage of 10 V. In the device, all of the nanowires are connected in parallel and each single nanowire is a light emitter. Brightness difference among the individual nanowires comes probably from the current crowding effect and different serial contact resistances therefore different injection currents through the individual nanowire. The pitch between each lighting spot shown in Figure 23(e) is 4 μm and the resolution is 6350 dpi.

The EL spectrum was measured on a Master Systems Felix32 PTI fluorescence detector. When measuring the EL spectrum, the device was let cool down before doing another measurement so the possible thermal effect could be ignored. The physical origin of this electroluminescence (EL) has been extensively studied but is still under debate.(*111, 113*) As shown in Figure 24(a), emission spectrum of the as-fabricated LED was monitored at different biased voltages/injection-currents at room temperature. We can see that, from 4 V to 10 V, the contour of the EL spectrum does not change much with the biased voltage. The dominant emission peak is slightly blue shifted in the range of 400 nm - 420 nm with a FWHM of about 60 nm. The peak intensity versus injection current ($L - I^m$) characteristics have been acquired, showing a superlinear relationship with m=1.3. Peak-deconvolution with Gaussian functions, inset picture in Figure 24(a), shows that the broad spectrum consists of three distinct bands (Figure 24(b)) centered in the range of 395-415 nm, 420-440 nm, and 450-510 nm, respectively, and each emission band corresponds to a particular recombination process as elaborated in the following. The fitting of the EL spectrum was performed using the Microcal Origin software. The near-UV emission band centered at around 400 nm is attributed to the near band edge (NBE) emission in ZnO nanowires that originates from the recombination of ZnO free and bound excitons. Whereas the red shifted violet emission band centered at about 430

nm is ascribed to the transitions from the conduction band or shallow donors to deep Mg acceptor levels in the p-GaN thin film substrate.(*96, 114-115*)

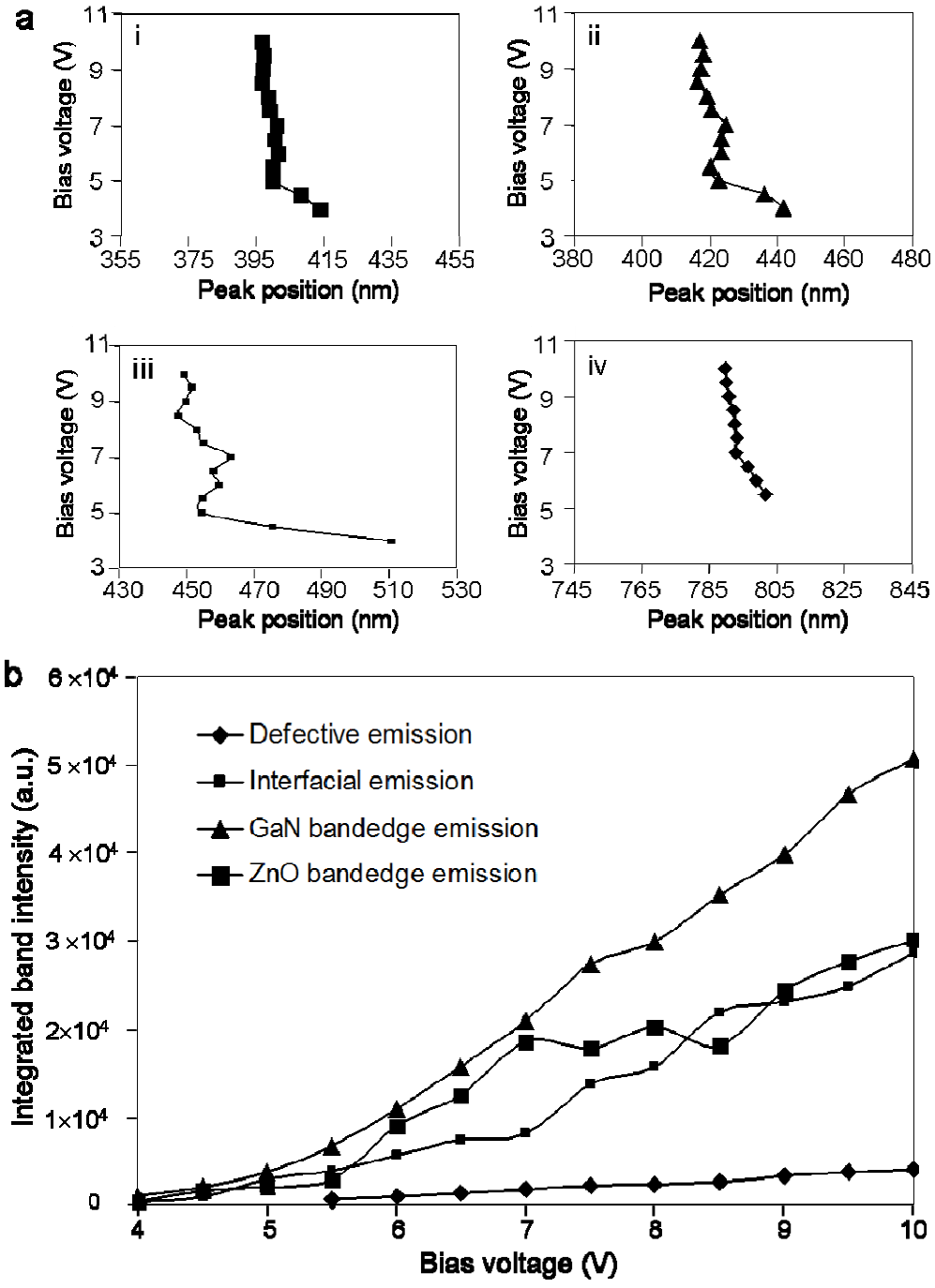

Figure 25. (a) Peak positions blue shift as a function of the biased voltage for (i) ZnO NBE emission, (ii) GaN NBE emission, (iii) interfacial emission, and (iv) defective emission. (b) The integrated emission bands intensity as a function of the biased voltage. For the defective emission, when the biased voltage is below 5.5 V, it is hardly distinguished from the noise level.

There has been a controversy about whether the emission is from the n-ZnO side(*101, 116*) or the p-GaN side.(*96, 115*) Here, from our observation, both scenarios have made contributions. In reality, the hole concentration in the Mg-doped p-GaN substrate ($p\sim10^{18}$ cm^{-3}) is higher than the electron concentration in the n-ZnO nanowire ($n\sim10^{17}$ cm^{-3}), but the carrier mobility in the p-GaN is smaller than that in the n-ZnO. The barrier heights at the interface for the holes (0.57 eV) and for the electrons (0.59 eV) are comparably equal. In that case, the charge injection by electrons and holes should be comparable from both sides. Of course, the energy band offset at the ZnO/GaN interface is likely to be determined by the fabrication process.(*117*) The blue emission around 460 nm is related to the radiative interfacial recombination of the electrons from n-ZnO and holes from p-GaN.(*20, 114, 118*) The interface states generally act as nonradiative centers that annihilate free electrons and holes. Therefore, it is required to get high quality interface between the heterojunctions in order to get high efficiency LEDs. The weak red emission at around 790 nm is coming from the native deep level point defects (oxygen vacancies and zinc interstitials) in ZnO nanowires.(*115*)

As the biased voltage is increased, intensity of the main peak and all of the four sub-bands (including the defect emission) exponentially increases and also blue shifts (Figure 24(b)). The blue shift has been explained to be caused by several different mechanisms, such as band renormalization and band filling,(*119*) and the screening effect of the built-in piezoelectric field.(*120*) Here in our experiment, the blue shift of the emission peak comes from two resources: the blue shift of sub-band positions (Figure 25(a)), and the change of relative intensities of the sub-bands at different injection currents (Figure 25(b)).(*114*) The blue shift of the ZnO and GaN NBE emission positions (Figure 25(a) i and ii) may be caused by the recombination of increasing kinetic energies of electrons and holes as the biased voltage is increased, assuming the mobility of the carriers does not change too much when the biased voltage is not too high, and that could contribute to the energy of the emitted photons. The most obvious blue shift of the peak

position comes from the interfacial recombination process (Figure 25(a) iii), which could be understood from the band diagram. As the biased voltage is increased, the gap between the two quasi-Femi levels is increased, and the interfacial recombination energy of the electrons from ZnO side and holes from GaN side goes up.

The blue shift of the EL spectrum also comes from the change of the relative intensity of the three bands, as shown in Figure 25(b). The intensity of the GaN NBE emission increases comparatively faster than the ZnO NBE emission and the interfacial emission. As the biased voltage is increased, the band bending of the p-GaN and n-ZnO is reduced, therefore the kinetic energy of the electrons and holes is increased and they have much higher probability to go across the interface barrier and recombine at the other side. As we compare the curve for ZnO NBE and the one for GaN NBE emissions (Figure 25(b)), at low biased voltages (< 7.0 V), the ZnO NBE emission has a competitive intensity with the GaN counterpart. As the biased voltage goes up, the ZnO NBE emission falls behind the GaN. In comparison with the high quality GaN thin film fabricated by MOCVD, the relatively high level of native defects with the hydrothermally grown ZnO nanowires could undermine its internal quantum efficiency. These point defects in the ZnO nanowires perform like trapping centers and give rise to nonradiative recombinations.

3.3 External quantum efficiency of the heterostructural LED

As the flat thin film based LEDs are suffering from the low light extraction efficiency as limited by the total internal reflection, extensive research efforts have been made in this regard, such as roughing the surface of the emitting thin film,(*121*) reshaping the geometry of the LED architecture,(*122*) utilizing resonant cavity,(*123*) coupling with surface plasmon,(*124*) and fabricating photonic crystal structures,(*125*) etc. Among these approaches, nanowire/thin film heterostructures are proposed to be a promising method

considering the feasible waveguiding properties of ZnO nanowires.(*105, 107-108, 126-128*)

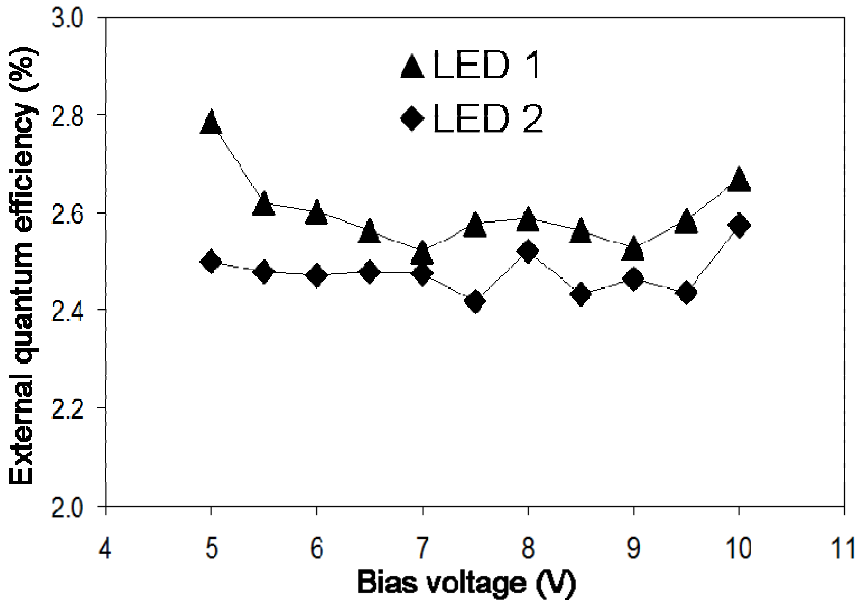

Figure 26. External quantum efficiencies of two heterostructural LEDs as a function of the biased voltage/injection current. The efficiency was determined only when the LED was turned on and the light output power was stably registered with the power meter.

Under the single mode waveguide cavity conditions,

$V = 2\pi \frac{a}{\lambda_o}\left(n_1^2 - n_2^2\right)^{\frac{1}{2}} = 2.405$,(*108*) 86.5 % of the light would be confined within a 223 nm nanowire, where V is the single mode cut-off value, a is the diameter of the nanowire, λ_o is the free space wavelength of the propagating light (here we set it to be 400 nm), and n_1 (2.10) and n_2 (1.59) are the effective refractive index of the ZnO nanowire and the cladding PMMA thin film, respectively. To note, the facets of the nanowire are assumed to be perfectly flat under the single mode conditions. But in reality, these nanowires have rounded tips (Figure 23(c)), a large surface to volume ratio, and thus a high density of surface states near the band edge, which allows a great reduction of the back reflections at the ZnO nanowire surfaces, known as the omnidirectional reflector effect.(*129*) Besides, based on an effective medium theory, these graded refractive

indices of GaN (2.49), ZnO (2.10) and PMMA (1.59) could largely reduce the Fresnel reflection between GaN/ZnO and ZnO/PMMA interfaces, which helps the optical transmission.

By virtue of these advantages, the light could easily be extracted out through multiple scattering. ZnO have a transmittance of over 90% in the visible range,(*107*) so the self-absorption of the nanowires should not be the major concern. To take one step further, the patterned ZnO nanowire arrays form a two-dimensional photonic crystal, which has an optical bandgap for the light travelling parallel to the surface of the substrate. So by controlling the periodicity of the nanowire arrays, it may be possible to match the wavelength of the emitted light to the bandgap of the photonic crystal, possibly resulting in normal directional emission of the light.

Figure 26 shows the room temperature external quantum efficiency versus d.c. injection current characteristics. The external quantum efficiency of the LEDs was measured using a power meter (OPHIR, NOVA-ORIEL, P/N 1Z01502) and a light detector (OPHIR, 3A-P-SH-V1, P/N 1Z02622). The external quantum efficiency was calculated by acquiring the ratio of the output light power and the input electrical power. As we clearly see, the external quantum efficiency of the LED is about 2.5 %, which is considerably high for a single p-n junction based LEDs, and such data are reproducible and consistent for several devices. As the biased voltage/injection current is gradually increased, the external quantum efficiency becomes steady, which indicates that the serial resistance or the nonradiative recombination through the defects, e.g. Auger recombination, does not increase in proportion with increasing the injection current.

CHAPTER 4

HIGH POWER OUTPUT THREE-DIMENSIONAL NANOGENERATORS

Building self-powered nanosystems is a future direction of nanotechnology. A nanosystem is an integration of nanodevices, functional components and a power source. The search for sustainable micro/nano-powering sources for driving wireless and mobile electronics is an emerging field in today's energy research, which could offer a fundamental solution to the energy needed for driving nanodevices/nanosystems, for its independent, wireless, and sustainable operation.(*130-132*) In particular, ZnO based piezoelectric nanogenerators are a promising approach for harvesting small environmental vibrations.(*32-34, 36, 133*)

4.1 Multilayered three-dimensional direct current nanogenerator fabricated by using paired nanotip-to-nanowire brushes.

The previously developed nanogenerator was based on a vertically aligned ZnO nanowire array that was placed beneath a zigzag electrode with a small gap.(*134*) The nanogenerator relied on the piezoelectric potential created in a nanowire once subject to elastic straining, which drove the flow of charge carriers.(*135*) The zigzag electrode acted as an array of parallel integrated tips for simultaneously creating, collecting and outputting electricity from all of the active nanowires. In this design, the non-uniform heights and random distribution of the nanowires on substrate, however, might prevent a large fraction of nanowires from contributing to the energy conversion process; a bottleneck technology in the application of nanogenerators is the output power, especially the output voltage, which is dictated by individual nanowires. The output current of the

nanogenerator is a sum of those contributed by all of the active nanowires, while the ultimate output voltage is determined by individual nanowire. The packaging technology was of critical importance to keep the gap distance between the zigzag electrode and the nanowire arrays just right so that it was large enough to allow the nanowires to be freely bent/deflected, but small enough to ensure an intimate contact between the nanowires and the electrode.(*136-137*)

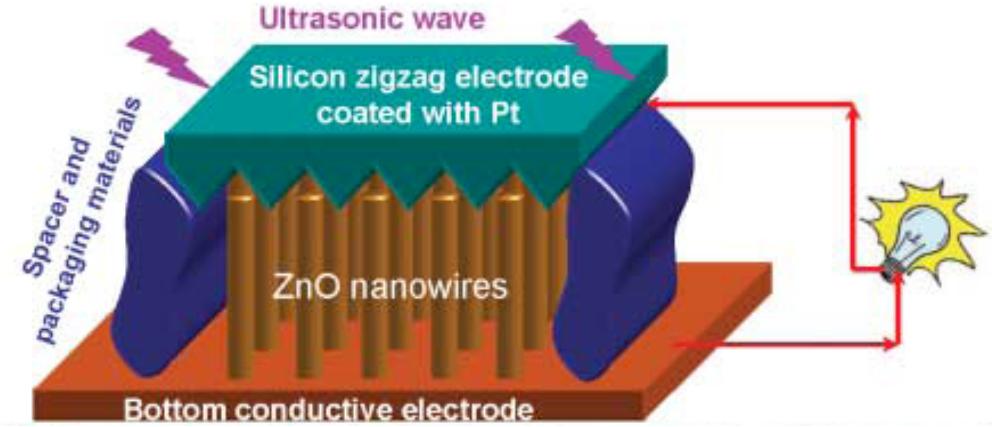

Figure 27. Schematics show the design and structure of a high output power nanogenerator. Patterned ZnO nanowire arrays grown on a general substrate are covered by a geometry matched zigzag electrode.(*33*)

Motivated by bottleneck of the direct current nanogenerator explained above, we need to fabricate position defined ZnO nanowire arrays on the substrates to match the shape and morphology of the top zig-zag electrode very well, and this would eventually increase the number of active nanowires for participating electricity generation, as shown in Figure 27. This approach requires growth of patterned ZnO nanowire arrays over a large area. Also, the zigzag top electrode and the bottom ordered ZnO nanowire array needs to be well aligned up.

Alternatively, instead of using the patterned growth of ZnO nanowire arrays as the bottom electrode and the zigzag Pt coated Si trenches as the top electrode, we demonstrated a new approach to this class of nanogenerators which is composed of integrated, paired nanobrushes made of metal coated ZnO nanotip arrays and bare ZnO nanowire arrays (Figure 28).(*35*)

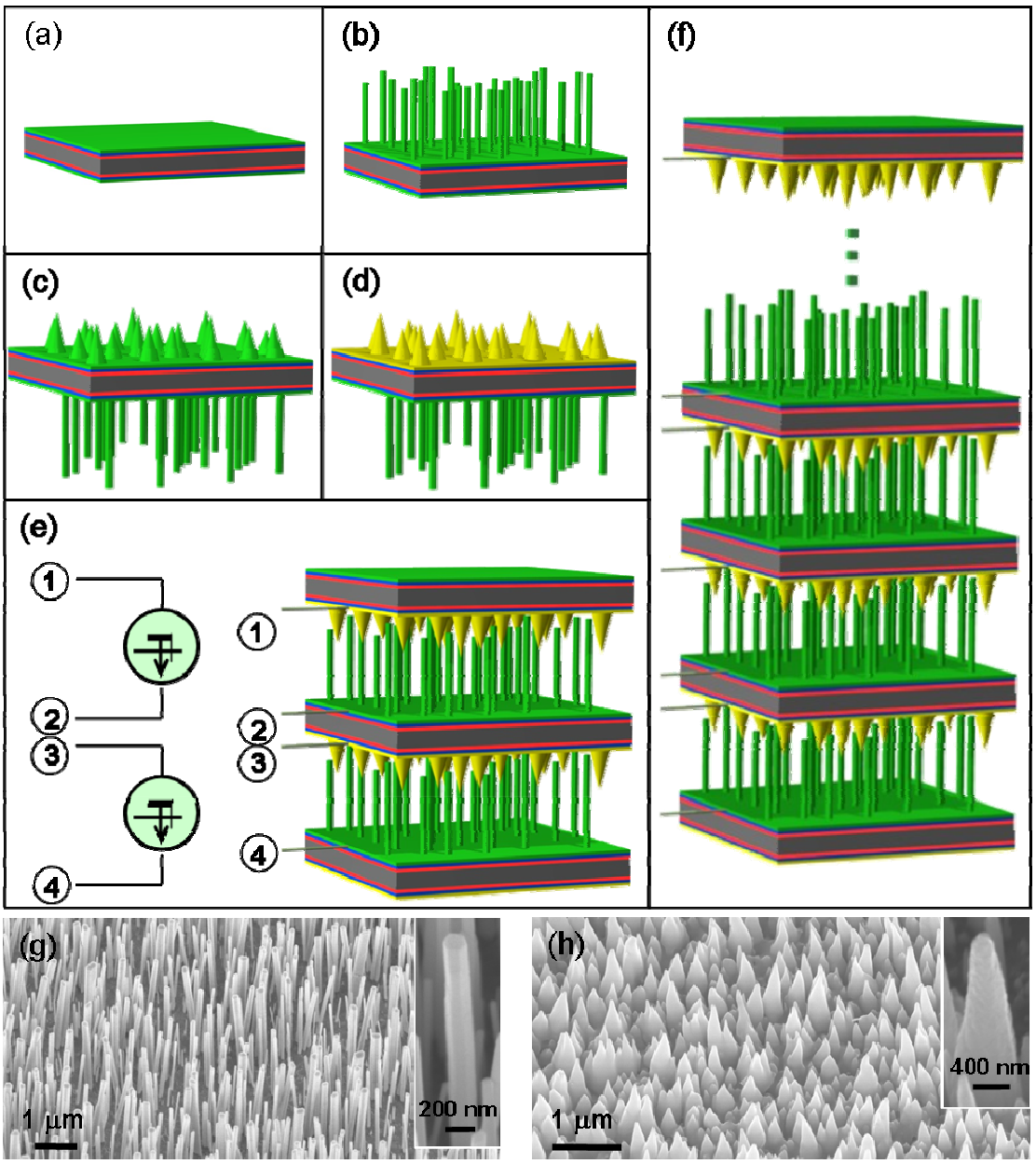

Figure 28. Design and fabrication procedures of the multilayered nanogenerators and rational growth of ZnO nanowire and nanotip arrays. (a) The as fabricated substrate after coating with the $Zn(CH_3COO)_2$ seed layer. (b) Growth of hexagonal-prism-shaped nanowire arrays by wet chemical method on one side. (c) Growth of pyramid-shaped nanotip arrays on the other side. (d) Coating the nanotip arrays with an Au layer by magnetron plasma sputter. (e) Two-layered nanogenerator made by stacking three layers of the wafer structures shown in (d), with the Au-coated nanotip arrays facing and interpenetrating the bare nanowire arrays. The right-hand side is the designed symbol for representing the nanogenerators. (f) A multilayered three-dimensional nanogenerator integrated by stacking multiple layers of wafer structures. (g) 60° tilt view SEM image of the hexagonal-prism-shaped ZnO nanowire arrays grown by chemical approach. (h) 60° tilted view SEM image of the pyramid-shaped ZnO nanotip arrays grown by chemical approach. Inset SEM images are high magnification views of a single nanowire and nanotip.

The nanotip and nanowire arrays were rationally synthesized on the two surfaces of a common substrate using the chemical method previously developed and described above. The operation of the nanogenerators relied on mechanical deflection of the nanowires but not the resonance of the nanowires as required by previous nanogenerators. This largely expanded the application of the nanogenerators from a low frequency domain (hertz range) to a relatively high frequency domain (megahertz range). Furthermore, through layer-by-layer stacking of the devices, high output direct current was generated by exciting the architecture with ultrasonic waves. A four-layer integrated nanogenerator was demonstrated to generate an output power density of 0.11 μW/cm^2 at 62 mV. The layer-by-layer assembly provides a feasible technology for building three dimensional nanogenerators for applications where force or pressure variations are present, such as a shoe sole, an underskin layer for airplanes to harvest turbulence, and next to a vibration source such as a car engine or tire.

The density of the ZnO nanowires and nanotips plays a critical role in the current generating process. If it is too high, when the nanowire is bent the nanotip, the nanowire would probably touch an adjacent nanowire, which would result in charge leakage and undercut the charge accumulating process. This would in the end decrease the voltage output of the nanogenerator. If the density is too low, then the output power density of the nanogenerator would be rather limited. So, we need to optimize the chemical growth parameter to get an optimum ZnO nanowires and nanotips density.(*58*) Also, we need to control the morphology of the ZnO nanostructures. Generally speaking, at a low growth temperature and long growth time, nanowires were formed, while at a relatively high growth temperature and short growth time, nanotips were grown.(*58*)

For the ultrasonic wave driven nanogenerator, there were thousands to millions of nanowires that contribute to the electric output in a random phase. Although each nanowire is considered to be in a unequilibrium state, but the statistical average of

thousands of them can be considered as in a dynamic steady state with continuous constant output, which is similar with the process in solar cells.

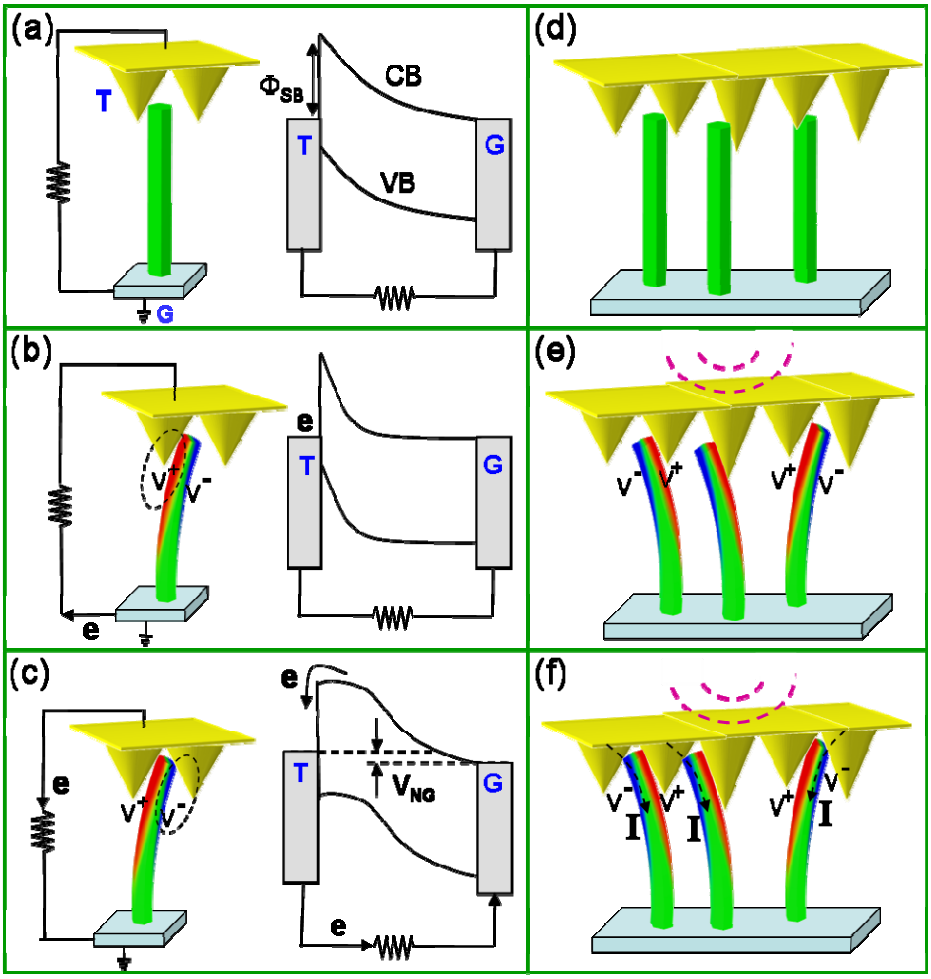

Figure 29. Physical principle of a single layered nanogenerator. (a) Schematic diagram of the nanogenerator and the corresponding electron energy band diagram, where "T" is the Au-nanotip, and "G" is the grounded nanowire. (b) Under the excitation of ultrasonic wave, there is a relative movement (in both vertical and lateral directions) between the nanotip and the nanowire, and as a result the nanowire is bent with the contact surface being stretched. The corresponding local piezoelectric potential (positive) creates a reversely biased Schottky barrier. (c) When the relative movement of the nanotip and nanowire is strong enough, the nanowire is bent enough to touch another adjacent nanotip with its compressive side. Then, the local piezoelectric potential (negative) sets the Schottky barrier to be forward biased and drives the flow of electrons from the nanowire into the nanotip. (d) Schematic diagram of multiple nanowire and nanotip contacts with slight variation in heights and lateral distribution. (e) Disregard the nanowires being deflected to left-hand or right-hand, the first contacting surfaces with the tips are tensile surfaces with a positive piezoelectric potential. (f) Electric currents created by the driving force of the piezoelectric potential when the compressive surfaces of the nanowires contacting the surfaces of adjacent tips. The contacts can be simultaneous or with a slight delay, but the created transient currents flow in the same direction.

This can also be interpreted using the energy band diagram. The energy conversion process can be understood from the change in band structure induced by the piezoelectric potential. Since Au has a work function of 4.8 eV, which is larger than the electron affinity of ZnO (4.5 eV), a Schottky contact (barrier height of Φ_{SB}) at the interface is formed (Figure 29(a)). When a nanotip slowly pushes a nanowire, a strain field is created across the nanowire width, with its outer surface in tensile and its inner surface in compressive strain. This asymmetric strain produces an asymmetric piezoelectric potential across its width, with V^- (negative) at the compressive surface and V^+ (positive) at the stretched surface.(*134, 138*) It is important to note that the piezoelectric potential is created by the ions in the crystal when the nanowire is subject to mechanical deformation, which cannot move freely; they may be partially screened by free carriers in the nanowire but cannot be completely neutralized or depleted.(*139*) This means that the piezoelectric potential still preserves even with consideration of the existence of moderate free charge carriers in ZnO nanowire. When a nanotip is in contact with the stretched surface of the nanowire, which has a higher local potential than the nanotip, a reversely biased Schottky barrier blocks the flow of electrons through the interface (Figure 29(b)). As the degree of nanowires' bending increases, its compressive side may reach the surface of an adjacent nanotip, thus, the local piezoelectric potential V^- (negative) in the nanowire results in a local shape modification of the conduction band of the nanowire near the nanotip (Figure 29(c)). If the raise in local potential energy is large enough as determined by the degree of nanowire bending,(*138*) the accumulated local n-type carriers in the nanowire can quickly flow through the contact into the nanotip, which creates a circular flow of the electrons in the external circuit, e.g., the output current. The role played by the Schottky barrier is to prevent the flow of electrons from the nanotip into the nanowire, which is a key structure for preserving the piezoelectric potential and releasing the free electrons from the nanowire into the nanotip. A working nanogenerator is required to have such a diode effect, and it was first

measured for each and every nanogenerator to determine its correct polarity. The role played by the piezoelectric potential is to drive the electrons from the ZnO nanowire to overcome the threshold energy at the Au-ZnO interface and flow into the Au nanotip. The piezoelectric potential does not directly determine the magnitude of the output voltage. As more electrons are pumped into the Au nanotip, the local Fermi surface is raised by the accumulated charge. Therefore, the theoretical output voltage is determined by nothing but the difference between the Fermi energies of the Au-nanotip on the top and the ZnO-nanowire at the bottom, as illustrate by V_{NG} in Figure 29(c). In practice, one has to consider the contact resistance, system capacitance and possible current leakage, all of which would lower the voltage output to be measured.(*140*)

As the nanogenerators was subjected to ultrasonic wave excitation in a water bath, the ultrasonic wave would cause a vertical or lateral vibration of the Si wafers and/or vibration of the ZnO nanowires, resulting in a relative bending/deflection of the nanowires as enforced by the Au coated nanotips (Figure 29(e)). The nanotips were significantly thicker and stiffer than the nanowires (Figure 28(g) and (h)). Regardless the nanowires being deflected to left-hand or right-hand, the currents generated by all of them add up constructively as determined by the Schottky barrier and the uniaxial growth of the nanowires (Figures 29(e) and (f)), although the output voltage is determined by the performance of individual nanowire. A constant and steady direct output current is observed as long as the ultrasonic wave is on.

The layer-by-layer integrated nanogenerators show enhanced output current and voltage. By connecting two individual layers of nanogenerators in parallel, e.g., connecting electrodes 1 with 3 and electrodes 2 with 4 in Figure 28(e), the output current was a sum of the two nanogenerators. As shown in Figure 30(a), a single layer of nanogenerator L1 gave ~13 nA of short circuit output current, and the other layer of nanogenerator L2 gave ~10 nA under the same conditions. After connecting them in parallel, the output current increased to an average of 22 nA (Figure 30(a), red curve).

The working principles could be further verified by reversely connecting those two layers of nanogenerators in anti-parallel in reference to the polarities of their Schottky barriers,(*141*) e.g., connecting electrodes 1 with 4 and electrodes 2 with 3 in Figure 28(e). The total output current was just 3 nA (Figure 30(a), purple curve), which was the difference of their individual output currents.(*142*) As shown in Figure 30(a), the output signal for the L1+L2 case is a lot "unstable" than the L1-L2 case. This is due to the fact that the L1+L2 case double amplifies the instability introduced by the intensity and frequency of the ultrasonic wave source, while the L1-L2 case impairs the instability.

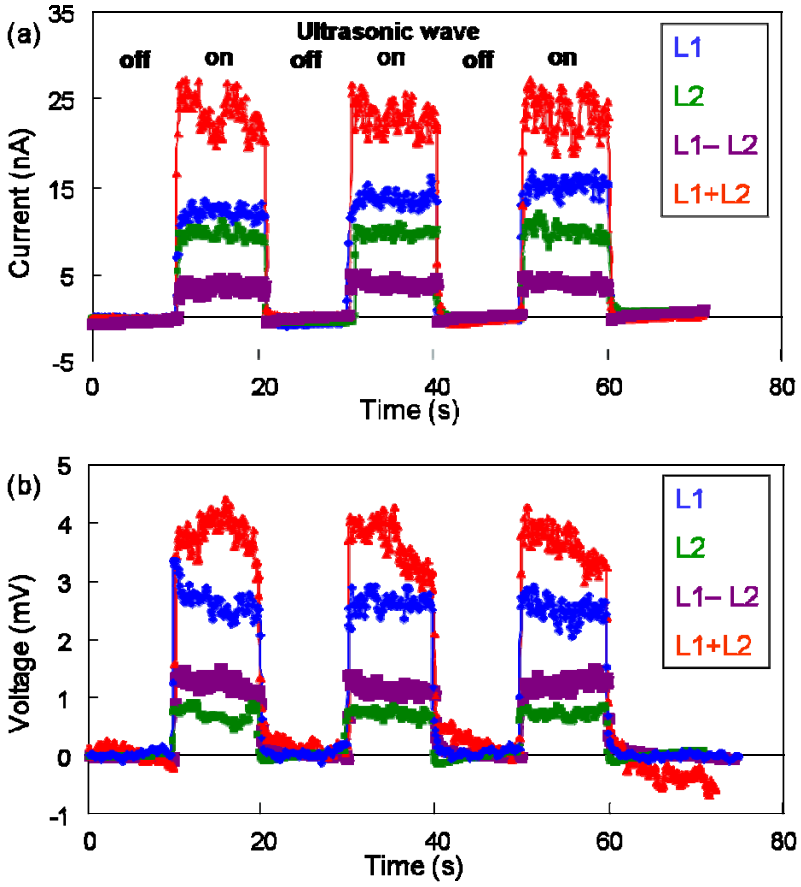

Figure 30. Output current and voltage signals by connecting two single-layered nanogenerators in parallel and anti-parallel, and series and anti-series, illustrating the three dimensional integration of the nanogenerators for raising output power. (a) Short circuit current output measured from the nanogenerators when connected in parallel and anti-parallel. (b) Open circuit voltage output measured from the nanogenerators when connected in series and anti-series. The regions when the ultrasonic wave was on and off are indicated. The surface area of each nanogenerator was 6 mm^2.

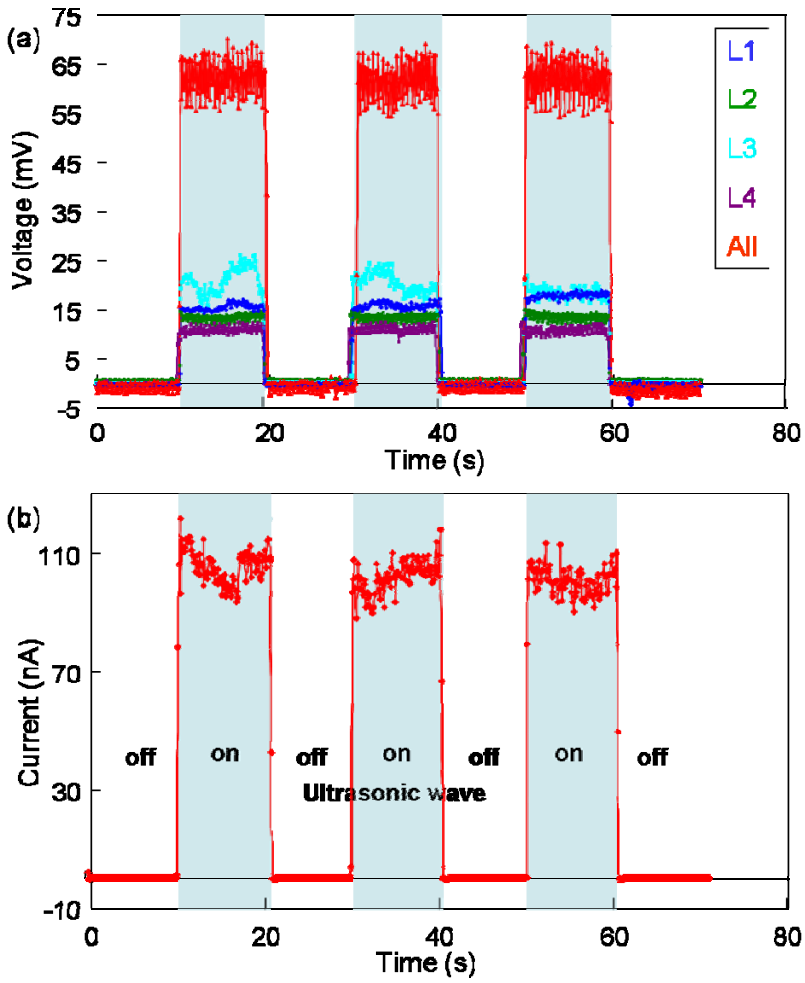

Figure 31. Open circuit voltage and short circuit current output measured from four-layer integrated nanogenerator. (a) Open circuit voltage output measured from each individual layers and the four-layer integrated nanogenerator. (b) Short circuit current output measured from the four-layer integrated nanogenerator. The regions when the ultrasonic wave was on and off are indicated. The surface area of the nanogenerator was 6 mm^2.

In a similar way, by connecting two layers of nanogenerators in a series, e.g., connecting electrodes 2 with 3 in Figure 28(e), the output voltage was the sum of the output voltages from the two individual layers. As presented in Figure 30(b), L1 gave an output voltage of approximate 2.6 mV, while L2 gave about 0.8 mV. When those two layers of nanogenerators were connected in series and tested under the same condition, the output voltage was around 3.5 mV on average (Figure 30(b), red curve), which was the sum of their individual outputs. Furthermore, if we put the two layers in anti-series,

e.g., connecting electrodes 2 with 4 in Figure 28(e), the output voltage was just 1.5 mV (Figure 30(b), purple curve), which was the difference of their individual output voltages.

Integration of multilayers of nanogenerators has great potential for raising the output voltage. Once the output voltage is high enough to operate an electronic device, such as a diode, the outputting electric energy from the nanogenerators can be stored for future use. To demonstrate the technological feasibility of the approach, we have connected several nanogenerators in series. As shown in Figure 31(a), four individual layers of nanogenerators, L3, L4, L5 and L6 with 11 mV, 14 mV, 16 mV and 20 mV open circuit output voltages, respectively, were connected in series. The resultant total output voltage was ~62 mV as expected. The corresponding short circuit output current was around 105 nA (Figure 31(b)). Each of the layers shows typical Schottky characteristics. It appears that the ultrasonic wave of 41 kHz can penetrate rather deep so that the damping effect is not a major problem. The maximum power output of the four-layer integrated nanogenerator is 6.5 nW for a surface area of 6 mm^2. A power density of 0.11 $\mu W/cm^2$ was achieved.

4.2 Multilayered three-dimensional alternating current nanogenerator

The harvesting of mechanical energy from ambient sources could power electrical devices without the need for batteries. However, although the efficiency and durability of harvesting materials such as piezoelectric nanowires have steadily improved, the voltage and power produced by a single nanowire are insufficient for real devices. The integration of large numbers of nanowire energy harvesters into a single power source is therefore necessary, requiring alignment of the nanowires as well as synchronization of their charging and discharging processes.

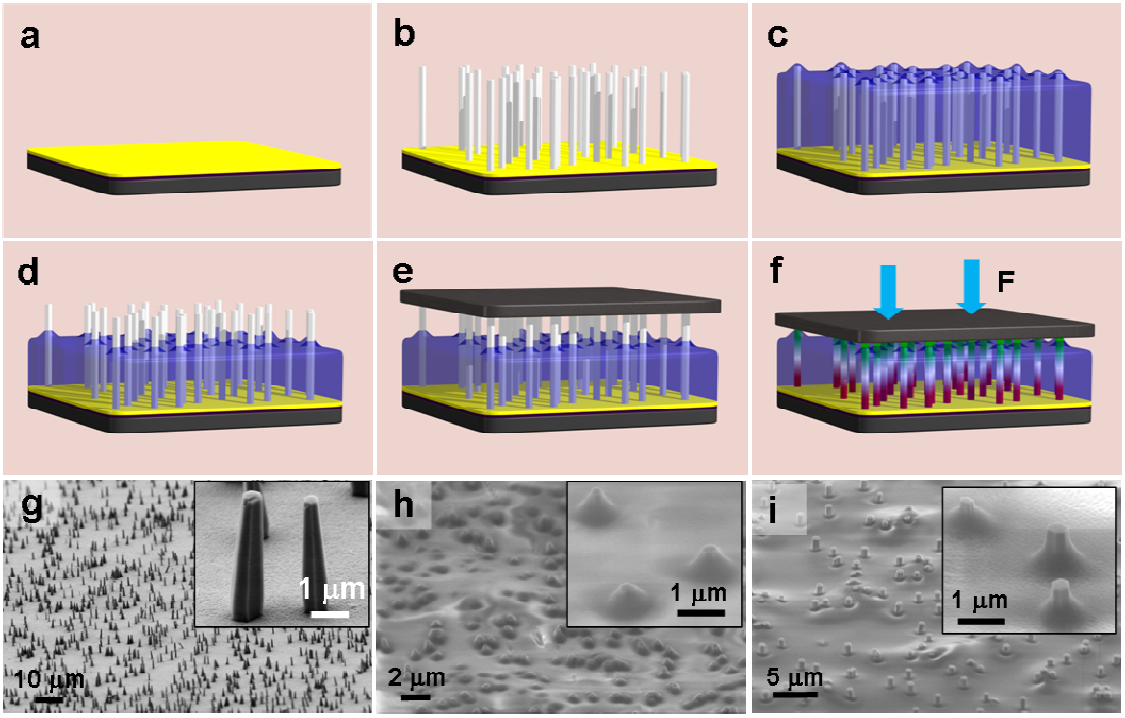

Figure 32. On a gold-coated silicon wafer (a), ZnO nanowire arrays (b) are grown by low-temperature hydrothermal method. PMMA, applied by spin coating (c), covers both the bottom and tips of the nanowire arrays. After oxygen plasma etching (d), the tips of the nanowires are exposed, but the main body and bottoms of the nanowires are still fully enclosed. A platinum-coated flat electrode is placed on top of the nanowires (e) to form a firm Schottky contact. When a uniaxial stress is applied at the top electrode (f), the nanowires are readily compressed, the straining of the crystallographically aligned nanowires generating a macroscopic piezoelectric potential along the c-axis growing direction of the nanowires. g–i, SEM images of the as-grown ZnO nanowire arrays on the substrate (g), after spin-coating with PMMA (h) and after oxygen plasma etching (i).

We present an innovative approach for using vertically (Figure 32 (a)-(i)) aligned ZnO nanowire arrays for converting mechanical energy into electricity using materials that are environmentally friendly and biocompatible. The vertical nanowires are in full contacts at the two ends. Utilizing the crystallographic alignment of the nanowires, a macroscopic piezo-potential is created when the nanowires are subjected to a uniaxial compressive or tensile strain, which drives a transient flow of electrons in the external circuit.

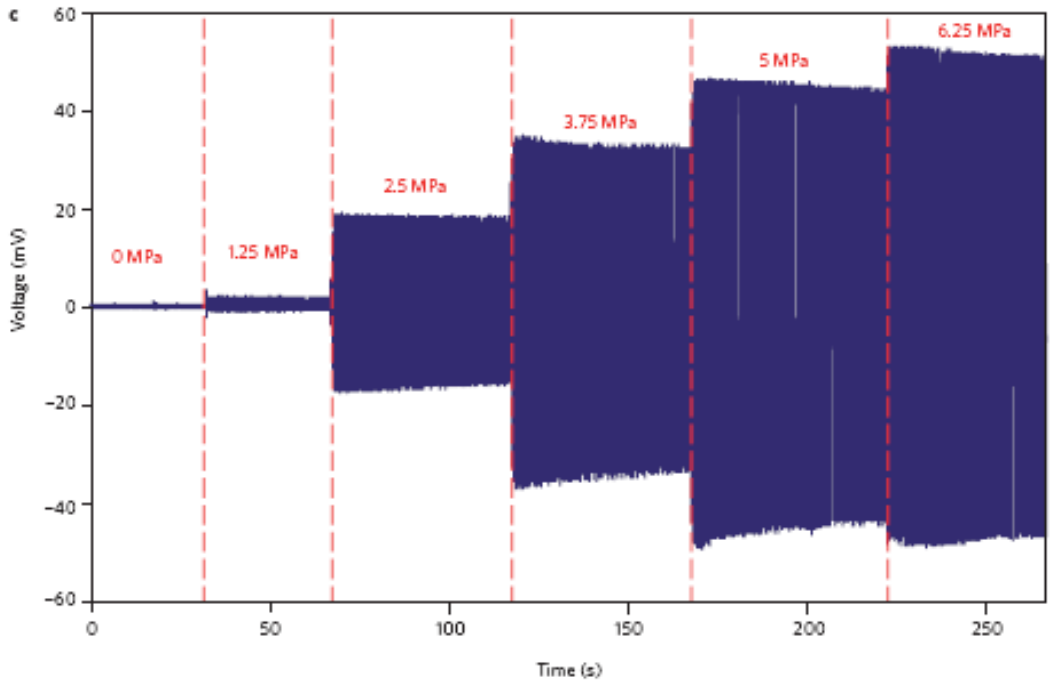

Figure 33. Magnitude of the output voltage as a function of the magnitude of the compressive stress at a frequency of 2 Hz. The vertically integrated nanogenerator is built using ZnO nanowires of about 300 nm in tip diameter and 4 μm in length. The size of the vertically integrated nanogenerator was ~4 mm^2. The total number of nanowires grown in the nanogenerator was ~75,000 (area density $1.9x10^6/cm^2$). As the applied stress is gradually increased from 0 MPa, 1.25 MPa, 2.5 MPa, 3.75 MPa, 5 MPa, and then to 6.25 MPa, the output voltage increases almost linearly. The impact speed of the mechanical trigger was 0.1 m/s, but it was hard to correlate this to the straining rate in the nanowires because the damping effect of the packaging material around the nanogenerator was difficult to be quantified.

Theoretical calculations have shown that, within elastic linear mechanics regime, the output voltage of a single nanowire is linearly proportional to the magnitude of its deformation.(*138*) The ZnO nanowires in the vertically integrated nanogenerator were all connected in parallel between the two electrodes. Undoubtedly, as we raise the pressing force onto the nanowires, the deformation of the nanowires becomes larger, and the output voltage linearly scales up (Figure 33). It must be noticed that a large fraction of the applied stress was consumed at overcoming the elasticity of the packaging material (1-2 mm in thickness) around the vertically integrated nanogenerator. The magnitude of the output voltage also depended on the straining rate at which the stress was applied.

The output signals of the vertically integrated nanogenerator were stable over a long period of time.

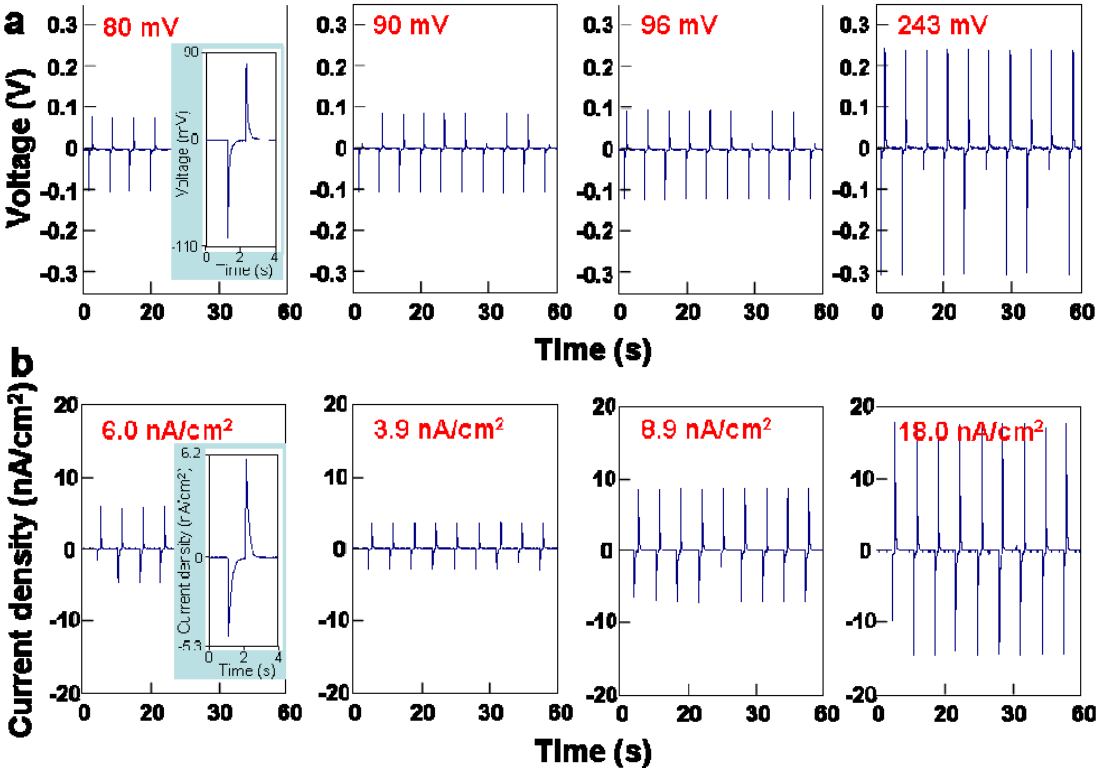

Figure 34. Enhancing the output voltage of the vertical nanowire array nanogenerators by integrating them in series. (a) Individual devices produce output voltages of 80, 90 and 96 mV, respectively. When the three nanogenerators are connected in series, the voltage increases to 243 mV. (b) Linear superposition of output current when the nanogenerators are connected in parallel. Individual devices produce output current densities of 6.0, 3.9 and 8.9 nA cm^{-2}, respectively. When the three nanogenerators are connected in parallel, the output current density increases to 18.0 nA cm^{-2}.Insets in the left panels of (a) and (b) are enlarged views of a single pulse.

We have integrated three vertical nanowire array nanogenerators in series to receive an enhanced output voltage of 0.243 V (Figure 34(a)) and in parallel to get an improved output current density of 18 nA/cm^2 (Figure 34(b)). A peak output power density of 2.7 mW/cm^3 has been achieved. This demonstrates a great potential for layer-by-layer three-dimensional integration for applications where a dynamic compressive stress/straining is available, such as in shoe pads, automobile tires and underneath of carpet/floor.

4.3 Self-powered nanowire devices

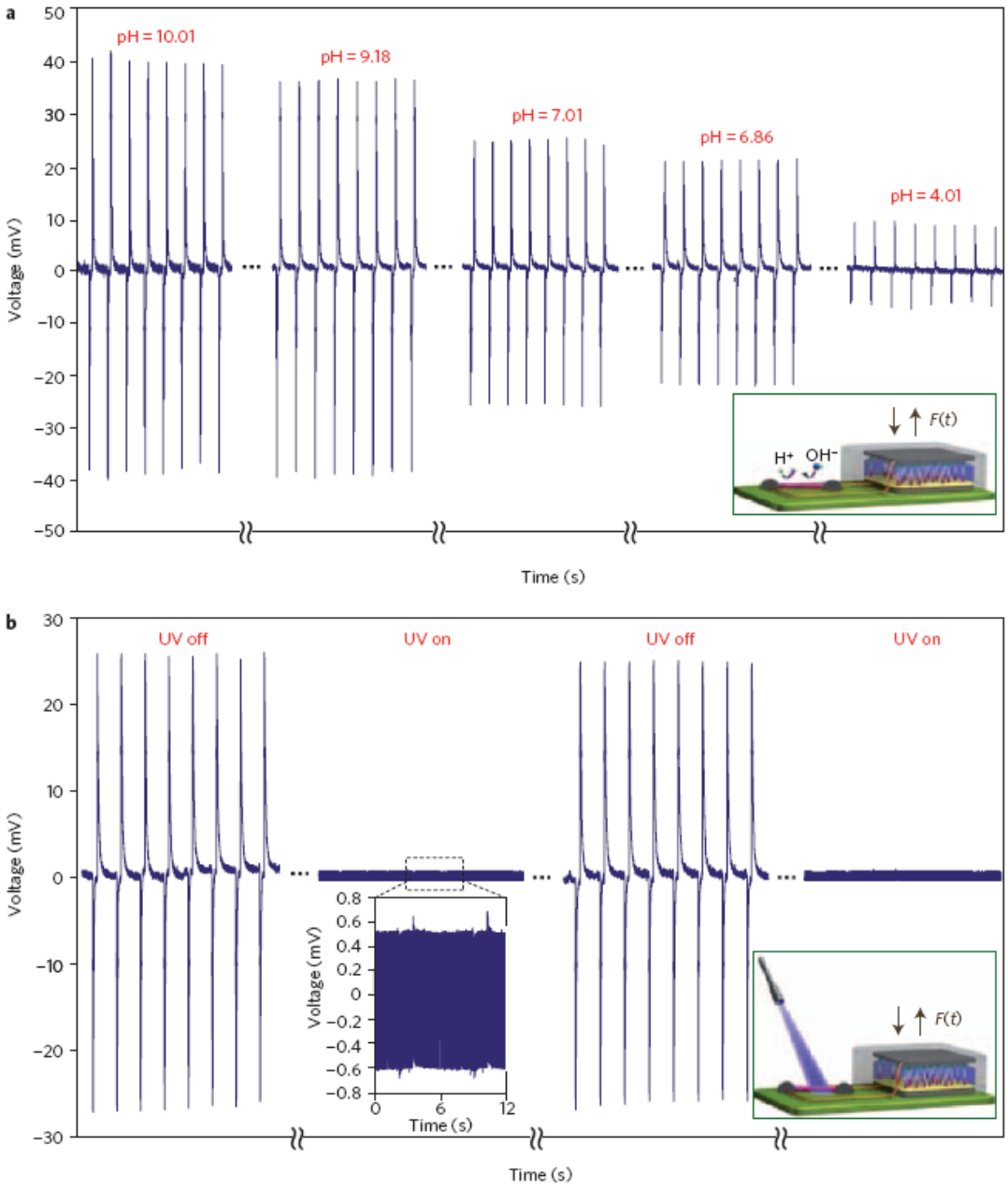

Figure 35. (a) Voltage drop across a single ZnO nanowire-based pH sensor powered by a vertical nanogenerator with an output voltage of 40 mV, showing a stepwise dropping of the voltage across the nanosensor as a function of its local pH value. The ZnO nanowire was covered with a thin layer of Si_3N_4 and the testing was carried out within 1 hr so that the etching effect from the solution was negligible. (b) Voltage drop across a ZnO nanowire based UV sensor powered by a vertically integrated nanogenerator with an output voltage of ~25 mV. When the UV light is off, the resistance of the nanowire is comparable to the inner resistance of the vertically integrated nanogenerator, and the nanowire therefore shares a substantial amount of voltage. When the UV light is turned on, the resistance of the nanowire decreases to a level that is non-competitive to the vertically integrated nanogenerator, and the voltage drop across the nanowire is very small. The insets are schematics of the nanowire-based nanopower–nanodevice systems.

Building self-powered nanosystems is a future direction of nanotechnology. A nanosystem is an integration of nanodevices, functional components, and a power source. The vertical nanowire array nanogenerator was integrated with a single nanowire based nanosensor to demonstrate a "self-powered" nanosystem that was made of a vertical nanowire array nanogenerator and a nanosensor, the two of which were separated components and were connected in series to form a loop.

As shown in an inset in Figure 35, a vertical nanowire array nanogenerator was connected to a ZnO nanowire based pH sensor, and the voltage across the nanosensor was monitored by a voltmeter (*143*). The pH sensor was coated with a 10 nm Si_3N_4 layer, which was thin enough for the electrostatic interaction between the surface adsorbed charges and the carriers in the nanowire. By powering the pH sensor using a vertical nanowire array nanogenerator that generated an output voltage of ~ 40 mV, a clear sensitivity to local pH change was observed (Figure 35(a)). When the buffer solution was basic, the surface of the nanosensor was dominated by $-O^-$ groups. Those negatively charged groups resulted in depletion regions at the surface of the n-type ZnO nanowire, which increased the resistance of the ZnO nanowire. Thus, the voltage drop on the ZnO nanowire was relatively high. As the buffer solution was changed from basic to acidic, the surface of the nanosensor was gradually changed from $-O^-$ to $-OH_2^+$ groups. Therefore, the depletion regions at the ZnO nanowire surface diminished, which would lower the resistance of the ZnO nanowire. As we changed the pH value of the testing buffer solution from 10.01, 9.18, 7.01, 6.86, then to 4.01, the voltage drop on the pH sensor changed accordingly (Figure 35(a)).

A vertically integrated nanogenerator was also applied to drive the operation of a ZnO nanowire based UV sensor (Figure 35(b)). When UV light was off, the resistance of the UV sensor was ~10 MΩ, which was of the same order as the vertically integrated nanogenerator's inner resistance. The corresponding voltage drop on the nanosensor was about 25 mV, as shown in Figure 35(b). When the nanosensor was illuminated by UV

light, its resistance dropped to ~500 KΩ, which is 20 times lower in magnitude than that before illumination. And then the voltage drop on the nanosensor could hardly be distinguished from the noise.

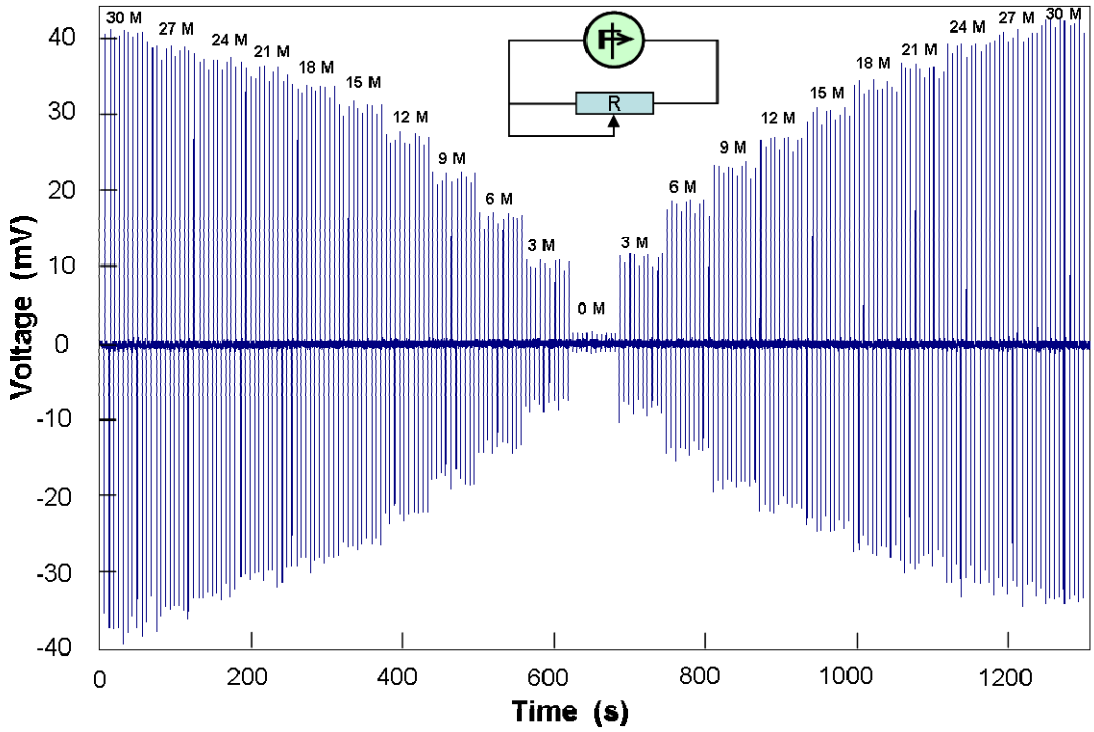

Figure 36. When gradually changing the amount of loading resistance (from 0 to 30 MΩ), the magnitude of the voltage drop across the resistor changes accordingly. The voltage on the resistor is $V = V_0R/(R+r)$, where V_0 is the open circuit voltage of the vertically integrated nanogenerator, r is its inner resistance, and R is the resistance of the resistor.

This unambiguously indicates that the vertical nanowire array nanogenerator of 20-40 mV can power up a nanosensor! By using a variable resistor, the voltage across the resistor was sensitive to the magnitude of its resistance and the result fits well to the linear circuit theory (Figure 36). The powering of a nanosensor is a pivot step toward building up self-powered, solely nanowire-base nanosystems.

CHAPTER 5

HIGH PERFORMANCE ALTERNATING CURRENT NANOGENERATORS BASED ON EPITAXIALLY GROWN $PBZR_XTI_{1-X}O_3$ NANOWIRE ARRAYS

Lead zirconate titanate, PZT, is probably the most important piezoelectric material for sensors and actuators owing to its remarkable piezoelectric performance.(*144-145*) However, the fabrication of PZT thin films(*146*) and microfibers(*147*) usually requires high temperatures (~ 650 ℃) to increase the crystallinity,(*148*) which leads not only to high cost and incompatibility with general fabrication processes, but also makes it difficult to integrate with soft materials, even though a transfer technique has been demonstrated recently.(*149*) We reported the first epitaxial growth of vertically aligned single crystal $PbZr_{0.52}Ti_{0.48}O_3$ nanowire arrays on a variety of conductive and nonconductive substrates by hydrothermal decomposition at 230 ℃.

5.1 Epitaxial growth of PZT nanowire arrays by hydrothermal decomposition

PZT nanowire arrays were grown by a hydrothermal process.(*150*) Conductive substrates, 0.7 wt% Nb doped $SrTiO_3$ (STO) (100) and 0.01 wt% Fe doped STO (100) (~0.007 Ω·cm), were chosen for the epitaxial growth due to their small lattice mismatch with PZT (Figure 37(a)). The growth solution (50 ml) was prepared by mixing 0.8168 g $(C_4H_9O)_4Ti$ dissolved in 26 ml ethanol, and 0.8379 g $ZrOCl_2 \cdot 8H_2O$ dissolved in 30 ml de-ionized water.(*151-152*) Then the Ti^{4+} ethanol solution was added drop by drop into the Zr^{4+} aqueous solution under vigorous stirring. The mixed solution was introduced into 150 ml 0.25*M* $NH_3 \cdot H_2O$, resulting in a white precipitation of $Zr_{0.52}Ti_{0.48}O(OH)_2$ (ZTOH).

After filtering and rinsing to get rid of the residual Cl^-, $NH_3 \cdot H_2O$, C_4H_9OH, and C_2H_5OH, the white precipitate ZTOH was redispersed in DI water. Under vigorous stirring, 1.656 g $Pb(NO_3)_2$, 5.611 g KOH, 0.02 g poly(vinyl alcohol), and 0.36 g poly(acrylic acid) were consecutively added. Next, the hydrothermal solution was placed inside a stainless steel autoclave with a Teflon liner and with the substrate leaning against the side wall. It was then placed in an oven at 230 °C for 12 h. The final product was baked at 60 ℃ for 2 h.

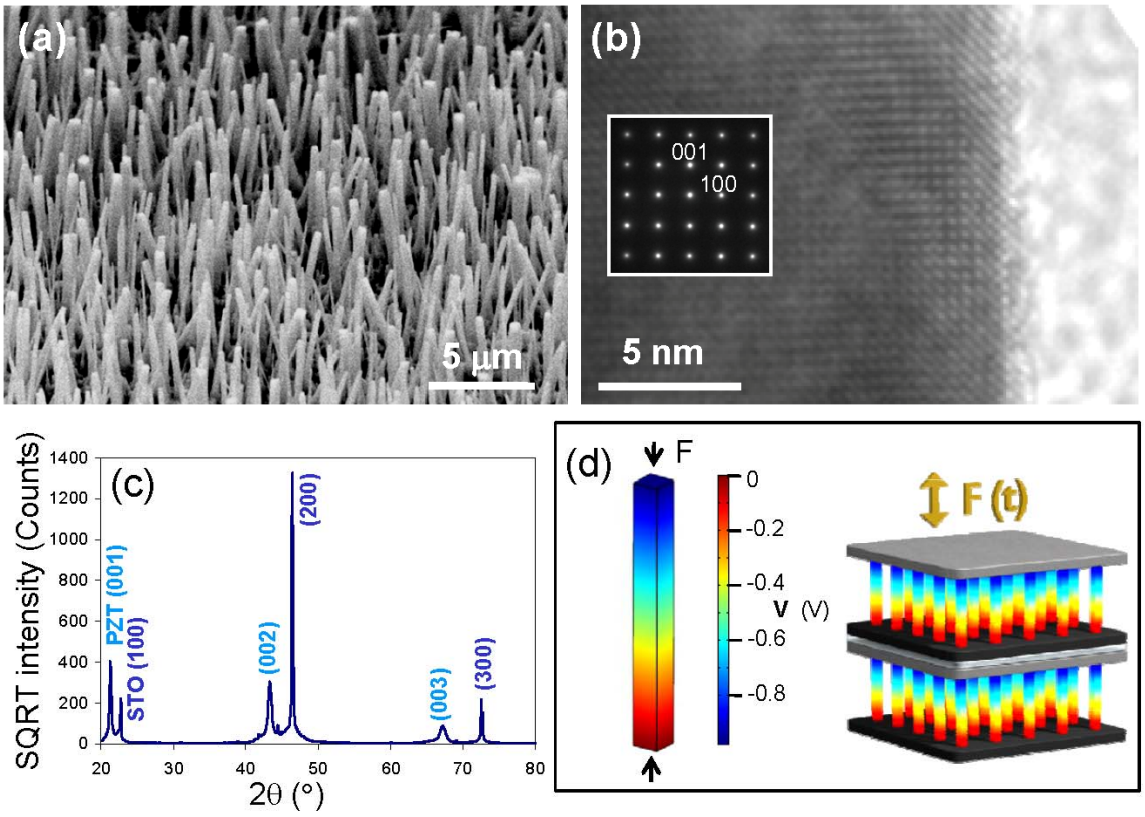

Figure 37. (a) SEM image of the epitaxially grown $PbZr_{0.52}Ti_{0.48}O_3$ nanowire arrays on a Nb doped $SrTiO_3$ (STO) substrate by hydrothermal decomposition. (b) HRTEM image and electron diffraction pattern (inset) acquired from an as-grown PZT nanowire, indicating a well crystallized tetragonal phase with a lattice constant of a = 3.93 Å and c = 4.16 Å. (c) Conventional θ-2θ scan XRD spectrum from the as-grown nanowire arrays. (d) Finite element calculation (left) of the piezoelectric potential distribution (~ 1 V) in a PZT nanowire ($d_{33} = 1.52 \times 10^{-10}$ C/N) of 500 nm in width and 5 μm in length, under a uniaxial compression of 2.5 μN. The right-hand side schematic diagram is the structure of a multilayered nanogenerator fabricated using the nanowire arrays.

The reaction equations are proposed in the following. During the nucleation and growth of $PbZr_{0.52}Ti_{0.48}O_3$ nanowires, the poly(vinyl alcohol) and poly(acrylic acid) perform as capping agents that chemisorb at the side surfaces of the nanowires and thus inhibit their radial growth. TEM analysis of a single nanowire (Figure 37(b) and Figure 38) and XRD of nanowire arrays (Figure 37(c)) show that the as-synthesized nanowires have a tetragonal phase of single crystalline $PbZr_{0.52}Ti_{0.48}O_3$ (space group P4mm) and a [001] growth direction.(*153*) The vertical growth and alignment were enforced by the epitaxial growth on the inorganic substrate. A piezoelectric domain boundary was found in the axial direction of the nanowire, but the entire nanowire preserves a single crystal structure (Figure 38(c)).

$$NH_3 \cdot H_2O \leftrightarrow NH_4^+ + OH^- \quad (6)$$

$$ZrOCl_2 \cdot 8H_2O + 2\ OH^- \leftrightarrow ZrO(OH)_2 + 2\ Cl^- + 8\ H_2O \quad (7)$$

$$Ti(C_4H_9O)_4 + 4\ H_2O \leftrightarrow Ti(OH)_4 + 4\ C_4H_9OH \quad (8)$$

$$13\ ZrO(OH)_2 + 12\ Ti(OH)_4 \rightarrow 25\ Zr_{0.52}Ti_{0.48}O(OH)_2 \downarrow + 12\ H_2O \quad (9)$$

$$Pb(NO_3)_2 + 2\ OH^- \leftrightarrow Pb(OH)_2 + 2\ NO_3^- \quad (10)$$

$$Pb(OH)_2 + Zr_{0.52}Ti_{0.48}O(OH)_2 \rightarrow PbZr_{0.52}Ti_{0.48}O_3 \downarrow + 2\ H_2O \quad (11)$$

5.2 High power output alternating nanogenerator based on PZT nanowire arrays

Currently, a common bottleneck with nanogenerators is that the output voltage and output power are still too small to realize any practical applications. Before being able to make any practical applications out of these nanogenerators, we need first to boost up their output voltage/power. And there are several different approaches going on aiming at resolving this issue, including utilizing large areas of patterned ZnO nanowire arrays, doing multi-layer and multi-row integration of the vertical and horizontal ZnO nanowire arrays, etc.

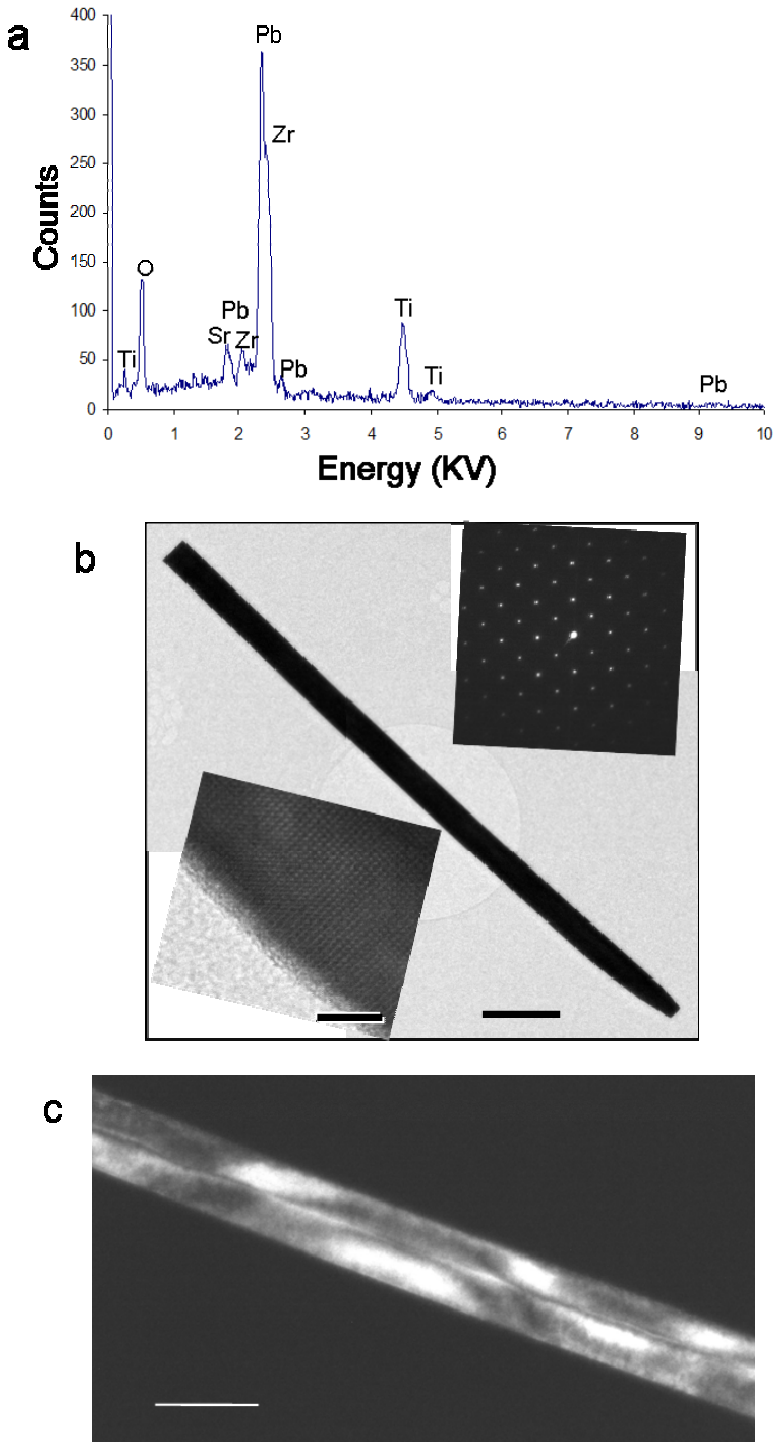

Figure 38. Characterization of the as grown PZT nanowires. (a) Energy dispersive X-ray spectrum acquired from a single crystal $PbZr_{0.52}Ti_{0.48}O_3$ nanowire in SEM showing its chemical composition. (b) Low magnification TEM image. Scale bar, 500 nm. Upper right is the electron diffraction pattern. Lower left is a corresponding HRTEM image recorded from a PZT nanowire. Scale bar, 4 nm. (c) A dark field image from a PZT nanowire showing the presence of a piezodomain boundary along the length of the nanowire. Scale bar, 200 nm.

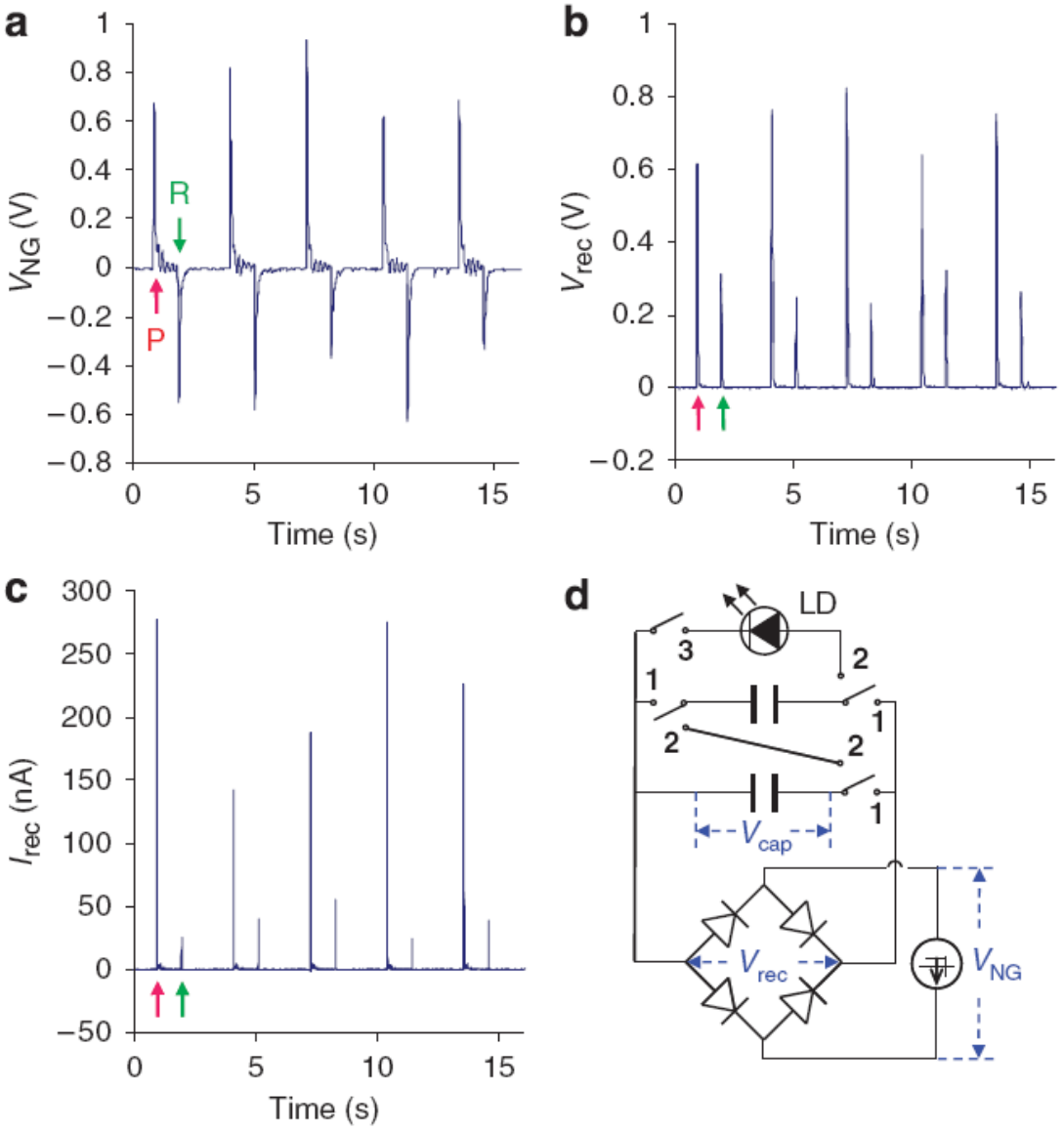

Figure 39. (a) Open circuit voltage of a seven-layer integrated nanogenerator before rectification, and (b) open circuit voltage and (c) short circuit current of the nanogenerator after rectification, where the outputs when the nanogenerator was compressed and released are indicated with red and green arrowheads, respectively. The projected surface area of the nanogenerator was 6 mm2. (d) Schematic design diagram of the rectifying circuit and charge storage devices, in which the measured voltages are labeled.

As we may know, ZnO is weakly n-type conductive in nature which comes from the oxygen vacancies and zinc interstitial atoms. Even though the weak conductivity may not screen completely the piezoelectric potential, the piezoelectric potential is decreased to a certain degree, which eventually brings down the output voltage and thus output power of the nanogenerators.(*139*) In order to get around this problem, here we

demonstrate to use PZT rather than ZnO to boost the output voltage/power of the nanogenerators.(*144, 149, 154*) In addition, PZT has a higher piezoelectric coefficient than ZnO, which is more favorable to fabricating nanogenerators than ZnO.

Finite element calculation is used based on a cantilever model that has one end fixed and the other end free. We have three main assumptions. First, the elastic modulus of the nanowire is isotropic and the piezoelectric efficient is anisotropic. Second, the nanowire is under pure axial compression and free of shear strain. And third, the piezoelectric domains are all perfectly aligned up. The calculation result shows that, for a tetragonal PZT nanowire growing along [001] direction with a 500 nm diameter and 5 μm length, a uniaxial force of 2.5 μN can create a piezoelectric potential (piezo-potential) of ~ 1 V (Figure 37(d)).

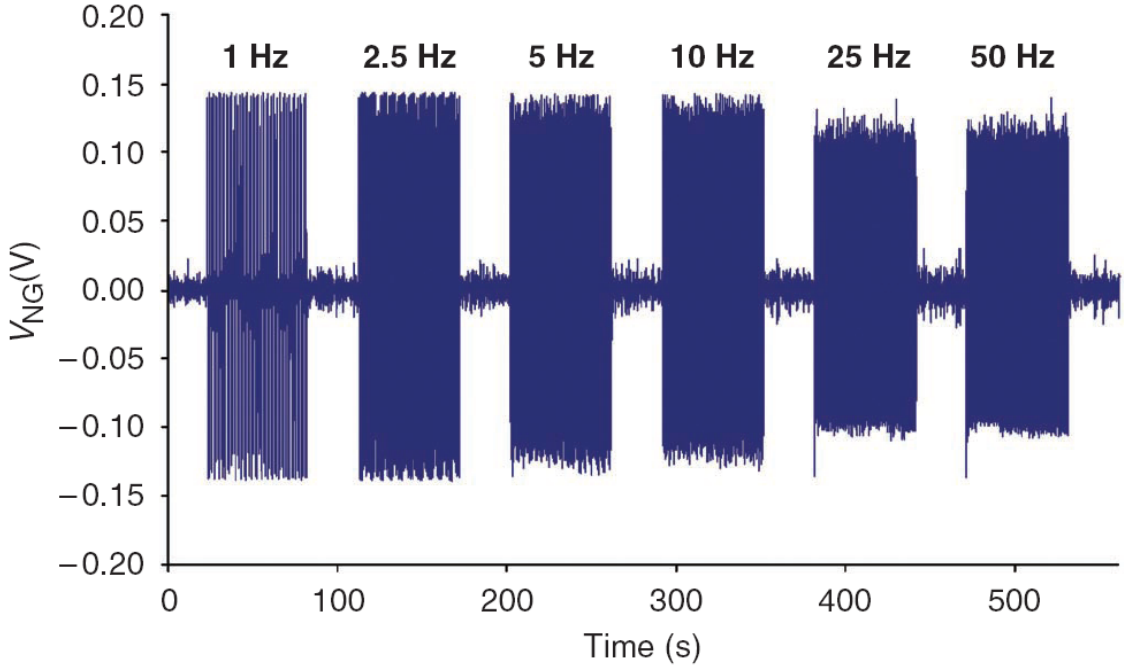

Figure 40. Output voltage of a nanogenerator as a function of the driving frequency. When the external force frequency is at relatively high, the soft packaging epoxy polymer could not respond at the same pace as the external mechanical force, which dampers the magnitude of the external force. Therefore, the amplitude of the output voltage is slightly reduced when the force frequency is increased. Such performance is expected to be improved with the exploration of new packaging materials and technologies.

To utilize this high piezo-potential, nanogenerators were fabricated using the PZT nanowire arrays grown on conductive Nb-doped STO substrates,(*155*) following the schematic shown in Figure 37(d). A piece of Si wafer was coated consecutively with layers of 50 nm Ti and 300 nm Pt by electron beam evaporation. The Pt side of the Si wafer was placed on top of the nanowire arrays to form an intimate electrical contact. The area of the nanogenerator layer was 6 mm^2. Three-dimensional integration of the nanogenerators was accomplished by stacking multiple layers of the described structure. Each layer was a distinct nanogenerator with each set of two terminals insulated from the other layers and the entire structure was packaged with soft epoxy polymer to ensure the robustness of the device and also isolate possible moisture erosion to the nanowires. The as-fabricated alternating current nanogenerator was measured by the mechanical stimulation triggered by a linear motor that provided a controllable impact speed, force and frequency.

Electrical polarization was required to align the piezoelectric domains in the same direction and in all of the nanowires. In the as-grown nanowires, the dipole moments resulting from the position shift of the Ti^{4+}/Zr^{4+} ions could take six possible orientations along <001>. An electric poling of the nanowires was made by applying an external electric field of 100 KV/cm in a dielectric fluid of high dielectric strength and with the top electrode negative and bottom electrode positive. As a result, a macroscopic piezoelectric polarization was forced to align upward normal to the substrate.(*156*) When the PZT nanowires are subject to a uniaxial compressive force, a piezoelectric field is created inside the nanowires, which produces a transient flow of the free electrons in the external load to screen the piezo-potential. When the force is lifted, the piezo-potential diminishes, and the accumulated electrons are released. A dynamically applied stress drives the electrons in the external circuit to flow back and forth, resulting in an alternating output. The dynamic strain applied to the nanogenerator in our study was stimulated using a linear motor, which provided a controllable impact speed, force and

frequency. Shown in Figure 39(a) is the output voltage profile from a seven-layer integrated nanogenerator under a periodic mechanical pressing (P) and releasing (R). The output voltage is reduced compared with the calculated result, due to the following reasons. First, the height of the nanowires is non-uniform, and only a few percent of the nanowires are actively generating electricity. Second, the nanowires are not perfectly vertically aligned. So when the nanowires are under compression, shear strain is inevitable. Third is the relatively low remnant polarization after the electric field poling. This could be improved by infiltration of insulating polymers into the spacing of the nanowires, and thus increasing the driving voltage.

The intended use is for harvesting naturally available mechanical agitations rather than a purposely created regular action to drive the nanogenerator. The output voltage of a PZT nanowire based nanogenerator at a range of stimulating frequencies from 1 Hz to 50 Hz is shown in Figure 40. This demonstrates that the nanogenerator is able to work at a range of low frequencies, such as human walking, heart beating and vessel contracting, and its capability of powering *in-vivo* biosensors by harvesting biomechanical and/or biofluid hydraulic energies. In addition the nanogenerators could be configured to work under a relatively high frequency of ~ 50 KHz.(*157*) In such a frequency range, the average output power is about half of the peak output power, and thus, an average power density of 2.8 mW/cm^3 is conceivable by increasing the agitation frequency shown in Figure 39.

5.3 Powering up microelectronic devices

The piezoelectric nanogenerator that converts mechanical energy into electricity was first demonstrated using ZnO nanowire arrays.(*32*) Following this initial discovery, both direct current(*33, 158-159*) and alternating current(*34, 160*) ZnO nanogenerators have been developed. In addition, nanogenerators based on GaN nanowires(*161*) and poly(vinylidene fluoride) nanofibers(*162*) have shown promising potential for enhancing

the nanogenerator performance. Consequently, a world wide effort has been launched in this regard, forming a new research field in nanotechnology and energy science.(*163*)

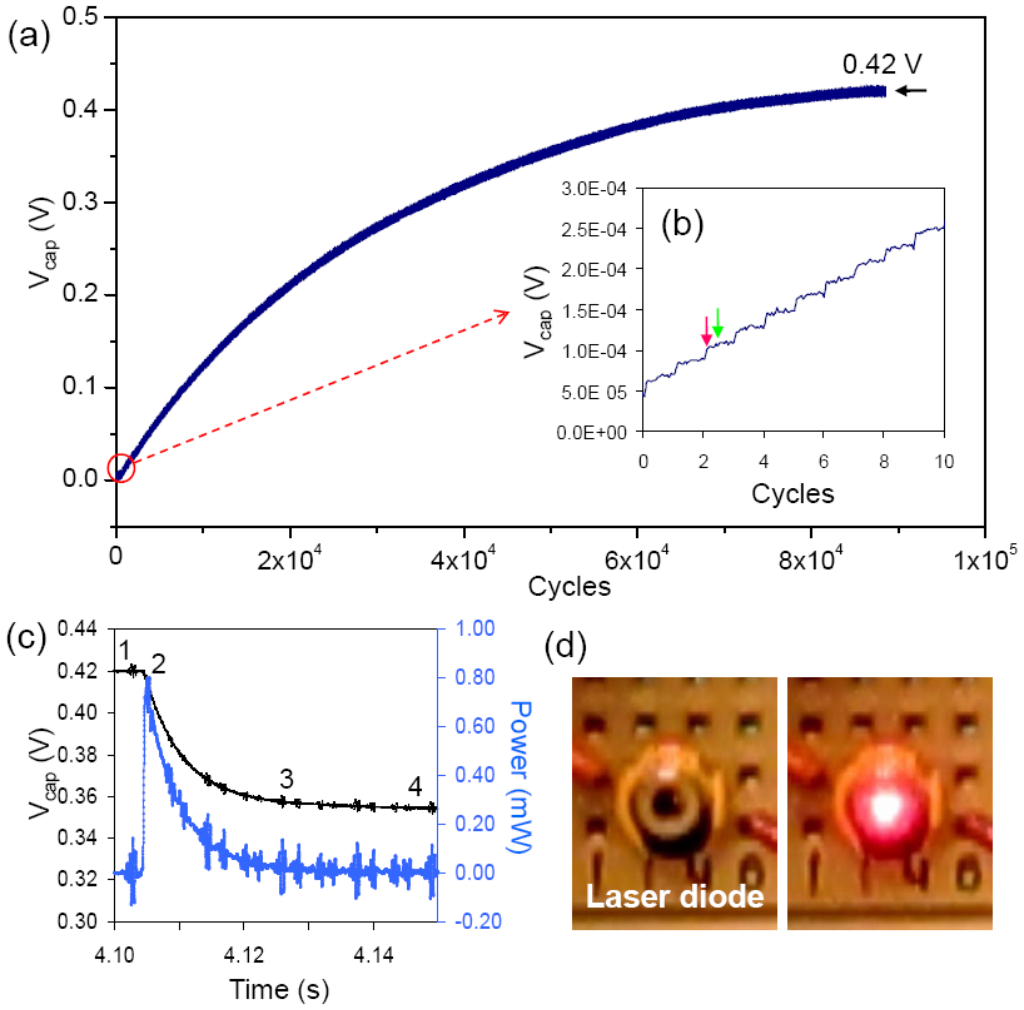

Figure 41. (a) Voltage across a storage capacitor when being charged by an alternating current nanogenerator with 0.7 V peak voltage. (b) An enlarged plot of the voltage curve in (a) at the very beginning of the charging process as indicated by a red circle. The step increases in capacitor voltage when the nanogenerator is compressed and released are indicated by red and green arrowheads, respectively. (c) Discharging voltage curve across a single capacitor when it was connected in series together with seven other capacitors to a LD (emission wavelength 650 nm, operation power 0.1-6 mW), and the corresponding output power to drive the LD (blue curve). V_{cap} saturates at 0.42 V (1~2). Then the capacitors discharged to light the LD, and the V_{cap} drops to 0.35 V (2~3) followed by a slow decay process (3~4). It is suggested that such a discharge behavior took place when the charges stored in the capacitor were insufficient to light the LD although the remaining voltage was enough to overcome the LD threshold but the current was limited. The output power was derived from the discharge curve following $nCV_{cap}dV_{cap}/dt$, with n = number of capacitors in series. The fluctuation in power curve is due to differentiations of the noise in the V_{cap} curve. (d) Snap shots of the LD before and at the moment of being lit up using the stored charges. Video is provided in Supplementary information.

The advantage of using nanowires for energy harvesting is their high mechanical robustness and responsiveness to tiny random mechanical disturbances/stimulation. Although the output voltage of nanogenerators has been raised to 1.2 V using an integration of millions of ZnO nanowires for driving a single nanowire based UV/pH sensor,(*36*) the output power of the nanogenerators was still too small to power any conventional electronic components, such as LDs.

To fully utilize the electrical energy harvested by the nanogenerator in one full cycle of mechanical deformation from both pressing and releasing, a current rectification and energy storage system was implemented using a commercial full-wave bridge rectifier composed of four diodes (Figure 39(d)), each of which had a threshold voltage of 0.3-0.4 V as could be determined from their I-V curves. The voltage and current outputs of the nanogenerator after rectification are shown in Figure 39(b)-(c), respectively, clearly demonstrating full-wave rectification. Next, the generated charge pulses were stored consecutively by connecting eight 22 μF capacitors in parallel, as shown in Figure 39(d) with the switches were set at position "1".

The entire charging process was recorded by monitoring the voltage/potential across a capacitor as presented in Figure 41(a). A step increase in the stored energy can be clearly seen with each cycle of the energy conversion process, as indicated by arrowheads in Figure 41(b). As the charging process continued, the voltage of the capacitor was saturated to ~ 0.42 V, which was lower than the peak output voltage of the nanogenerator and possibly due to voltage drop consumed at the rectifying diodes and/or the leakage of the capacitors, especially when the capacitor voltage was high. Then, by connecting the eight charged capacitors in series by adjusting the switches to position "2", the total output voltage reached $V_{tot} = 0.42 \times 8 = 3.36$ V. This was high enough to drive a LD with a turn-on voltage of ~1.5 V provided the output power was sufficient at the discharge (Figure 41(c)). By utilizing this voltage amplification technique we successfully powered a commercial LD by a fast discharge of the stored charges, as

shown in Figure 41(d). The voltage drop across a capacitor dropped from ~0.42 V to ~0.35 V after the discharge process (Figure 41(c)). This means that ~ 16.7% of the stored charges were effectively used to drive the LD. The remaining charges were still stored in the capacitor and blocked by the threshold operating voltage of the LD. The next round of charging the capacitors would start at a base voltage of 0.35 V rather than 0 V, thus the following charging cycle should take a lot less time.

The projected surface area of the nanogenerator used for generating the charges and powering the LD in Figure 36 was ~ 6 mm^2. The power generated by such a small nanogenerator can not drive the continuous operation of a LD. However, an accumulation of charges generated over a period of time is sufficient to drive the LD for a fraction of a second. This can be of practical use for devices that have standby and active modes, such as glucose sensors and blood pressure sensors for health monitoring, or even personal electronics such as blue tooth transmitters (driving power ~5 mW; data transmission rate ~ 500 kbits/s; power consumption 10 nW/bit) that are only required to be in active mode periodically. The excess energy generated/harvested while the device is in standby is likely sufficient to drive the device when it is in active mode.

In comparison to its thin film counterparts, PZT nanowires have several figures of merit. First, facial growth of high crystallinity PZT nanowires by wet chemical methods exhibits a great advantage for scaling up at a low cost and the possibility of being transferred onto flexible substrates,(*149*) where as single crystal PZT thin films are fabricated at high temperature using chemical vapor deposition.(*164*) Second, the nanowires have extremely high elasticity and are resistant to fatigue, allowing large degrees of mechanical deformation without fracturing.(*165*) This results in largely enhanced energy conversion efficiencies due to non-linear mechanical properties. Third, the force/stress required to induce the mechanical deformation of the nanowires is rather small in comparison to that needed to deform a solid thin film based energy harvester, thus permitting nanowire based nanogenerators to operate in scenarios where only small

triggering forces are available, such as in biological system, tiny vibration and even small pressure fluctuation.(*160*) Finally, the nanogenerators based on nanowires do not require a specific driving frequency to operate, but can be driven by a wide range of irregular/random low frequency mechanical agitations that are abundant in our daily life. In contrast, the thin film based cantilever energy harvesters only work at their high resonant frequencies and harmonics,(*157*) which may not be ideal for application in our living environment of irregular physical motion and time-dependent variant amplitudes.

CHAPTER 6

CONCLUSION

Throughout the last four years, as a research assistant in Dr. Wang's group, I have worked towards making significant contributions in one dimensional arrays of oxides research through a series of experiments. My contributions are extensive, encompassing the following topics.

6.1 Density controlled ZnO nanowire arrays on a general substrate, followed by optimization using a statistical design of experiments.

Preceding this endeavor, ZnO nanowires were usually very dense and their density could not be easily controlled. Using a novel chemical approach, density-controlled vertical ZnO nanowire arrays were synthesized on both rigid and flexible substrates by variation of the precursor concentration.(*58*) The synthesis had no special requirements for the substrates as long as their surfaces were locally flat. This technique was a low-cost, time-efficient, and scalable method.

Controlling the morphology of the as-synthesized nanomaterials is usually challenging, and there lacks a general theoretical guidance in experimental approach. The usual "cook-and-look" methods are time-consuming and inefficient. We have developed a novel way of optimizing the aspect ratio of hydrothermally grown ZnO nanowire arrays by utilizing a systematic statistical design and analysis method.(*57*) By controlling the hydrothermal reaction parameters, we have enhanced the aspect ratio of ZnO nanowires from approximately 10 to nearly 23. The statistical design and analysis methods were very effective in reducing the number of necessary experiments and in identifying the optimal experimental parameters.

6.2 Patterned growth of vertical ZnO nanowire arrays and their applications in LEDs.

In order to grow high quality ZnO nanowire arrays for technological applications, it was imperative to develop an approach that met three essential criteria. First, the growth temperature must be low so that it can be integrated with a general substrate. Second, the spatial distribution of the nanowires should be controlled in size, orientation, dimensionality, uniformity, and possibly in shape as well. Finally, all catalysts must be eliminated for integration with silicon-based technology. We have developed a technique that incorporated all of these requirements. Our method combined EBL and a hydrothermal process to achieve patterned and aligned growth of ZnO nanowires at <100 °C on general inorganic substrates such as Si and GaN, without the usage of a catalyst.(*55*)

ZnO-based LEDs are considered as a potential candidate for the next generation of blue/near-UV light sources, due to a variety of advantages of ZnO. By combining low temperature wet chemical methods and EBL, we have demonstrated the capability of controlling the spatial distribution of blue/near-UV LEDs composed of position-controlled arrays of n-ZnO nanowires on a p-GaN thin film substrate. Under forward bias, each single nanowire is a light emitter.(*21*) This approach has considerable potential for applications in high-resolution displays, optical interconnections, and high density data storage.

6.3 Patterned growth of horizontal ZnO nanowire arrays and transfer onto flexible substrates.

As a counterpart of the vertical ZnO nanowire arrays, horizontal arrays are vital components in various applications including strain and force sensors, two-dimensional photonic crystals, integrated circuit interconnections, and high output power-alternating current nanogenerators. Due to unresolved technical problems, there has been very little

progress in this domain, though. Previous methods have resulted in rather sparse distribution of nanowires with random lateral orientations or poor alignment. By using a variation of our chemical synthesis technique, we have fabricated patterned horizontal ZnO nanowire arrays on single crystal ZnO $\{2\bar{1}\bar{1}0\}$ surfaces, with superior control over their dimensionality, orientation and uniformity incorporating EBL and a low temperature hydrothermal decomposition.(*83*) Furthermore, these horizontal nanowires have been successfully lifted off and transferred onto a flexible polymer substrate,(*84*) which greatly expands their potential applications.

6.4 Integrated high performance direct current and alternating current nanogenerators for self-powered nanosystems.

Energy harvesting from the environment for powering nanosystems is a vital imperative for its independent, wireless, and sustainable operation. In this regard, ZnO-based piezoelectric nanogenerators are a promising approach for harvesting the unexploited masses of low-intensity environmental vibrations. We have developed a new nanogenerator composed of integrated, paired nanobrushes made of metal-coated ZnO nanotip arrays and bare ZnO nanowire arrays.(*35*) Additionally, through the stratified stacking of the devices, a four-layer integrated nanogenerator has been accomplished.

We have brought our advancements a step beyond that by integrating 700 rows of lateral ZnO nanowires, producing a peak voltage of 1.26 V at a low strain of 0.19%, which is sufficient to recharge an AA battery. In one of our separate devices, a vertical integration of three layers of ZnO nanowire arrays produces a peak power density of 2.7 mW/cm^3. We have used the vertically-integrated nanogenerator to power a nanowire pH sensor, thus demonstrating a self-powered system comprised entirely of nanowires.(*36*)

6.5 Epitaxial synthesis single crystalline $PbZr_{0.52}Ti_{0.48}O_3$ nanowire arrays by hydrothermal decomposition and high performance alternating current nanogenerators

We have also pioneered the first chemical epitaxial growth of $PbZr_{0.52}Ti_{0.48}O_3$ nanowire arrays and their application as high output energy converters. The nanogenerators fabricated using a single array of $PbZr_{0.52}Ti_{0.48}O_3$ nanowires produce a peak output voltage of ~ 0.7 V, a current density of 4 $\mu A/cm^2$, and an average power density of 2.8 mW/cm^3. The alternating current output of the nanogenerator has been rectified and the harvested energy has been stored and later utilized to light up a commercial LD. This work has been accepted for publication.(*150*)

REFERENCES

1. S. Iijima, Helical Microtubules of Graphitic Carbon. *Nature* **354**, 56 (Nov 7, 1991).

2. T. W. Odom, J. L. Huang, P. Kim, C. M. Lieber, Atomic structure and electronic properties of single-walled carbon nanotubes. *Nature* **391**, 62 (Jan 1, 1998).

3. A. M. Morales, C. M. Lieber, A laser ablation method for the synthesis of crystalline semiconductor nanowires. *Science* **279**, 208 (Jan 9, 1998).

4. Z. W. Pan, Z. R. Dai, Z. L. Wang, Nanobelts of semiconducting oxides. *Science* **291**, 1947 (Mar 9, 2001).

5. M. H. Huang, Y. Wu, H. Feick, N. Tran, E. Weber, P. Yang, Catalytic Growth of Zinc Oxide Nanowires by Vapor Transport. *Advanced Materials* **13**, 113 (2001).

6. Z. L. Wang, Ten years' venturing in ZnO nanostructures: from discovery to scientific understanding and to technology applications. *Chinese Science Bulletin* **54**, 4021 (Nov, 2009).

7. Z. L. Wang, ZnO nanowire and nanobelt platform for nanotechnology. *Materials Science and Engineering, R* **64**, 33 (Apr 3, 2009).

8. Z. L. Wang, The new field of nanopiezotronics. *Materials Today* **10**, 20 (May, 2007).

9. Z. L. Wang, Theme issue: inorganic nanotubes and nanowires. *Journal of Materials Chemistry* **19**, 826 (2009).

10. [Anon], Map of physics. *Physics World* **21**, 36 (Oct, 2008).

11. U. Ozgur, Y. I. Alivov, C. Liu, A. Teke, M. A. Roshchikov, S. Dogan, V. Avrutin, S. J. Cho, H. Morkoc, A comprehensive review of ZnO materials and devices. *Journal of Applied Physics* **98**, 041301 (2005).

12. D. C. Look, Recent advances in ZnO materials and devices. *Materials Science and Engineering B-Solid* **80**, 383 (Mar 22, 2001).

13. Y. W. Heo, D. P. Norton, L. C. Tien, Y. Kwon, B. S. Kang, F. Ren, S. J. Pearton, J. R. LaRoche, ZnO nanowire growth and devices. *Materials Science and Engineering R* **47**, 1 (Dec 20, 2004).

14. G. C. Yi, C. R. Wang, W. I. Park, ZnO nanorods: synthesis, characterization and applications. *Semiconductor Science and Technology* **20**, S22 (Apr, 2005).

15. Z. L. Wang, Oxide nanobelts and nanowires - Growth, properties and applications. *Journal of Nanoscience and Nanotechnology* **8**, 27 (Jan, 2008).

16. Z. L. Wang, Splendid One-Dimensional Nanostructures of Zinc Oxide: A New Nanomaterial Family for Nanotechnology. *ACS Nano* **2**, 1987 (Oct, 2008).

17. M. H. Huang, S. Mao, H. Feick, H. Yan, Y. Wu, H. Kind, E. Weber, R. Russo, P. Yang, Room-temperature ultraviolet nanowire nanolasers. *Science* **292**, 1897 (Jun 8, 2001).

18. K. Govender, D. S. Boyle, P. O'Brien, D. Binks, D. West, D. Coleman, Room-Temperature Lasing Observed from ZnO Nanocolumns Grown by Aqueous Solution Deposition. *Advanced Materials* **14**, 1221 (2002).

19. W. I. Park, G. C. Yi, Electroluminescence in n-ZnO Nanorod Arrays Vertically Grown on p-GaN. *Advanced Materials* **16**, 87 (2004).

20. X. M. Zhang, M. Y. Lu, Y. Zhang, L. J. Chen, Z. L. Wang, Fabrication of a High-Brightness Blue-Light-Emitting Diode Using a ZnO-Nanowire Array Grown on p-GaN Thin Film. *Advanced Materials* **21**, 2767 (Jul 20, 2009).

21. S. Xu, C. Xu, Y. Liu, Y. Hu, R. Yang, Q. Yang, J. H. Ryou, H. J. Kim, Z. Lochner, S. Choi, R. Dupuis, Z. L. Wang, Ordered Nanowire Array Blue/Near-UV Light Emitting Diodes. *Advanced Materials* **22**, 4749 (2010).

22. D. S. Mao, X. Wang, W. Li, X. H. Liu, Q. Li, J. F. Xu, Electron field emission from hydrogen-free amorphous carbon-coated ZnO tip array. *Journal of Vacuum Science & Technology B* **20**, 278 (Jan-Feb, 2002).

23. Y. W. Zhu, H. Z. Zhang, X. C. Sun, S. Q. Feng, J. Xu, Q. Zhao, B. Xiang, R. M. Wang, D. P. Yu, Efficient field emission from ZnO nanoneedle arrays. *Applied Physics Letters* **83**, 144 (2003).

24. W. Z. Wang, B. Zeng, J. Yang, B. Poudel, J. Huang, M. J. Naughton, Z. Ren, Aligned ultralong ZnO nanobelts and their enhanced field emission. *Advanced Materials* **18**, 3275 (Dec 18, 2006).

25. T. Y. Wei, P. H. Yeh, S. Y. Lu, Z. L. Wang, Gigantic Enhancement in Sensitivity Using Schottky Contacted Nanowire Nanosensor. *Journal of the American Chemical Society* **131**, 17690 (Dec 9, 2009).

26. P. H. Yeh, Z. Li, Z. L. Wang, Schottky-Gated Probe-Free ZnO Nanowire Biosensor. *Advanced Materials* **21**, 4975 (Dec 28, 2009).

27. J. Zhou, Y. D. Gu, Y. F. Hu, W. J. Mai, P. H. Yeh, G. Bao, A. K. Sood, D. L. Polla, Z. L. Wang, Gigantic enhancement in response and reset time of ZnO UV nanosensor by utilizing Schottky contact and surface functionalization. *Applied Physics Letters* **94**, (May 11, 2009).

28. M. Law, L. E. Greene, J. C. Johnson, R. Saykally, P. D. Yang, Nanowire dye-sensitized solar cells. *Nature Materials* **4**, 455 (Jun, 2005).

29. C. Levy-Clement, R. Tena-Zaera, M. A. Ryan, A. Katty, G. Hodes, CdSe-Sensitized p-CuSCN/nanowire n-ZnO heterojunctions. *Advanced Materials* **17**, 1512 (Jun 17, 2005).

30. B. Weintraub, Y. G. Wei, Z. L. Wang, Optical Fiber/Nanowire Hybrid Structures for Efficient Three-Dimensional Dye-Sensitized Solar Cells. *Angewandte Chemie-International Edition* **48**, 8981 (2009).

31. Y. G. Wei, C. Xu, S. Xu, C. Li, W. Wu, Z. L. Wang, Planar Waveguide-Nanowire Integrated Three-Dimensional Dye-Sensitized Solar Cells. *Nano Letters* **10**, 2092 (Jun, 2010).

32. Z. L. Wang, J. H. Song, Piezoelectric nanogenerators based on zinc oxide nanowire arrays. *Science* **312**, 242 (Apr 14, 2006).

33. X. D. Wang, J. H. Song, J. Liu, Z. L. Wang, Direct-current nanogenerator driven by ultrasonic waves. *Science* **316**, 102 (Apr 6, 2007).

34. R. S. Yang, Y. Qin, L. M. Dai, Z. L. Wang, Power generation with laterally packaged piezoelectric fine wires. *Nature Nanotechnology* **4**, 34 (Jan, 2009).

35. S. Xu, Y. G. Wei, J. Liu, R. Yang, Z. L. Wang, Integrated Multilayer Nanogenerator Fabricated Using Paired Nanotip-to-Nanowire Brushes. *Nano Letters* **8**, 4027 (Nov, 2008).

36. S. Xu, Y. Qin, C. Xu, Y. G. Wei, R. S. Yang, Z. L. Wang, Self-powered nanowire devices. *Nature Nanotechnology* **5**, 366 (2010).

37. Z. L. Wang, Nanopiezotronics. *Advanced Materials* **19**, 889 (Mar 19, 2007).

38. Z. L. Wang, Towards Self-Powered Nanosystems: From Nanogenerators to Nanopiezotronics. *Advanced Functional Materials* **18**, 3553 (Nov 24, 2008).

39. R. A. Laudise, A. A. Ballman, Hydrothermal Synthesis of Zinc Oxide and Zinc Sulfide. *Journal of Physical Chemistry* **64**, 688 (1960).

40. M. A. Verges, A. Mifsud, C. J. Serna, Formation of Rod-Like Zinc-Oxide Microcrystals in Homogeneous Solutions. *Journal of the Chemical Society-Faraday Transactions* **86**, 959 (Mar 21, 1990).

41. L. Vayssieres, K. Keis, S. E. Lindquist, A. Hagfeldt, Purpose-Built Anisotropic Metal Oxide Material: 3D Highly Oriented Microrod Array of ZnO. *Journal of Physical Chemistry B* **105**, 3350 (2001).

42. B. D. Yao, Y. F. Chan, N. Wang, Formation of ZnO nanostructures by a simple way of thermal evaporation. *Applied Physics Letters* **81**, 757 (2002).

43. W.I. Park, G. C. Yi, M. Kim, S. J. Pennycook, ZnO Nanoneedles Grown Vertically on Si Substrates by Non-Catalytic Vapor-Phase Epitaxy. *Advanced Materials* **14**, 1841 (2002).

44. W. I. Park, D. H. Kim, S. W. Jung, G. C. Yi, Metalorganic vapor-phase epitaxial growth of vertically well-aligned ZnO nanorods. *Applied Physics Letters* **80**, 4232 (2002).

45. H. Yuan, Y. Zhang, Preparation of well-aligned ZnO whiskers on glass substrate by atmospheric MOCVD. *Journal of Crystal Growth* **263**, 119 (2004).

46. Y. W. Heo, V. Varadarajan, M. Kaufman, K. Kim, D. P. Norton, F. Ren, P. H. Fleming, Site-specific growth of Zno nanorods using catalysis-driven molecular-beam epitaxy. *Applied Physics Letters* **81**, 3046 (2002).

47. Y. Sun, G. M. Fuge, M. N. R. Ashfold, Growth of aligned ZnO nanorod arrays by catalyst-free pulsed laser deposition methods. *Chemical Physics Letters* **396**, 21 (Sep 21, 2004).

48. W. T. Chiou, W. Y. Wu, J. M. Ting, Growth of single crystal ZnO nanowires using sputter deposition. *Diamond and Related Materials* **12**, 1841 (2003).

49. C. K. Xu, G. D. Xu, Y. K. Liu, G. H. Wang, A simple and novel route for the preparation of ZnO nanorods. *Solid State Communications* **122**, 175 (2002).

50. D. Lin, W. Pan, H. Wu, Morphological Control of Centimeter Long Aluminum-Doped Zinc Oxide Nanofibers Prepared by Electrospinning. *Journal of the American Ceramic Society* **90**, 71 (2007).

51. D. Lin, H. Wu, W. Pan, Photoswitches and memories assembled by electrospinning aluminum-doped zinc oxide single nanowires. *Advanced Materials* **19**, 3968 (2007).

52. J. J. Wu, H. I. Wen, C. H. Tseng, S. C. Liu, Well-aligned ZnO nanorods via hydrogen treatment of ZnO films. *Advanced Functional Materials* **14**, 806 (Aug, 2004).

53. H. Zhang, D. Yang, X. Ma, N. Du, J. Wu, D. Que, Straight and Thin ZnO Nanorods: Hectogram-Scale Synthesis at Low Temperature and Cathodoluminescence. *Journal of Physical Chemistry B* **110**, 827 (2006).

54. P. C. Chang, J. G. Lu, ZnO Nanowire Field-Effect Transistors. *IEEE Transactions on Electron Devices* **55**, 2977 (Nov, 2008).

55. S. Xu, Y. Wei, M. Kirkham, J. Liu, W. Mai, D. Davidovic, R. L. Snyder, Z. L. Wang, Patterned Growth of Vertically Aligned ZnO Nanowire Arrays on Inorganic Substrates at Low Temperature without Catalyst. *Journal of the American Chemical Society* **130**, 14958 (Nov 12, 2008).

56. K. Govender, D. S. Boyle, P. B. Kenway, P. O'Brien, Understanding the factors that govern the deposition and morphology of thin films of ZnO from aqueous solution. *Journal of Materials Chemistry* **14**, 2575 (2004).

57. S. Xu, N. Adiga, S. Ba, T. Dasgupta, C. F. J. Wu, Z. L. Wang, Optimizing and Improving the Growth Quality of ZnO Nanowire Arrays Guided by Statistical Design of Experiments. *ACS Nano* **3**, 1803 (Jul, 2009).

58. S. Xu, C. Lao, B. Weintraub, Z. L. Wang, Density-controlled growth of aligned ZnO nanowire arrays by seedless chemical approach on smooth surfaces. *Journal of Materials Research* **23**, 2072 (Aug, 2008).

59. L. Vayssieres, Growth of Arrayed Nanorods and Nanowires of ZnO from Aqueous Solutions. *Advanced Materials* **15**, 464 (2003).

60. J. Zhang, L. D. Sun, C. S. Liao, C. H. Yan, A simple route towards tubular ZnO. *Chemical Communications*, 262 (2002).

61. D. F. Zhang, L. D. Sun, J. L. Yin, C. H. Yan, R. M. Wang, Attachment-driven morphology evolvement of rectangular ZnO nanowires. *Journal of Physical Chemistry B* **109**, 8786 (May 12, 2005).

62. P. X. Gao, J. H. Song, J. Liu, Z. L. Wang, Nanowire piezoelectric nanogenerators on plastic substrates as flexible power sources for nanodevices. *Advanced Materials* **19**, 67 (Jan 8, 2007).

63. X. Gao, X. Li, W. Yu, Flowerlike ZnO Nanostructures via Hexamethylenetetramine-Assisted Thermolysis of Zinc-Ethylenediamine Complex. *Journal of Physical Chemistry B* **109**, 1155 (2005).

64. W. B. Wu, G. D. Hu, S. G. Cui, Y. Zhou, H. T. Wu, Epitaxy of Vertical ZnO Nanorod Arrays on Highly (001)-Oriented ZnO Seed Monolayer by a Hydrothermal Route. *Crystal Growth & Design* **8**, 4014 (Nov, 2008).

65. C. F. J. Wu, S. S. Mao, F. S. S. Ma, SEL: A Search Method Based on Orthogonal Arrays. In Statistical Design and Analysis of Industrial Experiments. *Ghosh, S., Ed.;, Marcel Dekker: New York*, 279 (1990).

66. C. F. J. Wu, M. Hamada, Experiments: Planning, Analysis, and Parameter Design Optimization. *Wiley: New York*, (2000).

67. T. Fujibayashi, T. Matsui, M. Kondo, Improvement in quantum efficiency of thin film Si solar cells due to the suppression of optical reflectance at transparent conducting oxide/Si interface by TiO2/ZnO antireflection coating. *Applied Physics Letters* **88**, 183508 (May 1, 2006).

68. C. C. Striemer, P. M. Fauchet, Dynamic etching of silicon for broadband antireflection applications. *Applied Physics Letters* **81**, 2980 (Oct 14, 2002).

69. L. Hu, G. Chen, Analysis of optical absorption in silicon nanowire Arrays for photovoltaic applications. *Nano Letters* **7**, 3249 (Nov, 2007).

70. Y. J. Lee, D. S. Ruby, D. W. Peters, B. B. McKenzie, J. W. P. Hsu, ZnO nanostructures as efficient antireflection layers in solar cells. *Nano Letters* **8**, 1501 (May, 2008).

71. H. K. Park, M. H. Oh, S. W. Kim, G. H. Kim, D. H. Youn, S. Lee, S. H. Kim, K. C. Kim, S. L. Maeng, Vertically well-aligned ZnO nanowires on c-Al_2O_3 and GaN substrates by Au catalyst. *Etri Journal* **28**, 787 (Dec, 2006).

72. D. F. Liu, Y. J. Xiang, X. C. Wu, Z. X. Zhang, L. F. Liu, L. Song, X. W. Zhao, S. D. Luo, W. J. Ma, J. Shen, W. Y. Zhou, G. Wang, C. Y. Wang, S. S. Xie, Periodic ZnO nanorod arrays defined by polystyrene microsphere self-assembled monolayers. *Nano Letters* **6**, 2375 (Oct 11, 2006).

73. W. I. Park, G. C. Yi, M. Kim, S. J. Pennycook, ZnO Nanoneedles Grown Vertically on Si Substrates by Non-Catalytic Vapor-Phase Epitaxy. *Advanced Materials* **14**, 1841 (2002).

74. C. H. Liu, J. A. Zapien, Y. Yao, X. Meng, C. S. Lee, S. Fan, Y. Lifshitz, S. T. Lee, High-Density, Ordered Ultraviolet Light-Emitting ZnO Nanowire Arrays. *Advanced Materials* **15**, 838 (2003).

75. Y. J. Kim, C. H. Lee, Y. J. Hong, G. C. Yi, S. S. Kim, H. Cheong, Controlled selective growth of ZnO nanorod and microrod arrays on Si substrates by a wet chemical method. *Applied Physics Letters* **89**, 163128 (2006).

76. Y. J. Kim, C. H. Lee, Y. J. Hong, G. C. Yi, S. S. Kim, H. Cheong, Controlled selective growth of ZnO nanorod and microrod arrays on Si substrates by a wet chemical method. *Applied Physics Letters* **89**, 163128 (2006).

77. J. B. Cui, U. Gibson, Low-temperature fabrication of single-crystal ZnO nanopillar photonic bandgap structures. *Nanotechnology*, 15532 (2007).

78. X. D. Wang, J. H. Song, Z. L. Wang, Nanowire and nanobelt arrays of zinc oxide from synthesis to properties and to novel devices. *Journal of Materials Chemistry* **17**, 711 (2007).

79. Y. Q. Liang, C. G. Zhen, D. C. Zou, D. S. Xu, Preparation of free-standing nanowire arrays on conductive substrates. *Journal of the American Chemical Society* **126**, 16338 (Dec 22, 2004).

80. V. Gupta, P. Bhattacharya, Y. I. Yuzuk, K. Sreenivas, R. S. Katiyar, Optical phonon modes in ZnO nanorods on Si prepared by pulsed laser deposition. *Journal of Crystal Growth* **287**, 39 (Jan 18, 2006).

81. H. Q. Le, S. J. Chua, K. P. Loh, E. A. Fitzgerald, Y. W. Koh, Synthesis and optical properties of well aligned ZnO nanorods on GaN by hydrothermal synthesis. *Nanotechnology* **17**, 483 (Jan 28, 2006).

82. Y. Liang, C. Zhen, D. Zou, D. Xu, Preparation of Free-Standing Nanowire Arrays on Conductive Substrates. *Journal of the American Chemical Society* **126**, 16338 (2004).

83. S. Xu, Y. Ding, Y. G. Wei, H. Fang, Y. Shen, A. K. Sood, D. L. Polla, Z. L. Wang, Patterned Growth of Horizontal ZnO Nanowire Arrays. *Journal of the American Chemical Society* **131**, 6670 (May 20, 2009).

84. S. Xu, Y. Shen, Y. Ding, Z. L. Wang, Growth and Transfer of Monolithic Horizontal ZnO Nanowire Superstructures onto Flexible Substrates. *Advanced Functional Materials* **20**, 1493 (May 10, 2010).

85. Y. Qin, R. S. Yang, Z. L. Wang, Growth of Horizonatal ZnO Nanowire Arrays on Any Substrate. *Journal of Physical Chemistry C* **112**, 18734 (Dec 4, 2008).

86. J. F. Conley, L. Stecker, Y. Ono, Directed integration of ZnO nanobridge devices on a Si substrate. *Applied Physics Letters* **87**, (Nov 28, 2005).

87. S. J. Chang, T. J. Hsueh, C. L. Hsu, Y. R. Lin, I. C. Chen, B. R. Huang, A ZnO nanowire vacuum pressure sensor. *Nanotechnology* **19**, (Mar 5, 2008).

88. N. Babak, A. M. Chris, J. S. Stephan, D. V. Mark, Horizontal growth and in situ assembly of oriented zinc oxide nanowires. *Applied Physics Letters* **85**, 3244 (2004).

89. W. Il Park, C. H. Lee, J. H. Chae, D. H. Lee, G. C. Yi, Ultrafine ZnO Nanowire Electronic Device Arrays Fabricated by Selective Metal-Organic Chemical Vapor Deposition. *Small* **5**, 181 (Jan 19, 2009).

90. O. Harnack, C. Pacholski, H. Weller, A. Yasuda, J. M. Wessels, Rectifying Behavior of Electrically Aligned ZnO Nanorods. *Nano Letters* **3**, 1097 (2003).

91. M. Kirkham, X. D. Wang, Z. L. Wang, R. L. Snyder, Solid Au nanoparticles as a catalyst for growing aligned ZnO nanowires: a new understanding of the vapour-liquid-solid process. *Nanotechnology* **18**, 365304 (Sep 12, 2007).

92. D. K. Andeen, J. H.; Lang, F. F.; Goh, G. K. L.; Tripathy, S. , Lateral Epitaxial Overgrowth of ZnO in Water at 90 degree C. *Advanced Functional Materials* **16**, 799 (2006).

93. Q. B. Xu, R. M. Rioux, M. D. Dickey, G. M. Whitesides, Nanoskiving: A New Method To Produce Arrays of Nanostructures. *Accounts of Chemical Research* **41**, 1566 (Dec, 2008).

94. S. Nakamura, The roles of structural imperfections in InGaN-Based blue light-emitting diodes and laser diodes. *Science* **281**, 956 (Aug 14, 1998).

95. A. Tsukazaki, A. Ohtomo, T. Onuma, M. Ohtani, T. Makino, M. Sumiya, K. Ohtani, S. F. Chichibu, S. Fuke, Y. Segawa, H. Ohno, H. Koinuma, M. Kawasaki, Repeated temperature modulation epitaxy for p-type doping and light-emitting diode based on ZnO. *Nature Materials* **4**, 42 (Jan, 2005).

96. Y. I. Alivov, J. E. Van Nostrand, D. C. Look, M. V. Chukichev, B. M. Ataev, Observation of 430 nm electroluminescence from ZnO/GaN heterojunction light-emitting diodes. *Applied Physics Letters* **83**, 2943 (Oct 6, 2003).

97. D. C. Look, B. Claflin, Y. I. Alivov, S. J. Park, The future of ZnO light emitters. *Physica Status Solidi a-Applied Research* **201**, 2203 (Aug, 2004).

98. D. J. Rogers, F. H. Teherani, A. Yasan, K. Minder, P. Kung, M. Razeghi, Electroluminescence at 375 nm from a ZnO/GaN : Mg/c-Al2O3 heterojunction light emitting diode. *Applied Physics Letters* **88**, (Apr 3, 2006).

99. M. C. Jeong, B. Y. Oh, M. H. Ham, J. M. Myoung, Electroluminescence from ZnO nanowires in n-ZnO film/ZnO nanowire array/p-GaN film heterojunction light-emitting diodes. *Applied Physics Letters* **88**, (May 15, 2006).

100. W. I. Park, G. C. Yi, Electroluminescence in n-ZnO Nanorod Arrays Vertically Grown on p-GaN. *Advanced Materials* **16**, 87 (2004).

101. J. J. Cole, X. Wang, R. J. Knuesel, H. O. Jacobs, Integration of ZnO microcrystals with tailored dimensions forming light emitting diodes and UV photovoltaic cells. *Nano Letters* **8**, 1477 (May, 2008).

102. S. D. Lee, Y. S. Kim, M. S. Yi, J. Y. Choi, S. W. Kim, Morphology Control and Electroluminescence of ZnO Nanorod/GaN Heterojunctions Prepared Using Aqueous Solution. *Journal of Physical Chemistry C* **113**, 8954 (May 21, 2009).

103. T. P. Yang, H. C. Zhu, J. M. Bian, J. C. Sun, X. Dong, B. L. Zhang, H. W. Liang, X. P. Li, Y. G. Cui, G. T. Du, Room temperature electroluminescence from the n-ZnO/p-GaN heterojunction device grown by MOCVD. *Materials Research Bulletin* **43**, 3614 (Dec 1, 2008).

104. K. P. Hsueh, S. C. Huang, C. T. Li, Y. M. Hsin, J. K. Sheu, W. C. Lai, C. J. Tun, Temperature-dependent study of n-ZnO/p-GaN diodes. *Applied Physics Letters* **90**, (Mar 26, 2007).

105. E. Lai, W. Kim, P. D. Yang, Vertical Nanowire Array-Based Light Emitting Diodes. *Nano Research*, (2009).

106. M. C. Jeong, B. Y. Oh, M. H. Ham, S. W. Lee, J. M. Myoung, ZnO-Nanowire-Inserted GaN/ZnO heterojunction light-emitting diodes. *Small* **3**, 568 (Apr, 2007).

107. S. J. An, J. H. Chae, G. C. Yi, G. H. Park, Enhanced light output of GaN-based light-emitting diodes with ZnO nanorod arrays. *Applied Physics Letters* **92**, 121108 (Mar 24, 2008).

108. K. S. Kim, S.-M. Kim, H. Jeong, M. S. Jeong, G. Y. Jung, Enhancement of Light Extraction Through the Wave-Guiding Effect of ZnO Sub-microrods in InGaN Blue Light-Emitting Diodes. *Advanced Functional Materials* **20**, 1076 (April 6, 2010).

109. H.-M. Kim, Y. H. Cho, H. Lee, S. I. Kim, S. R. Ryu, D. Y. Kim, T. W. Kang, K. S. Chung, High-Brightness Light Emitting Diodes Using Dislocation-Free Indium Gallium Nitride/Gallium Nitride Multiquantum-Well Nanorod Arrays. *Nano Letters* **4**, 1059 (2004).

110. I. E. Titkov, L. A. Delimova, A. S. Zubrilov, N. V. Seredova, I. A. Liniichuk, I. V. Grekhov, ZnO/GaN heterostructure for LED applications. *Journal of Modern Optics* **56**, 653 (2009).

111. I. E. Titkov, A. S. Zubrilov, L. A. Delimova, D. V. Mashovets, I. A. Liniichuk, I. V. Grekhov, White electroluminescence from ZnO/GaN structures. *Semiconductors* **41**, 564 (May, 2007).

112. S. H. Park, S. W. Han, Charge influence and growth mechanism of ZnO nanorods. *Journal of Nanoscience and Nanotechnology* **7**, 2526 (Jul, 2007).

113. K. A. Bulashevich, I. Y. Evstratov, S. Y. Karpov, Hybrid ZnO/III-nitride light-emitting diodes: modelling analysis of operation. *Physica Status Solidi a-Applications and Materials Science* **204**, 241 (Jan, 2007).

114. A. M. C. Ng, Y. Y. Xi, Y. F. Hsu, A. B. Djurisic, W. K. Chan, S. Gwo, H. L. Tam, K. W. Cheah, P. W. K. Fong, H. F. Lui, C. Surya, GaN/ZnO nanorod light emitting diodes with different emission spectra. *Nanotechnology* **20**, (Nov 4, 2009).

115. H. Y. Xu, Y. C. Liu, Y. X. Liu, C. S. Xu, C. L. Shao, R. Mu, Ultraviolet electroluminescence from p-GaN/i-ZnO/n-ZnO heterojunction light-emitting diodes. *Applied Physics B-Lasers and Optics* **80**, 871 (Jun, 2005).

116. R. Guo, J. Nishimura, M. Matsumoto, M. Higashihata, D. Nakamura, T. Okada, Electroluminescence from ZnO nanowire-based p-GaN/n-ZnO heterojunction light-emitting diodes. *Applied Physics B-Lasers and Optics* **94**, 33 (Jan, 2009).

117. H. F. Liu, G. X. Hu, H. Gong, K. Y. Zang, S. J. Chua, Effects of oxygen on low-temperature growth and band alignment of ZnO/GaN heterostructures. *Journal of Vacuum Science and Technology A* **26**, 1462 (Nov, 2008).

118. Y. I. Alivov, U. Ozgur, S. Dogan, C. Liu, Y. Moon, X. Gu, V. Avrutin, Y. Fu, H. Morkoc, Forward-current electroluminescence from GaN/ZnO double heterostructure diode. *Solid-State Electronics* **49**, 1693 (Oct, 2005).

119. C. Bayram, F. H. Teherani, D. J. Rogers, M. Razeghi, A hybrid green light-emitting diode comprised of n-ZnO/(InGaN/GaN) multi-quantum-wells/p-GaN. *Applied Physics Letters* **93**, 081111 (Aug 25, 2008).

120. H. W. Choi, C. W. Jeon, M. D. Dawson, P. R. Edwards, R. W. Martin, S. Tripathy, Mechanism of enhanced light output efficiency in InGaN-based microlight emitting diodes. *Journal of Applied Physics* **93**, 5978 (2003).

121. I. Schnitzer, E. Yablonovitch, C. Caneau, T. J. Gmitter, A. Scherer, 30-Percent External Quantum Efficiency from Surface Textured, Thin-Film Light-Emitting-Diodes. *Applied Physics Letters* **63**, 2174 (Oct 18, 1993).

122. H. Kim, K. K. Kim, K. K. Choi, H. Kim, J. O. Song, J. Cho, K. H. Baik, C. Sone, Y. Park, Design of high-efficiency GaN-based light emitting diodes with vertical injection geometry. *Applied Physics Letters* **91**, 023510 (2007).

123. E. F. Schubert, J. K. Kim, Solid-state light sources getting smart. *Science* **308**, 1274 (May 27, 2005).

124. W. L. Barnes, Electromagnetic crystals for surface plasmon polaritons and the extraction of light from emissive devices. *Journal of Lightwave Technology* **17**, 2170 (Nov, 1999).

125. T. N. Oder, K. H. Kim, J. Y. Lin, H. X. Jiang, III-nitride blue and ultraviolet photonic crystal light emitting diodes. *Applied Physics Letters* **84**, 466 (2004).

126. J. Zhong, H. Chen, G. Saraf, Y. Lu, C. K. Choi, J. J. Song, D. M. Mackie, H. Shen, Integrated ZnO nanotips on GaN light emitting diodes for enhanced emission efficiency. *Applied Physics Letters* **90**, (May 14, 2007).

127. K. K. Kim, S. D. Lee, H. Kim, J. C. Park, S. N. Lee, Y. Park, S. J. Park, S. W. Kim, Enhanced light extraction efficiency of GaN-based light-emitting diodes with ZnO nanorod arrays grown using aqueous solution. *Applied Physics Letters* **94**, (Feb 16, 2009).

128. H. Sekiguchi, K. Kato, J. Tanaka, A. Kikuchi, K. Kishino, Ultraviolet GaN-based nanocolumn light-emitting diodes grown on n-(111) Si substrates by rf-plasma-assisted molecular beam epitaxy. *Physica Status Solidi a-Applications and Materials Science* **205**, 1067 (May, 2008).

129. S. H. Park, S. H. Kim, S. W. Han, Growth of homoepitaxial ZnO film on ZnO nanorods and light emitting diode applications. *Nanotechnology* **18**, (Feb 7, 2007).

130. Z. L. Wang, Self-powered nanotech - Nanosize machines need still tinier power plants. *Scientific American* **298**, 82 (Jan, 2008).

131. B. Z. Tian, X. L. Zheng, T. J. Kempa, Y. Fang, N. F. Yu, G. H. Yu, J. L. Huang, C. M. Lieber, Coaxial silicon nanowires as solar cells and nanoelectronic power sources. *Nature* **449**, 885 (Oct 18, 2007).

132. C. F. Pan, H. Wu, C. Wang, B. Wang, L. Zhang, Z. D. Cheng, P. Hu, W. Pan, Z. Y. Zhou, X. Yang, J. Zhu, Nanowire-based high performance "micro fuel cell": One nanowire, one fuel cell. *Advanced Materials* **20**, 1644 (May 5, 2008).

133. Y. Qin, X. D. Wang, Z. L. Wang, Microfibre-nanowire hybrid structure for energy scavenging. *Nature* **451**, 809 (Feb 14, 2008).

134. Z. L. Wang, J. H. Song, Piezoelectric nanogenerators based on zinc oxide nanowire arrays. *Science* **312**, 242 (Apr 14, 2006).

135. X. Wang, J. Song, J. Liu, Z. L. Wang, Direct-Current Nanogenerator Driven by Ultrasonic Waves. *Science* **316**, 102 (April 6, 2007, 2007).

136. J. Liu, P. Fei, J. Zhou, R. Tummala, Z. L. Wang, Toward high output-power nanogenerator. *Applied Physics Letters* **92**, 173105 (Apr 28, 2008).

137. Y. Qin, X. D. Wang, Z. L. Wang, Microfibre-nanowire hybrid structure for energy scavenging. *Nature* **451**, 809 (Feb 14, 2008).

138. Y. Gao, Z. L. Wang, Electrostatic potential in a bent piezoelectric nanowire. The fundamental theory of nanogenerator and nanopiezotronics. *Nano Letters* **7**, 2499 (Aug, 2007).

139. Y. Gao, Z. L. Wang, Equilibrium Potential of Free Charge Carriers in a Bent Piezoelectric Semiconductive Nanowire. *Nano Letters* **9**, 1103 (Mar, 2009).

140. J. Liu, P. Fei, J. Zhou, R. Tummala, Z. L. Wang, Toward high output-power nanogenerator. *Applied Physics Letters* **92**, 173105 (Apr 28, 2008).

141. X. D. Wang, J. Liu, J. H. Song, Z. L. Wang, Integrated nanogenerators in biofluid. *Nano Letters* **7**, 2475 (Aug, 2007).

142. J. Liu, P. Fei, J. H. Song, X. D. Wang, C. S. Lao, R. Tummala, Z. L. Wang, Carrier density and Schottky barrier on the performance of DC nanogenerator. *Nano Letters* **8**, 328 (Jan, 2008).

143. B. S. Kang, F. Ren, Y. W. Heo, L. C. Tien, D. P. Norton, S. J. Pearton, pH measurements with single ZnO nanorods integrated with a microchannel. *Applied Physics Letters* **86**, (Mar 14, 2005).

144. X. Chen, S. Y. Xu, N. Yao, W. H. Xu, Y. Shi, Potential measurement from a single lead zirconate titanate nanofiber using a nanomanipulator. *Applied Physics Letters* **95**, 253113 (Aug 10, 2009).

145. R. Guo, L. E. Cross, S. E. Park, B. Noheda, D. E. Cox, G. Shirane, Origin of the high piezoelectric response in $PbZr_{1-x}Ti_xO_3$. *Physical Review Letters* **84**, 5423 (Jun 5, 2000).

146. R. Ramesh, W. K. Chan, B. Wilken, H. Gilchrist, T. Sands, J. M. Tarascon, V. G. Keramidas, D. K. Fork, J. Lee, A. Safari, Fatigue and Retention in Ferroelectric Y-Ba-Cu-O/Pb-Zr-Ti-O/Y-Ba-Cu-O Heterostructures. *Applied Physics Letters* **61**, 1537 (Sep 28, 1992).

147. X. Chen, S. Xu, N. Yao, Y. Shi, 1.6 V Nanogenerator for Mechanical Energy Harvesting Using PZT Nanofibers. *Nano Letters*, (2010).

148. A. I. Kingon, S. Srinivasan, Lead zirconate titanate thin films directly on copper electrodes for ferroelectric, dielectric and piezoelectric applications. *Nature Materials* **4**, 233 (Mar, 2005).

149. Y. Qi, N. T. Jafferis, K. Lyons, Jr., C. M. Lee, H. Ahmad, M. C. McAlpine, Piezoelectric Ribbons Printed onto Rubber for Flexible Energy Conversion. *Nano Letters* **10**, 524 (Feb, 2010).

150. S. Xu, B. J. Hansen, Z. L. Wang, Piezoelectric-nanowire-enabled power source for driving wireless microelectronics. *Nature Communications*, DOI: 10.1038/ncomms1098 (2010).

151. Y. R. Lin, Y. T. Liu, H. A. Sodano, Hydrothermal synthesis of vertically aligned lead zirconate titanate nanowire arrays. *Applied Physics Letters* **95**, 122901 (Sep 21, 2009).

152. G. Xu, Z. H. Ren, P. Y. Du, W. J. Weng, G. Shen, G. R. Han, Polymer-assisted hydrothermal synthesis of single-crystalline tetragonal perovskite $PbZr_{0.52}Ti_{0.48}O_3$ nanowires. *Advanced Materials* **17**, 907 (Apr 4, 2005).

153. K. S. Hwang, B. H. Kim, X-ray diffraction studies of epitaxial $Pb(Zr,Ti)O_3$ films prepared by chemical solution method. *Materials Chemistry and Physics* **57**, 224 (Jan 25, 1999).

154. M. Alexe, C. Harnagea, D. Hesse, Non-Conventional Micro- and Nanopatterning Techniques for Electroceramics. *Journal of Electroceramics* **12**, 69 (2004).

155. D. M. Kim, C. B. Eom, V. Nagarajan, J. Ouyang, R. Ramesh, V. Vaithyanathan, D. G. Schlom, Thickness dependence of structural and piezoelectric properties of epitaxial $Pb(Zr_{0.52}Ti_{0.48})O_3$ films on Si and $SrTiO_3$ substrates. *Applied Physics Letters* **88**, 142904 (Apr 3, 2006).

156. B. P. Zhu, Q. F. Zhou, J. Shi, K. K. Shung, S. Irisawa, S. Takeuchi, Self-separated hydrothermal lead zirconate titanate thick films for high frequency transducer applications. *Applied Physics Letters* **94**, 102901 (Mar 9, 2009).

157. Y. B. Jeon, R. Sood, J. H. Jeong, S. G. Kim, MEMS power generator with transverse mode thin film PZT. *Sensor and Actuators a-Physical* **122**, 16 (Jul 29, 2005).

158. D. Choi, M. Y. Choi, W. M. Choi, J. J. Shin, J. K. Park, J. S. Seo, J. B. Park, S. M. Yoon, S. J. Chae, Y. H. Lee, S. W. Kim, J. Y. Choi, S. Y. Lee, J. M. Kim, Fully Rollable Transparent Nanogenerators Based on Graphene Electrodes. *Advanced Materials* **22**, 2187 (2010).

159. M. Y. Choi, D. Choi, M. J. Jin, I. Kim, S. H. Kim, J. Y. Choi, S. Y. Lee, J. M. Kim, S. W. Kim, Mechanically Powered Transparent Flexible Charge-Generating Nanodevices with Piezoelectric ZnO Nanorods. *Advanced Materials* **21**, 2185 (Jun 5, 2009).

160. R. Yang, Y. Qin, C. Li, G. Zhu, Z. L. Wang, Converting Biomechanical Energy into Electricity by a Muscle-Movement-Driven Nanogenerator. *Nano Letters* **9**, 1201 (Mar, 2009).

161. C. T. Huang, J. H. Song, W. F. Lee, Y. Ding, Z. Y. Gao, Y. Hao, L. J. Chen, Z. L. Wang, GaN Nanowire Arrays for High-Output Nanogenerators. *Journal of the American Chemical Society* **132**, 4766 (Apr 7, 2010).

162. C. Chang, V. H. Tran, J. Wang, Y.-K. Fuh, L. Lin, Direct-Write Piezoelectric Polymeric Nanogenerator with High Energy Conversion Efficiency. *Nano Letters* **10**, 726 (2010).

163. R. F. Service, Nanogenerators Tap Waste Energy To Power Ultrasmall Electronics. *Science* **328**, 304 (Apr 16, 2010).

164. C. M. Foster, G. R. Bai, R. Csencsits, J. Vetrone, R. Jammy, L. A. Wills, E. Carr, J. Amano, Single-crystal $Pb(Zr_xTi_{1-x})O_3$ thin films prepared by metal-organic chemical vapor deposition: Systematic compositional variation of electronic and optical properties. *Journal of Applied Physics* **81**, 2349 (Mar 1, 1997).

165. Z. Y. Gao, Y. Ding, S. S. Lin, Y. Hao, Z. L. Wang, Dynamic fatigue studies of ZnO nanowires by in-situ transmission electron microscopy. *Physica Status Solidi-Rapid Research Letters* **3**, 260 (Oct, 2009).